



Universitat Autònoma de Barcelona

ADVERTIMENT. L'accés als continguts d'aquesta tesi queda condicionat a l'acceptació de les condicions d'ús establertes per la següent llicència Creative Commons:  http://cat.creativecommons.org/?page_id=184

ADVERTENCIA. El acceso a los contenidos de esta tesis queda condicionado a la aceptación de las condiciones de uso establecidas por la siguiente licencia Creative Commons:  <http://es.creativecommons.org/blog/licencias/>

WARNING. The access to the contents of this doctoral thesis it is limited to the acceptance of the use conditions set by the following Creative Commons license:  <https://creativecommons.org/licenses/?lang=en>



Thermoelectric properties of oxides and related materials

Sweta Bhansali

M.Tech in Nanotechnology

Doctoral Thesis

Doctorate Programme in Physics (Materials Sciences)

Thesis Director: Prof. Dr. Clivia M. Sotomayor Torres

Supervisor: Prof. Dr. Jordi Mompert

Department of Physics
Faculty of Sciences

2016

In memory of my grandfather

Acknowledgements

The author would like to express her gratitude to the Catalan government for a research fellowship through the Agaur FI grant 2013. Additionally, the author would also like to acknowledge the financial support from the Spanish MINECO project nanoTHERM (grant nr. CSD2010-0044).

First of all, I would like to express my deepest gratitude to my thesis director Prof. Dr Clivia M. Sotomayor Torres and all my colleagues in the Phononic and Photonic Nanostructures group, P2N, at the Catalan Institute of Nanoscience and nanotechnology, ICN2, for their great contribution and support to the development of this work. Also, I would like to specially thank Dr Emigdio Chavez from the University of Mainz, Germany, for giving his time regarding the discussions required on nanoscale thermal transport and the overall development of this work.

I would like to thank specially Dr. Jose Santiso from the Catalan Institute of Nanoscience and nanotechnology, ICN2 for his help regarding the pulsed laser deposition technique and also the understanding of the crystallographic properties of perovskites and his help during the last preparation of my thesis.

I would like to thank all my friends and colleagues (present and previous) from ICN2 especially to Dr Worawut Khunsin, Dr. Emigdio Chavez, Dr Marianna Sledzinska, Dr. Daniel Navarro, MsC Ariadna Frenandez, Dr Jordi Gomis-Bresco, Dr Bartlomiej Graczykowski, Dr Juan Sebastian Reparaz, Dr. Marius Costache, Dr. Juan Francisco Sierra García and Dr Nikolaos Kehagias, for their great contribution to my scientific and social life. Especial acknowledge to Noèlia Arias, Erwan Guillotel and Cristina Morales for their indispensable work for the overall scientific development of group.

I am very grateful to Clivia for providing me this great opportunity to work in Europe and who has been there all the while until the completion of my thesis. Without her and her faith in me, nothing of the developed work in this thesis would have been possible.

Last but not the least; I would like to express my infinite gratitude to my lovely family and friends in India as well as Barcelona who have been my support system throughout this journey. I missed my family all the time due to the distance but their continuous love and support gave me the motivation and strength to sail through. My utmost thanks to my grandmother, my father Narpat Singh Bhansali and mother Manju Bhansali who gave their time and everything to me to reach where I am and who showed faith and gave me the wings to fly to achieve my dreams, to my elder brother Harsh Bhansali and sister in law Jyoti Bhansali for their continuous motivation to keep going and to the little stars of my life my niece Dheiva and nephew Shaurya who filled my life with laughter and positivity whenever it seemed dark.

Table of Contents

Abstract

Chapter 1 16

1.1 Nanotechnology and Nanomaterials 16

1.2 Thermoelectricity 17

1.3 Thermoelectric properties and energy conversion 19

1.4 Classification of thermoelectric materials 20

1.4.1 State of the art TE materials: from bulk to nano 21

1.5 Different generations of thermoelectric materials 23

1.5.1 Challenges in Thermoelectric Research 24

1.6 Oxides as thermoelectric material 25

1.7 SrTiO₃ as a promising thermoelectric material 28

Chapter 2

Thermoelectricity in nanostructures 32

2.1 Background 32

2.2 Nanoscale thermal conductivity 36

Considerations to optimize material parameters 37

Chapter 3

Experimental Techniques

3.1 Pulsed Laser Deposition: Sample Preparation Fabrication Technique 40

3.2 STO sample growth 42

3.3 Structural characterization techniques 45

3.3.1 XRD (X-Ray Diffraction) 45

3.3.2 Electron Microscopy 48

3.3.3 Energy-dispersive X-ray spectroscopy (EDS) 50

3.3.4 X-Ray Photoelectron Spectroscopy 51

3.3.5 Atomic Force Microscopy 53

3.4 Electrical Characterization	54
3.4.1 <i>Van Der Pauw technique</i>	54
3.4.2 <i>Seebeck measurement</i>	55
3.5 Thermal conductivity	56
3.6 Graphene transfer on oxide substrates	60
Chapter 4	
Thermoelectric properties of Nb-doped SrTiO₃ thin films	
4.1 Nb-doping of SrTiO ₃ thin films	63
4.1.1 <i>Target Preparation</i>	63
4.1.2 <i>Structural Properties</i>	64
4.1.3 <i>Thermopower measurements</i>	66
4.2 Thickness studies of Nb-doped SrTiO ₃ thin films	67
4.2.1 <i>Thickness measurements</i>	68
4.2.2 <i>XRD and HRTEM analysis</i>	69
4.2.3 <i>XPS analysis</i>	69
4.2.4 <i>Electrical measurements</i>	70
4.3 Results and discussion	74
4.4 Thermoelectric properties as a function of different substrates	77
4.4.1 <i>Introduction</i>	77
4.4.2 <i>Growth and thermoelectric studies</i>	77
4.5 Nb-doped STO multilayers	82
4.6 A novel concept: Graphene as interface dopant	84
Chapter 5	
Conclusions and suggestions for future work	90
APPENDICES	
Appendix I: Historical overview of thermoelectric parameters	95
Bibliography	106

List of Figures

Figure 1.1 Nanomaterials classification	17
Figure 1.2 Schematic of a thermoelectric module	18
Figure 1.3 Illustration of the thermodynamic effects for the relative Seebeck coefficient and Peltier and Thompson effects.	19
Figure 1.4 Thermoelectric figure-of-merit ZT as a function of temperature and year illustrating important milestones with introduction of nanostructuring	22
Figure 1.5 Schematic illustration of the current state of the art ZT achievements in bulk TEs	24
Figure 1.6 Thermoelectric behaviour of different classes of materials	25
Figure 1.7 Figure of merit, ZT, of selected oxides	27
Figure 1.8 The highest ZT oxides over the years	27
Figure 2.1 Development of thermoelectric materials in time	33
Figure 2.2 Impact of alloying on the components of ZT as a function of alloy composition for an generic thermoelectric alloy	34
Figure 3.1 Pulsed Laser Deposition with RHEED	41
Figure 3.2 Illustration of X-ray diffraction from lattice planes in an ordered material. The diagram illustrates the relation between incident angle and lattice plane separation known as Bragg's law.	45
Figure 3.3 Reciprocal space maps of heteroepitaxial layers.	47
Figure 3.4 Reflectometry map using XRR for a 66 nm film	47
Figure 3.5 The interaction of electron beam with the sample in TEM.	49
Figure 3.6 (a) FEI TITAN low base instrument (b) example of the TEM image of the reference sample i.e. LaAlO ₃ substrate	50
Figure 3.7 Example of a EDX spectrum	51
Figure 3.8 Schematic diagram of XPS process showing photoionization of an atom by the ejection of a 1s electron	52
Figure 3.9 the basic working principle of AFM	53
Figure 3.10 Schematic for hall measurement	54
Figures 3.11 Schematics of the Seebeck measurement set up	55
Figure 3.12 Optical image of contacts for measuring thermal conductivity with the 3 ω method	58

Figure 3.13 Schematic of the wet transfer of graphene on a substrate by etching away the copper	61
Figure 4.1 XRD crystallographic planes of (a) targets with different doping concentration and (b) the resulting doped PLD Nb:STO films (c) (200) diffraction peak with different dopant concentration (d) (002) peak of the Nb doped STO film with different doping concentration on LAO substrate	65
Figure 4.2. Electron microscopy images. (a) SEM image of a film on LaAlO ₃ substrate and (b) HR TEM of the epitaxial growth of Nb doped SrTiO ₃ thin film on the LaAlO ₃ substrate.	66
Figure 4.3. Seebeck coefficient of 2 mol% Nb-doped STO on LAO. (a) Temperature dependence on doping concentration for thin films of 50 nm thickness at 105° C.	67
Figure 4.4 (a) schematic of atomic arrangement of STO grown on LaAlO ₃ (Sr, Ti, Al, La, O) (b) X-Ray diffraction pattern of a Nb-SrTiO ₃ film deposited on LAO showing the film reflections marked by red arrow. The most intense peaks correspond to substrate reflections	68
Figure 4.5 (a) In-plane (a) and out-of-plane (c) lattice parameters calculated from reciprocal space maps. (b,c and d) HRTEM cross-section image of the interface region showing the substrate and the epitaxial growth of the 30, 66 and 200 nm thick thin film of Nb-doped SrTiO ₃ on LaAlO ₃ substrate and inset is the BF-STEM image showing the variation of the grain boundaries in the 30, 66 and 200 nm thick films.	70
Figure 4.6. XPS spectra of the different elements in typical film of Nb:STO	71
Figure 4.7 Thermoelectric properties of Nb: SrTiO ₃ films. (a) Charge carrier concentration and Seebeck coefficient at room temperature as a function of thickness. (b) Seebeck coefficient as a function of charge carrier concentration compared to the Pisarenko plot. The solid curve is based on the single parabolic band model described by eq. 4.1 with $m^* = 4.5 m^0$ at 300 K. (c) Seebeck coefficient as a function of temperature (d) power factor as a function of temperature using the values from table 4.1.	72
Figure 4.8 Illustrates the ideal density of states for a high and low value of S depending on the slope at the fermi level	73
Figure 4.9 (a) Thermal conductivity of Nb:STO using the 1-dimensional model as a function of thickness on various substrates. (b) Thermoelectric figure of merit as a function of thickness for Nb:STO on LAO at room temperature.	76
Figure 4.10 Nb:STO on LSAT. (a) XRD scans. (b) HRTEM image showing the outstanding crystalline quality of 2 mol% Nb-doped STO grown on LSAT. (c) Reciprocal space map of the thin film of Nb:STO on LSAT showing excellent lattice matching of the epitaxial film and the substrate	78
Figure 4.11 Seebeck coefficient of Nb:STO on several substrates. (a) on LSAT, (b) on SrLaAlO ₄ , (c) on DyScO ₃ and (d) full set of data for one thickness of Nb:SrTiO ₃ thin film	79

Figure 4.12 AFM images of Nb:STO on (a) a LAO substrate and (b) a LSAT substrate showing roughness <1 nm and a smooth interface (c) Reciprocal space map of the thin film of Nb:STO on LAO showing the lattice mismatch of the epitaxial film and the substrate.	80
Figure 4.13 (a) 2D arrangement of atoms of the doped and undoped layers of STO on LSAT substrate (b) the XRD planes of the layers on LSAT substrate (c) the Seebeck coefficient as a function of temperature of doped and undoped STO layers on LAO and LSAT substrate	83
Figure 4.14 Crystal planes of Nb doped SrTiO ₃ film with and without graphene in 001 direction.	85
Figure 4.15 Raman spectroscopy of Nb:SrTiO ₃ /graphene showing the G and 2D peaks clearly	85
Figure 4.16 HRTEM data showing the superlattice structure of Gr/STO with the inset showing one of the interface and the diffraction pattern of Nb doped SrTiO film and LAO substrate supported by graphene	86
Figure 4.17 Figure 4.17 STEM-EDX mapping distribution of elements contributing to the LAO/GR/STO thermoelectric system using HRTEM	87

List of Tables

Table 3.1 List of some materials deposited for the first time by PLD after 1987	40
Table 3.2 List of samples deposited using PLD in my thesis	43
Table 4.1 Thermoelectric properties of 2% Nb-doped STO films on LAO as a function of thickness at room temperature.	73
Table 4.2 Transport properties of Nb-doped STO films on different substrates	79
Table 4.3 The lattice mismatch between STO and the different substrates	80

List of Symbols

TE	Thermoelectric
S	Seebeck Coefficient
ZT	Thermoelectric Figure of Merit
TMO	Transition Metal Oxide
PLD	Pulsed Laser Deposition
\dot{Q}	Peltier coefficient
V	Total Volume
STO	Strontium Titanate
LAO	Lanthium aluminate
LSAT	Lanthanum aluminate - strontium aluminium tantalite.
SLAO	Strontium Lanthanum Aluminate
DyScO ₃	Scandium Dysprosium
SiO ₂	Silicon dioxide
T	Temperature
ϵ	Electron energy
η	Efficiency
λ	De Broglie wavelength
μ	chemical potential
u_s	Velocity of sound
\hbar	Reduced planck's constant
φ	Electric potential
Σ	Electrical conductivity
τ	Phonon relaxation time
τ_{qs}	Total relaxation time of each mode
μT	Thomson coefficient
κ	Thermal conductivity
e	Charge of an electron
m_e	Mass of an electron
k_B	Boltzmann constant
h	Planck's constant
E _g	Bandgap energy
n_e	Electron concentration
J	Electric current density
u	Carrier mobility
v	Electron velocity
f_0	Fermi–Dirac distribution
E _c	Conduction band edge
E _f	Fermi energy
le	Electron mean free path
L _p , Λ	Phonon mean free path
r	Scattering parameter
I	Electric current
T _m	Melting point

γ	Grüneisen constant
ϵ	Fractional amplitude of interatomic thermal vibration
R	Ideal gas constant
N_0	Avogadro's number
ρ	Density
C_v	Specific heat at constant volume
v_g	Phonon group velocity
ω_{qs}	Phonon frequency
n_{qs}	Bose-Einstein equilibrium phonon distribution function
v_{qs}	Group velocity
$h\nu$	Photon energy
E_K	Kinetic Energy of the electron
W	Work function in XPS, quantum well width in superlattice
uc	Unit cell
R_B	Interface thermal resistance
m^*	Effective mass of an electron
χ_{2D}^*	Reduced chemical potential in 2D structures
F_i	Fermi Dirac integral of order 1
T_p	Phonon temperature

Abstract

Nb doped Strontium titanate (SrTiO_3) thin films and multilayers are an increasingly interesting type of material for thermoelectricity due to their tunable structural, thermal and electrical properties. In addition to their stability at higher temperatures other advantages of STO over traditional thermoelectric materials include its non-toxicity and abundance. In this work we show that STO is highly versatile in terms of growth on several substrates and its suitability to be grown in multilayers. We report a comprehensive study of the influence of Nb doping concentration, substrate type (LaAlO_3 , LSAT, NGO, SrLaAlO_4 , DyScO_3 and SiO_2) and film thickness on the structural and thermoelectric properties of SrTiO_3 thin films grown by pulsed laser deposition. In this study Nb doping concentrations (2, 5, and 15 mol%) were investigated and found that the 2 mol % concentration yielded the largest thermopower. Van der Pauw, Seebeck and 3-omega measurements were carried out. The thermal conductivity of thin films with thickness from 30-200 nm measured by 3 ω method, yielded an 8-fold and a 3-fold reduction on LAO and LSAT substrates, compared to the bulk values of 12 and 5.1W/mK, respectively. We relate the origin of this reduction to structural defects revealed by high-resolution transmission electron microscopy. We found that optimised thermoelectric properties were obtained in 50 nm thick STO films with low Nb doping concentration grown on LSAT. LSAT proved to be an excellent substrate due to lattice matching. The derived thermoelectric figure of merit with the measured values, yields a $ZT = 0.35$ for 2 mol % doped Nb: SrTiO_3 thin film on LaAlO_3 substrate and a ZT value of 0.8 on LSAT substrate both at room temperature. Multilayers of doped and undoped STO, in the form of five-period superlattices were grown and found to exhibit a high Seebeck coefficient of $-650\mu\text{V/K}$. We discuss these results considering the nature of the interfacial bonding arrangements, the electron density of states at the Fermi energy and formulating the hypothesis of the formation of a 2-dimensional electron gas. Finally, in order to enhance the thermoelectric performance of the Nb-doped SrTiO_3 thin films multilayers by improving its electrical properties, a single- and a bi-layer graphene were transferred onto the substrate becoming sandwiched between the Nb:STO film and the substrate. This novel STO-graphene structure exhibits very encouraging thermal and transport properties and the preliminary results are part of this thesis.

Chapter 1

Introduction

This chapter provides the context to the research work reported in this thesis such as general aspects of nanotechnology, and why nanostructuring is important for improving the thermoelectric properties of the old and new materials. It also introduces oxide materials and the reasons why they are being considered as important and promising candidates for high temperature thermoelectric applications.

1.1 Nanotechnology and nanomaterials

Nanotechnology is a branch of science and engineering which utilizes the nanometer scale (10^{-9} meters) in manufacturing of structures and devices relying on new phenomena brought about by the dimensional control in that length scale. Scientists have been developing the ability to manipulate a single atom and or small group of atoms for startling applications with significantly modified characteristics including mechanical, optical, electrical, magnetic, and thermal properties. Unique material properties can be obtained in order to develop new capabilities and as a consequence, applications have been successfully demonstrated. In particular, energy materials have attracted great attention due to improved efficiency [1]. Solar power conversion efficiency has been increased from 4 to 14 % by using nanoengineered surfaces supported by new material synthesis routes which have led to a better understanding of their enhanced energy-related properties [2]. Figure 1.1 depicts different nanomaterials architectures, classified according to the number of degrees of freedom of charge carriers [3]. By way of illustration, charge carriers in a nanoparticle or in a quantum structure are confined in three dimensions which corresponds to “zero-dimensions” or 0D; nanowires and thin film structures are confined in two and one dimensions and are referred to as 1D and 2D structures, respectively [4]. Large size crystals, such as bulk nanostructures, with nanoscale building blocks, are known as 3D-bulk structures [5]. Among these classified nanomaterials, bulk nanomaterials (NM) can now be fabricated in high volumes [6, 7].

In this thesis thin films and multilayers are investigated for thermoelectric applications.

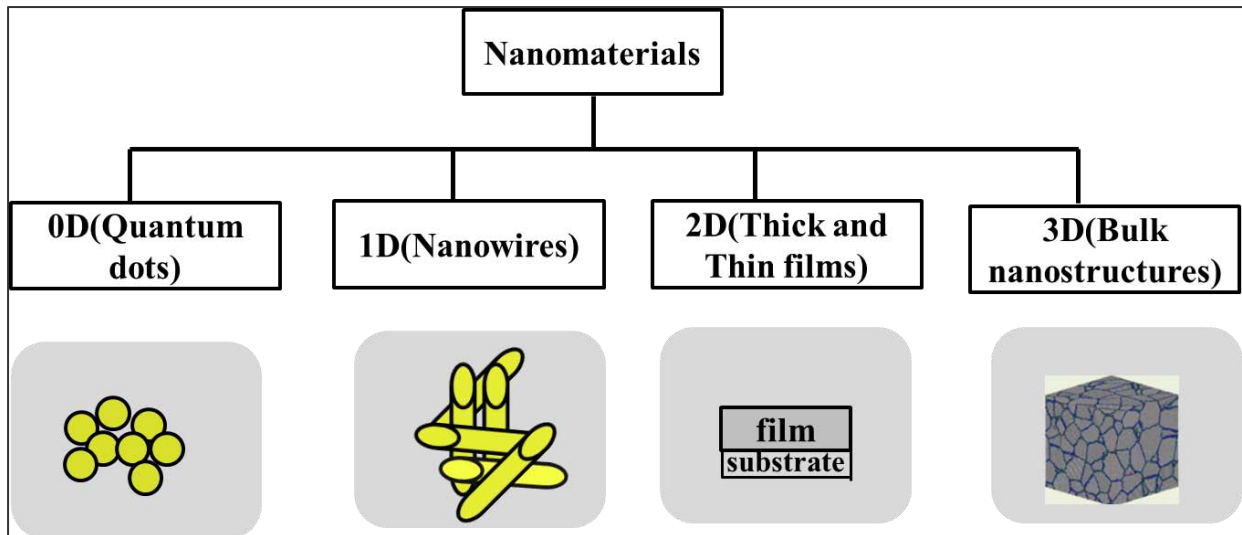


Figure1.1 Nanomaterials classification [3]

1.2 Thermoelectricity

The emerging global need for energy production, conservation and management has intensified interest in more efficient means of power generation. Increasing the existing energy supply must come from a variety of renewable sources including solar, wind, biomass and others. Among the most promising source of power generation is electricity generated by the temperature difference in a material via thermoelectricity. The thermoelectric materials convert thermal energy into electrical energy by a process known as thermoelectric (TE) conversion. The heat source giving rise to the temperature difference can be combustion engines using fossil fuels, sunlight, or a by-product of various processes such as combustion, chemical reactions and nuclear decay. Therefore, thermoelectric materials can play a role in both primary power generation and energy conservation, i.e., waste-heat harvesting [8].

The promise of electrical energy generation from a solid state device for nothing more than a thermal gradient is a highly desirable goal. However, not all thermoelectric materials and devices are made equal. Metals, intrinsic semiconductors and doped oxides can all display the thermoelectric effect, which is defined as a voltage produced in response to a temperature gradient or vice versa. These qualities, as well as the rate at which the thermoelectric conversion occurs, are described by the Seebeck effect, Peltier effect and Thompson effect, respectively[9].

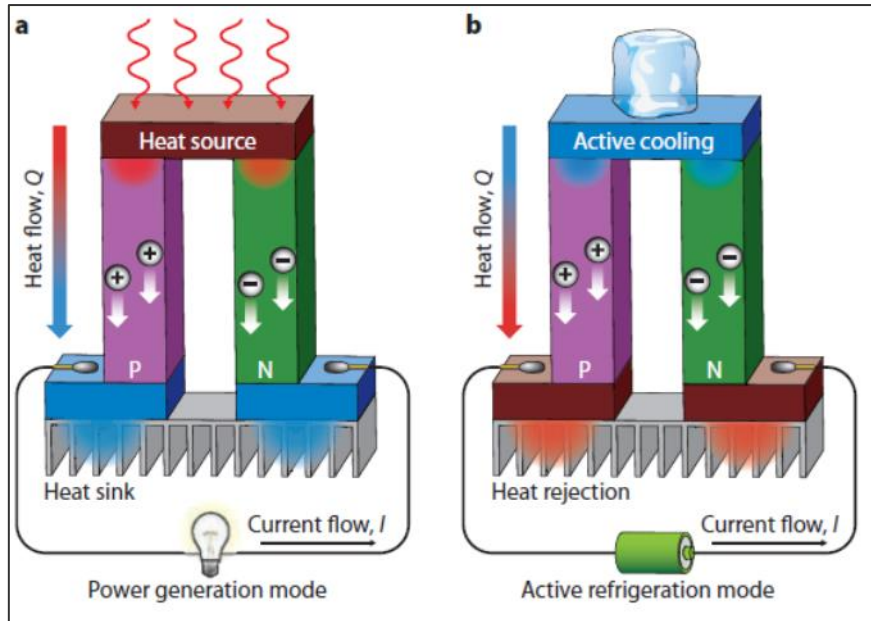


Figure 1.2 Schematic of a thermoelectric module [10].

The TE effect can be used for both power generation and electronic refrigeration. When a temperature gradient (ΔT) is applied to a TE couple consisting of n-type (electron-transporting) and p-type (hole-transporting) elements, the mobile charge carriers at the hot end tend to diffuse to the cold end, producing an electrostatic potential (ΔV). This is known as the Seebeck effect, where $S = \Delta V / \Delta T$ is defined as the Seebeck coefficient, and is the basis of TE power generation, as shown in Figure 1.2. On the other hand, Peltier effect is observed when the carriers attempt to return to the equilibrium when a voltage is applied to a TE couple, by absorbing energy at one contact and releasing it at the other that existed before the current was applied, also shown in Figure 1.2.

A third thermoelectric effect relating the Seebeck coefficient to the Peltier effects by thermodynamics is known as the Thomson effect as mentioned in Figure 1.3. In the Thomson effect, heat is absorbed or produced when current flows in a material with a temperature gradient. The heat is proportional to both the electric current and the temperature gradient.

A worldwide interest has arisen to exploit these effects in many application fields including the waste heat recovery and utilization of the solar heat, temperature controlled seats, portable picnic coolers and management of temperature in microprocessors [10].

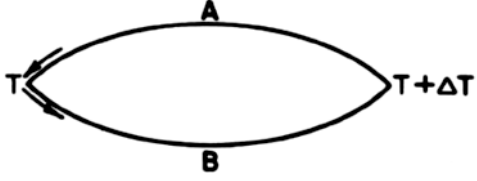
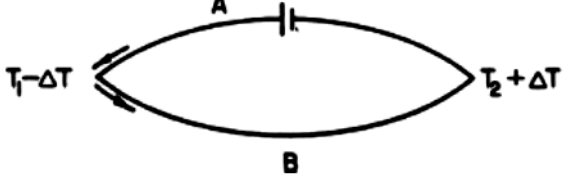
Thermoelectric effects	Schematic representation
Seebeck effect	
Peltier effect	
Thompson effect	<p data-bbox="810 689 1401 775">Connection between the Seebeck and the Peltier effects</p> $\dot{Q} = S\Delta T$

Figure 1.3 Illustration of the thermodynamic effects for the relative Seebeck coefficient and Peltier and Thompson effects.

1.3 Thermoelectric properties and energy conversion

The efficiency of the thermoelectric engine can be derived using the laws of thermodynamics just like in any other heat engine which uses few of the material parameters and source and the sink temperature. The expression for the energy conversion efficiency can be obtained for a case of a thermocouple, with thermo-elements made from a p-type and a n-type semiconductor which are schematically shown in Figure 1.2. The details of derivation of the expression for efficiency of such a generator are readily available elsewhere [9], and the discussion here will home in the final expression for the efficiency and its implications. The maximum efficiency (η_{\max}) of such a generator is given by:

$$\eta_{\max} = \eta_c \gamma \tag{1.1}$$

where η_c is the Carnot efficiency which depends on the temperature difference of the hot and cold ends:

$$\eta_c = \frac{T_H - T_C}{T_H} \tag{1.2}$$

$$\gamma = \frac{\sqrt{1 + Z\bar{T}} - 1}{\sqrt{1 + Z\bar{T}} + \frac{T_C}{T_H}} \tag{1.3}$$

$$\bar{T} = \frac{T_H + T_C}{2} \quad (1.4)$$

and

$$Z = \frac{S^2 \sigma}{\kappa} \quad (1.5)$$

Thus, the maximum efficiency is limited by the Carnot efficiency and a material dependent quantity γ . It is clear that this quantity is directly proportional to the term Z , which is related to three thermoelectric parameters, namely, thermopower (S), electrical conductivity (σ) and thermal conductivity (κ). When Z tends to infinity, the maximum efficiency approaches the Carnot efficiency. ZT is called the thermoelectric figure of merit and hence, the larger the ZT value, the higher the efficiency of a thermoelectric engine.

1.4 Classification of thermoelectric materials

Progress in TE materials requires tailoring the interconnected physical parameters S (Seebeck coefficient), σ (electrical conductivity) and κ (thermal conductivity). New scattering mechanisms to enhance ZT are introduced to decouple the thermal and electrical transport using by nanostructuring. Single crystals usually present the best electrical conductivity due to the absence of grain boundaries that scatter charge carriers, but the ZT of such materials can be optimized only by adjusting the carrier concentration by elemental doping. Tuning of the TE parameters can be achieved by reducing the dimensions as the density of states increases significantly at the discretised energy levels associated to spatial quantum confinement when the size approaches a scale comparable to the electron mean free path in any direction [11]. This has been proven to lead to an enhancement of the Seebeck coefficient and a reduction in thermal conductivity [12]. While these consequences happen due to an intrinsic material characteristic, such as its lateral dimensions, the reduction of thermal conductivity is also possible due to surface scattering of propagating phonons.

The ratio of the thermal conductivity to electrical conductivity is a constant and is known as Wiedemann-Franz-Lorenz law. In intrinsic materials it is not possible to reduce one while increasing the other. Although metals have Seebeck coefficients with values around $10 \mu\text{VK}^{-1}$, which can generate efficiencies of about 1%, they are uneconomical as a source of electrical power.

When n- and p-type semiconductor thermo-elements are connected electrically in series with metal connecting strips and are sandwiched between two electrically insulating but thermally

conducting ceramic plates to form a TE module, a "modern" thermoelectric convertor is created(see Figure 1.2). It will function as a generator when electrical power will be produced to an external load maintaining the temperature difference across the module. In the reversed sense, it will function as a refrigerator since the heat will be absorbed at one end and will be rejected at the other end of the module as an electric current passes through a TE module. From equations 1.1 to 1.5 we obtain the dependence of the figure of merit of a thermoelectric generator, it not only depends on the device operating temperature difference ΔT , or on its average temperature of operation, T , but also on the performance of the thermoelectric material for converting heat into electricity. Consequently, considerable effort has been made to obtain a large Z over a range of temperature for both generation and refrigeration.

Depending on the operating range of temperature the established thermoelectric materials conveniently fall into three categories. Bismuth telluride and its alloys are most extensively employed in refrigeration as it has the highest figures-of-merit and have a maximum operating temperature of around 450 K. After Bismuth telluride comes the next highest figures of merit, alloys based on lead telluride with silicon germanium alloys having the lowest figure of merit. Lead telluride and silicon germanium are used in generator applications with upper operating temperatures of around 1000 and 1300 K, respectively, as can be seen in Figure 1.4.

The discovery of Bi_2Te_3 -based alloys in the 1960s resulted in a roadmap for high-performance TE materials. The motivation for the search of new materials, such as skutterudites [13, 14] and clathrates [15-17], came after the suggestion of Slack [18], where the strong reduction of the thermal conductivity in skutterudites and clathrates was observed while maintaining high electrical conductivity as only phonon propagation was inhibited without impacting much the transport of the electrons, made possible due to the ‘rattling’ motion of loosely bonded atoms within a large cage which generates strong scattering in these materials[9].

1.4.1 State of the art TE materials: from bulk to nano

In 1993, Hicks and Dresselhaus [19, 20] pioneered the idea that quantum confinement of electrons and holes in low-dimensional materials could dramatically increase ZT to values greater than 1 by independently changing $S^2\sigma$.

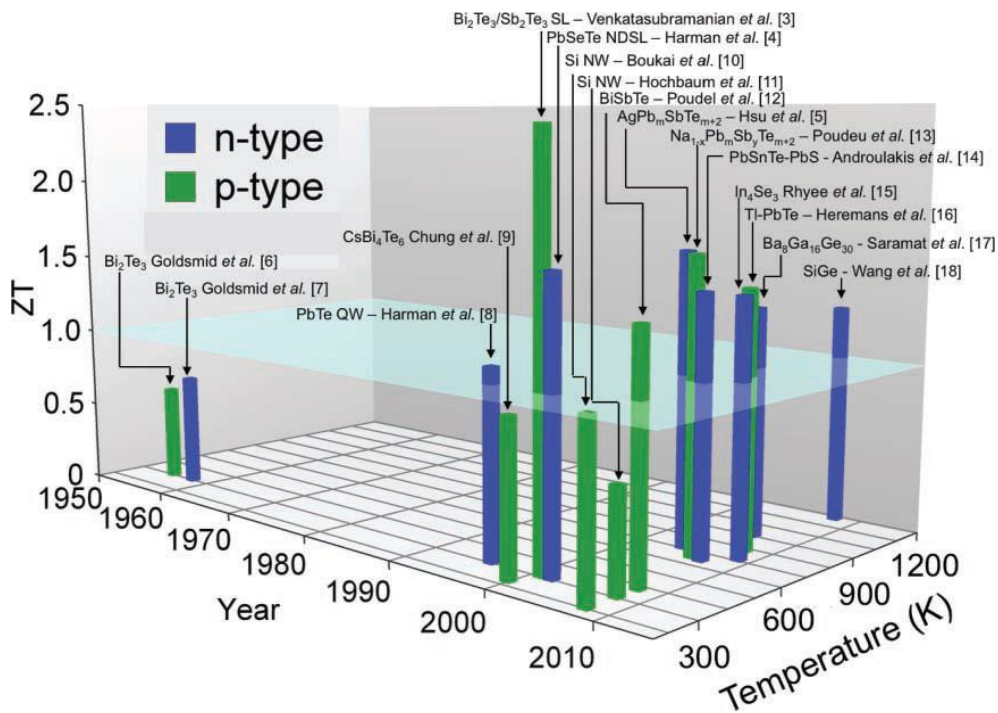


Figure 1.4 Thermoelectric figure-of-merit ZT as a function of temperature and year illustrating important milestones with introduction of nanostructuring [21].

Nanostructured thermoelectric materials have attracted a great deal of attraction but an explanation of the exact role of low dimensionality and nanostructures in the improvement of thermoelectrics is still under discussion. Enhanced performance ($ZT > 1$) in thermoelectrics with low-dimensional structures was reported by several groups, including Venkatasubramanian *et al* [22], Harman *et al*[23], and Hsu *et al* [24]. However, their structures have mainly benefitted from reduced phonon thermal conductivity while quantum confinement of the electronic carriers has not yet been demonstrated to play a role [21].

While the ZT of commercially available bulk thermoelectrics such as Bi_2Te_3 , PbTe and SiGe alloys hovered at ~ 1 for a long time, theoretical predictions [20] in the mid-90s coupled with exciting theoretical and experimental results in compound semiconductor quantum wells [25] and superlattice[22] structures, Si nanowires [26, 27], quantum dot [23] and other nanostructures incorporated in thermoelectric materials [28, 29] indicated the promise of a higher ZT and better energy conversion efficiency.

The majority of research is currently focused on the development of materials based on the perovskites, lanthanum chalcogenides and boron-carbon compound for high-temperature thermoelectric generation with a vision to increase the material figure of merit and the upper

operating temperature of devices. Improvement of the electrical power factor is also important with the introduction of disorder into the alloy structure which was responsible for the reduction of thermal conductivity in these materials [9].

1.5 Different generations of thermoelectric materials

TE materials have been extensively studied since the 1950s. To understand better how we can tune ZT it is important to revisit history. Seebeck, Peltier and Thompson effects were developed on the basis of metals as thermo-elements. However, theoretical predictions for TE devices by Altenkrich stated that metals were inefficient for TE applications [30, 31]. Ioffe investigated III-V and II-VI semiconductors identifying n- and p-type semiconductors to form a prototype TE generator [21]. Goldsmid *et al.* also contributed by finding that the best semiconductor for TE devices was Bismuth telluride (Bi_2Te_3) [32, 33]. These materials are known as the first generation of TEs with an average ZT of about 1.0 and device energy conversion efficiency of 4-6%. In 1980s, Rowe and co-workers proposed that phonon scattering at the grain boundaries may improve TE performance [34]. Later on Dresselhaus *et al.* revisited the nanostructuring concept by explaining how quantum confinement could enhance the power factor $S^2\sigma$ [20]. The generation of nanoscale precipitates, grain boundary inclusions, and compositional inhomogeneity, all helped to reduce the lattice thermal conductivity [15, 35-37]. A wide variety of research activities led to almost doubling the high temperature ZT . This defines the second generation of bulk TEs namely clathrates, half-Heusler alloys, lead tellurides (LAST), and skutterudites. These materials have shown ZT up to 1.7 at high temperatures while the conversion efficiency of devices made from such materials is about 10-12 % [35, 38].

Nowadays thermoelectricity researchers are developing the third generation of TE materials using many cutting-edge approaches to enhance ZT , with values of 1.5 to 2.2 for expected novel materials, which would translate into a 15 % conversion efficiency. On the other hand, some of the recently reported high ZT values have not been independently verified [39-41]. Figure 1.4 and 1.5 illustrates a comprehensive landscape of different TE materials [5]. It describes the revival of TEs with nanostructures that have shown improved TE performance. Most of these materials are not available commercially due to small-scale production, high cost, and complications during device fabrication. Indeed, large quantities of TE materials and efficient design of TE devices are major challenges at present. Several reports have

documented poor mechanical properties of TE materials as well [5, 42]. Due to these challenges, to date only bismuth telluride (Bi_2Te_3)-based TE modules are available in the market for low grade energy harvesting and cooling purposes [43].

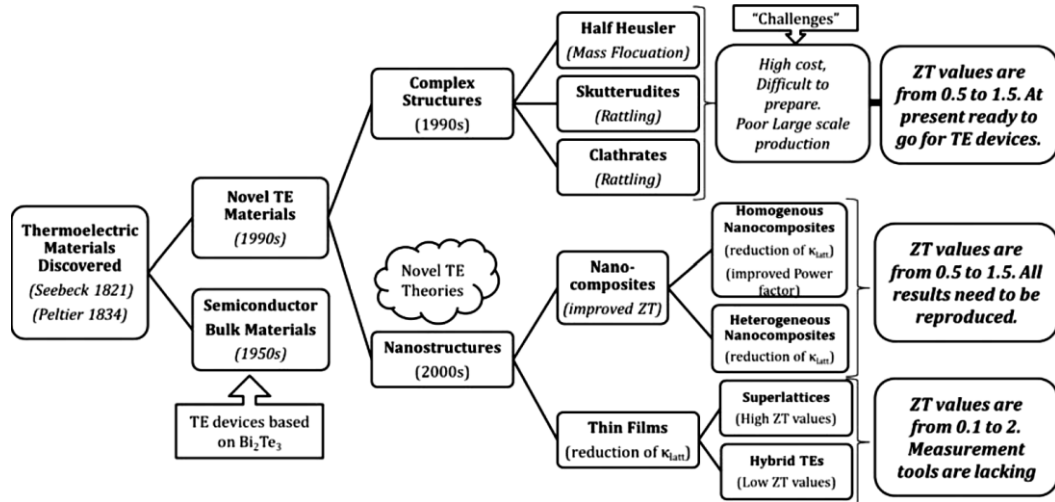


Figure 1.5 Schematic illustration of the current state of the art ZT achievements in bulk TEs[5].

1.5.1 Challenges in thermoelectric research

The primary scope of TE research is to attain improved ZT values. However, over several decades ZT only marginally improved [44]. Unfortunately, there seems to be no single material available in nature that has proven to be a good TE candidate. The major challenge resides in the three interconnected physical properties determining ZT . In order to obtain a high ZT value, S and σ should be high while κ should be reduced [45]. However, their interdependence has led to a limited selection of materials for TE applications, as shown in Figure 1.6 [46]. Metals possess a high σ and a high κ , but the power factor $S^2\sigma$ is rather small. Insulators are poor thermal and electrical conductors, but semiconductors and semi-metals exhibit large thermopower, relatively high σ , and lower κ , which may lead to an optimum ZT value [44].

When TE materials are integrated into devices, new challenges emerge such as coupling the n- and p-type materials with metallic contacts, placing ceramic plates on both ends, and matching the coefficient of thermal expansion of the materials. These are major considerations in the design of a TE device [4]. Packaging is an additional one as some materials are sensitive to air and the device has to be sealed in an inert atmosphere.

Moreover, the configuration plays a role and planar or tubular design may be preferred depending upon the target application [4].

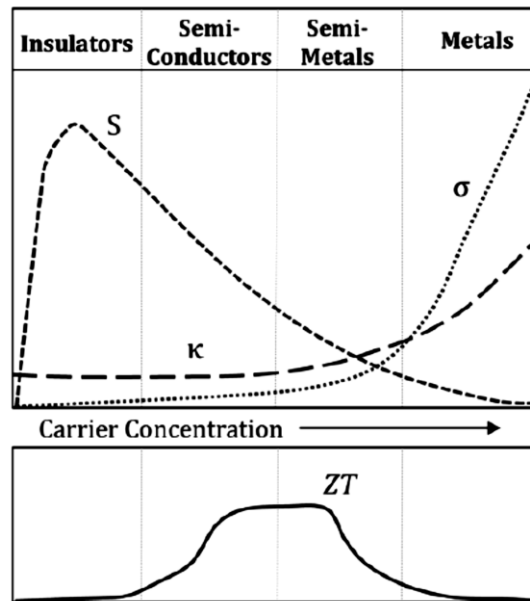


Figure 1.6 Thermoelectric behaviour of different classes of materials[47].

1.6 Oxides as thermoelectric material

In comparison to the major energy conversion technologies operating in air ambient conditions, e.g., combustion engines, concentrated solar radiation sources, or furnaces, the chalcogenides were found to be hardly efficient due to their poor chemical and physical stability at high temperatures, as well as oxidizing conditions, and toxicity [48, 49]. On the contrary under the same conditions, oxides proved to be very robust. Although they are considered as insulators, they can have a high Seebeck coefficient and some of them even have ZT values comparable to semiconducting chalcogenides. Currently, the best performing oxide material exhibits rather low $ZT \sim 0.3$ in poly-crystalline form [50, 51]. But to improve the overall performance of these oxide materials an intense study of their physical properties has to be considered through the effect of synthesis parameters on the microstructure. As an example, experiments with layered-cobalt-oxide single crystals like Na_xCoO_2 and $[\text{Ca}_2\text{CoO}_3]_{0.62}[\text{CoO}_2]$ have shown $ZT > 1$ [52, 53].

Oxide compounds have a great potential among all the thermoelectric materials and can be divided into three main groups: layered complex oxides, doped zinc oxide derivatives, and perovskite-type oxides.

In this thesis the research was carried out with perovskites-type oxides.

Although simple perovskites are normally good insulators with high Seebeck coefficients they have not been considered as very strong TE materials. However due to their advantages, like the possibility to select from a large set of material property combinations, their flexibility due to their constituent elements covering most of the periodic table, perovskites type oxides are being revisited. Thus, through aliovalent cation substitutions fruitful compromises between the lowered S and ρ can be achieved.

Among oxides, the field of transition metal oxides (TMOs) is drawing increasing attention in the field of thermoelectrics as the metal oxides can show a wide range of electronic properties ranging from insulating to semiconducting and conducting and include materials such as titanium, manganese, tungsten, zinc, copper, vanadium, cobalt, rhodium, and molybdenum oxides[54]. Engineering of the electronic and thermal properties of TMOs can be achieved by changing their properties such as morphology, doping and stoichiometry. Tuning of the thermal properties like phonon generation and propagation by the development of molecular engineering methods in TMOs is actively investigated. Additionally, as many TMOs exhibit high Seebeck coefficients, with desired thermal and electrical conductivity and heat capacity, are stable and have interesting thermal properties at high temperatures which can be exploited further for different applications [55-58], but they are yet to achieve their position in practical TE applications.

Figure 1.8 shows the trend in the research field of oxides and how the increase in ZT happened over the years and how there is so much intensive research required in n-type thermoelectric oxides, as p-type oxides with high ZT s exist. However, after Ohta *et al.* reported a high value of 2.4 in a conductive layer between the STO and Nb-doped STO superlattices structure, no further work was reported. This was the challenge that is addressed in this thesis to develop high performance n-type material in STO-based oxide.

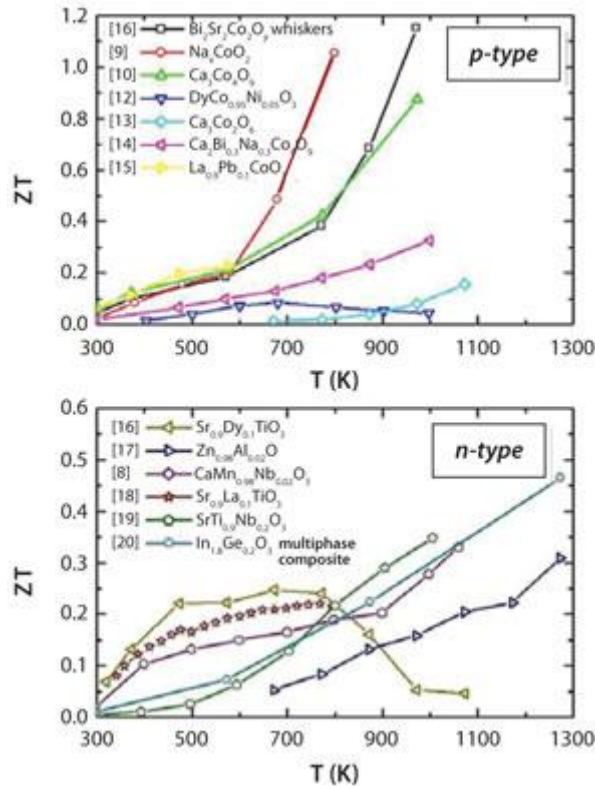


Figure 1.7 Figure of merit, ZT, of selected oxides[59].

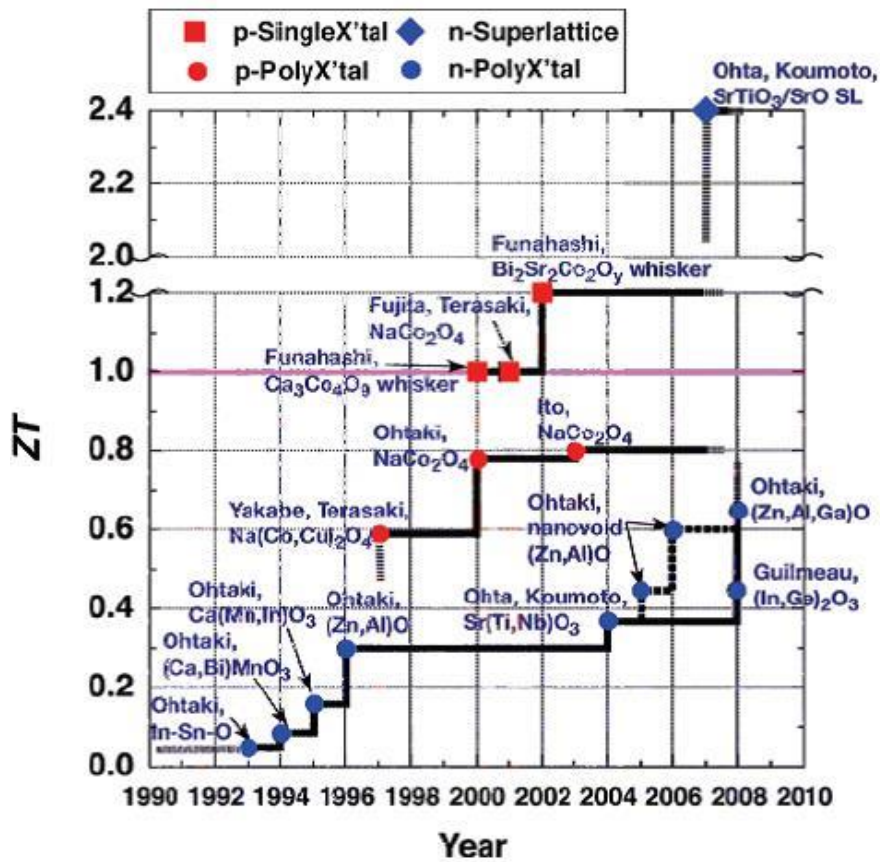


Figure 1.8 The highest ZT oxides over the years[60].

1.7 SrTiO₃ as a promising thermoelectric material

TMOs containing oxides such as Alkaline earth metal titanates ATiO₃ (A = Ba, Sr, Ca) with the perovskite structure are materials of fundamental and technological importance because of a broad range of their novel chemical and physical properties and for at most important for thermoelectric applications. Although the stoichiometric A₂Ti₄O₃ is a band insulator with an energy gap of ~3.20 eV, the tuning of chemical composition allows injection of carriers (electrons) to the conduction band composed mainly of Ti 3d t_{2g} orbitals. This is a very important point to understand since one way to improve the thermoelectric properties is by d band engineering in STO. Doping with aliovalent cation substitutions has been extensively examined, for example, using trivalent cations (e.g., La³⁺) at the A site [61, 62] or pentavalent cations (e.g., Nb⁵⁺ and Sb⁵⁺) at the Ti site [11, 63]. Oxygen deficient perovskite ATiO_{3-δ} has been also studied [64, 65].

Perovskite-type STO-based oxides are mostly realised in three configurations:

- (a) SrTiO₃
- (b) A layered perovskite-type in the Ruddlesden-Popper (RP) phase of STO, i.e., SrO(SrTiO₃)_n (*n* = integer) and
- (c) A SrTiO₃ /SrTiO₃:Nb superlattice.

Although *ZT* values for the single-crystal and polycrystalline ceramics are not above 0.37 at 1000 K, and the largest *ZT* estimated for a conducting thin layer in the SrTiO₃/Nb:SrTiO₃ superlattice has been reported to be 2.4 at room temperature, there is still a great deal of interest in the investigation of the TE properties of perovskite-type STO in the form of single crystals, epitaxial films, and polycrystalline ceramics. There is broad agreement that STO-based oxides are a promising group of *n*-type TE materials because they not only exhibit excellent electronic transport properties, stable at high temperatures as STO has a melting point of 2080°C but are also thermally conductive [11]. However, from the viewpoint of practical applications, the TE performance of the bulk materials is still insufficient, and further improvements are needed. Above 105 K STO exists in an isotropic cubic crystal structure with a lattice parameter *a* = 3.904 Å, and crystal symmetry belonging to a space group *pm3m*.

STO has a strong structural tolerance toward substitutional doping with, e.g., for the A site lanthanide substituting Sr^{2+} (A site) or Nb^{5+} replacing Ti^{4+} (B site), making it possible to increase the carrier density and reach a degenerate state with a relatively high electrical conductivity. Ti $3d$ orbitals of triply degenerate orbitals ($3d_{xy}$, $3d_{yz}$, and $3d_{xz}$) and O $2p$ orbitals form the conduction band and the valence band of the electronic band structure of STO with a band gap of $E_g \sim 3.2$ eV. Thus, the band degeneracy NC is 6, including the spin degeneracy [66-68]. Due to the d -band nature in STO, the effective mass m^* of carrier electrons turns out to be quite large, $m^* = (1.16 \sim 10)m_0$, where m_0 is the free electron mass at rest [69] which helps to achieve a large Seebeck coefficient in STO [70]. Thus, due to the high power factor, i.e., high electrical conductivity and large S in the doped STO single crystal, this oxide could compete with conventional TE materials. The potential of STO as a TE oxide was confirmed by the TE properties of STO single crystals reported by Ohta et al. [71] and Okuda et al. [70]. The ZT values are still below 1 as the highest ZT value reported is ~ 0.1 at room temperature and ~ 0.27 at 1000 K. Thus, the STO single crystal alone is not amenable to applications, mainly because of the rather high thermal conductivity, $\sim 11.0\text{--}3.2\text{Wm}^{-1}\text{K}^{-1}$, in the range of 300 to 1000 K.

One of the highest ZT achieved and reported so far in oxides is 0.37 in a 20 mol% Nb-doped STO film at 1000 K, though there are reports with 40% Nb doping as well but this is one of the highest values obtained in n-type oxides so far [72]. The state of the research on thermoelectricity in STO at the start of this thesis was as follows: Even with heavily doped films, heat transport could not be inhibited and the published results of the state of the art ZT were not reproducible. The highest reported values were recorded in highly complex sample structures grown at very high temperatures. Moreover, the explanations of the high Seebeck coefficient invoked a 2-dimensional electron gas, which led to suspect that the interface between the thin film and substrate played a role.

In this work, we set out to study the optimisation of the thermoelectric properties of Nb:STO by varying doping levels, film thickness, type of substrates and combinations of thin films and multilayers. It will be shown as one of the main results, a ZT of 0.8 at room temperature with only 2 mol% doping concentration in Nb:STO thin films grown by PLD.

A possible approach was conceived to increase further the thermoelectric properties of n-type STO, placing graphene sandwiched between the two most promising oxides investigated in

this thesis, namely, a thin film of STO on LaAlO₃ and LSAT as substrate. Graphene[73, 74], a 2-dimensional (2D) material of sp² bonded carbon atoms, consists of a single-atom-thick layer, the transport properties of which are, nevertheless, highly influenced by the supporting substrate [73, 75, 76]. The thermoelectric properties of graphene have been studied due to its promising electrical and thermal properties [77-81] including the electrical transport in graphene on SrTiO₃[76].

In what follows chapter 2 gives a brief historical overview of thermoelectrics and the issues when considering thermoelectricity in the nanoscale. Chapter 3 provides a description of the methodology including the experimental techniques used and their specification in relation to this work. Chapter 4 presents the results of the research including verification of the results and their discussion. Finally chapter 5 has the conclusions and suggestions for future work.

Chapter 2

Thermoelectricity in nanostructures

In this chapter the main ideas behind the investigation of nanostructuring as a way to maximize the thermoelectric figure of merit are surveyed. After a brief historical overview of the investigated materials and concepts used, we examine the definition of thermal conductivity based on existing models and consider them from the perspective of nanostructures.

2.1 Background

The history of thermoelectricity is marked by different stages of progress as with most technologically relevant discoveries (Figure 2.1). In the 19th century the thermoelectric effects known as Seebeck, Peltier and Thomson were discovered. Alloying and doping were investigated between 1940 to 1960, especially microscopic effects, enabled by the introduction of semiconductors as thermoelectric materials [82]. As introduced in chapter 1, a key indicator of progress in thermoelectric materials, is provided by the thermoelectric figure of merit, namely, $ZT = S^2\sigma/K$ given in Eq. 1.5.

A successful strategy that followed in 1950s was to increase ZT was to modify an already promising compound by introducing point defects through the synthesis of iso-structural alloys. These provide an environment of atomic mass fluctuation throughout the crystal lattice, i.e., disorder, which induced strong phonon scattering and generally lead to significantly lower thermal conductivity. The canonical example of this is the Bi_2Te_3 for which the $\text{Bi}_{2-x}\text{Sb}_x\text{Te}_3$, $\text{Bi}_2\text{Te}_{3-x}\text{Se}_x$ alloys are thermoelectrically superior to the parent compounds. This benefit results mainly from a lower thermal conductivity, $1.5 \text{ Wm}^{-1}\text{K}^{-1}$ compared to $2.4 \text{ Wm}^{-1}\text{K}^{-1}$ in the parent compound, leading to a room temperature $ZT \approx 1$ compared with $ZT \approx 0.6$ for the parent Bi_2Te_3 . The alloys continued to be used today in thermoelectric modules. The impact of alloying is generically exemplified in figure 2.2.

The value of ZT remained close to 1 for few decades until the 90s when a renewed interest in thermoelectrics emerged based on two main strategies: one was the engineering of new bulk phonon glass-electron crystals (PGEC) materials [18, 45, 83] and the other the perception that nanostructuring would yield dramatic improvements by impacting the lattice thermal conductivity [7, 19].

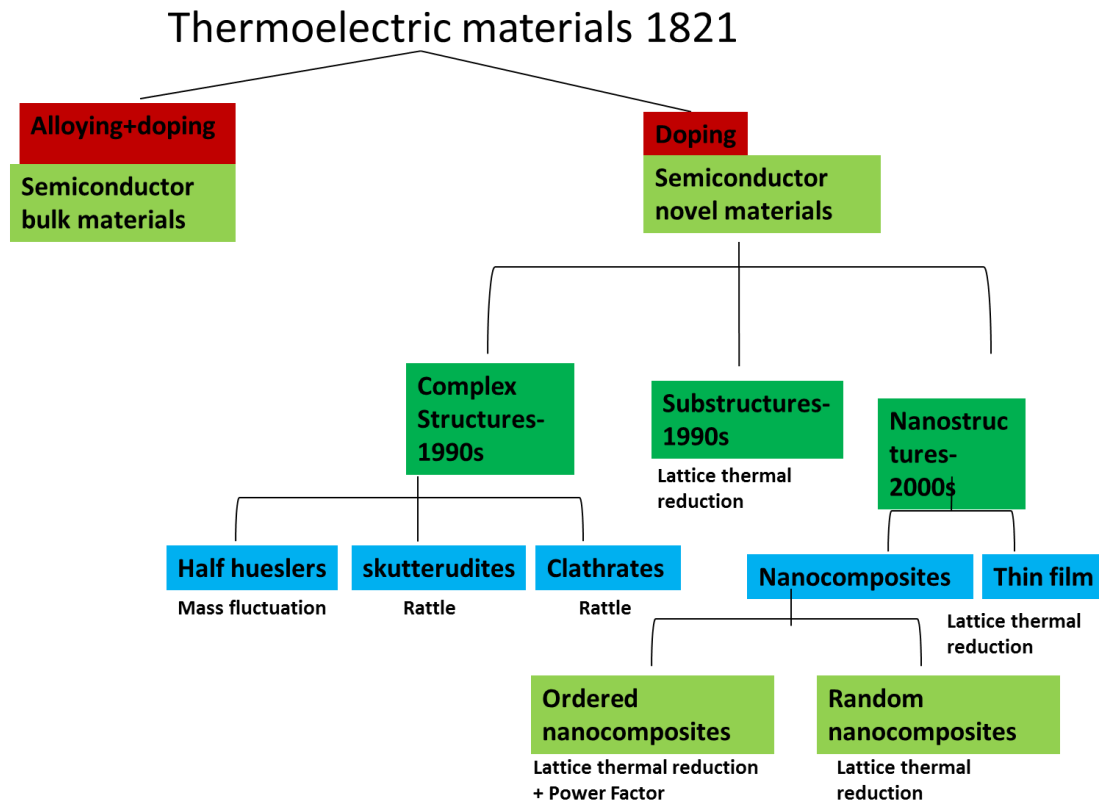


Figure 2.1 Development of thermoelectric materials in time.

Concerning the “phonon glass electron crystal” (PGEC) approach, a PGEC material features cages or tunnels in its crystal structure, inside which there are atoms small enough relative to the atoms forming the “cage” to “rattle”. This situation produces a phonon damping effect that can result in dramatic reduction in the lattice thermal conductivity. In the PGEC picture, a glass-like thermal conductivity can in principle coexist with charge carriers of high mobility. An indication for a “rattling” atom is a highly elevated thermal atomic displacement parameter, although this phenomenon by itself is not sufficient as proof of PGEC. This approach has stimulated a significant amount of new research and has led to increases in ZT for several compounds such as the clathrates.

From the 1990s onwards several materials were reported to exhibit a ZT value above 1, for example, epitaxial multilayers of $\text{Sb}_2\text{Te}_3/\text{Bi}_2\text{Te}_3$ [22] and quantum dot superlattices of PbTeSe dots in a PbTe matrix [23] which reached a ZT of 2.4 and 1.6 at room temperature, respectively. The validation of these strategies launched the renewed interest in thermoelectrics, exploring a myriad of materials and physical concepts as shown in Figure 2.1. In the 1960s and early 1970s, semiconductor nanostructures in the form of quantum

wells and superlattices became popular and showed excellent spatial control of charge and light enabling technologies that were subsequently used for thermoelectrics. Many of these semiconducting, and also oxide, materials and concepts continue to be investigated anchored on specific mechanisms that are expected to affect the thermal conductivity in a controllable manner, such as mass fluctuation, rattles in caged perovskite-like structures, assorted nanostructures varying from ordered to random, creation of a PGEC, etc., all targeting sufficiently high electrical conductivity σ with as small as possible thermal conductivity κ .

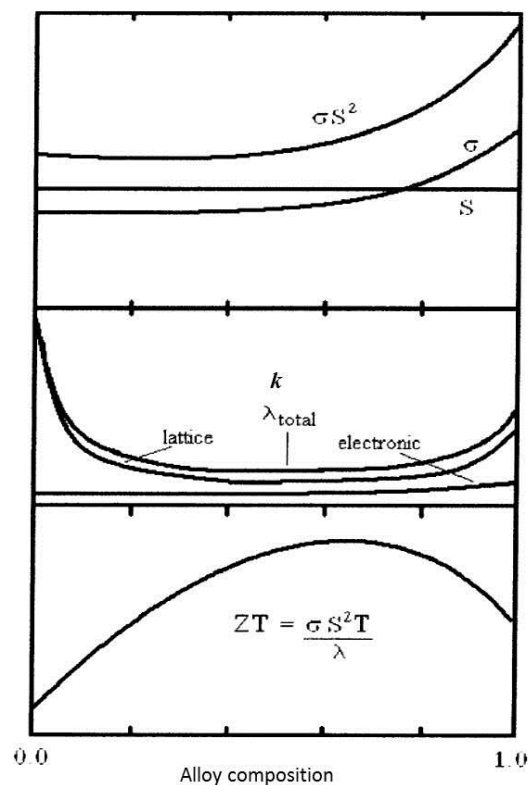


Figure 2.2 Impact of alloying on the ZT as a function of alloy composition for a generic thermoelectric alloy [84].

While each term in ZT (S , σ and κ) can be changed individually over several orders of magnitude, their interdependences have made it extremely difficult to increase ZT above 1 despite five decades of active research. Moreover, the technological drive demands not only a higher ZT but, most importantly, a good power factor (PF), given by $\sigma \cdot S^2$, to make use of these materials in competitive solid-state thermoelectric modules at both low and high temperatures [21].

With values of ZT crossing the barrier of unity, the constant development of new techniques to produce and characterize materials and thermoelectric devices has also spurred theoretical research.

For getting high performance TE Materials we have to either increase electrical conductivity or decrease the thermal conductivity, both of which are interconnected by charge carrier concentration given by the Wiedemann-Franz law

$$K_e = L\sigma T = ne\mu LT \quad 2.1$$

where the Lorenz number is

$$L = \frac{\pi^2}{3} \left(\frac{k_B}{e} \right)^2 \quad 2.2$$

And μ is the charge carrier mobility. There are two factors that contribute to the thermal conductivity of thermoelectric materials i.e., charge carriers (k_e) and thermal conductivity by lattice phonons (k_l) [47]. The contribution of the thermal conductivity by charge carriers is explained by the Wiedemann-Franz law, which is about 1/3 of total electrical conductivity in thermoelectric materials. This is also one of the reasons for the selection of the semiconductors as the material of choice for thermoelectrics.

According to the Keyes model [85], the expression for the lattice thermal conductivity in non-metals is dominated primarily by phonon-phonon scattering as given by:

$$k_{\text{latt}} T = R^{3/2} / \gamma^2 \epsilon^3 N_0^{1/3} T_m^{3/2} \rho^{2/3} / A^{7/6} \quad 2.3$$

where T_m is the melting point, A is the mean atomic weight, γ is the Grüneisen parameter, ϵ is the fractional amplitude of interatomic thermal vibration, R is the ideal gas constant, N_0 is Avogadro's number, and ρ is the density. Equation 1.1 offers some useful insight into thermal conductivity:

- 1) In the high temperature range k_{latt} follows a $1/T$ law,
- 2) A low melting point can lead to a low thermal conductivity,
- 3) k_{latt} decreases with increasing atomic mass, and
- 4) The proportionality to $\rho^{2/3}$ makes k_{latt} low for crystals with large interatomic distances.

Equation 2.3 is a very useful equation when addressing thermal conductivity in low dimensional structures.

The first thermal conductivity models for bulk systems [86-88] were based on the solution of the phonon Boltzmann transport equation (PBTE) under the single mode relaxation time approximation. This approach provides the simplest picture of phonon interactions considering that each phonon mode has a single relaxation time independent of others modes, i.e., it assumes that all other phonons are in their equilibrium distribution[89]. The calculation of the thermal conductivity in semiconductor material implies the knowledge of three major frequency-dependent parameters: specific heat, C_V , phonon group velocity, v_g , and the phonon mean free path, Λ . The expression for the thermal conductivity from the kinetic theory of gases is given by:

$$\kappa = \frac{1}{3} C_V v_g \Lambda \quad 2.4$$

Above the Debye temperature, C_V approaches the classical value of $3R$, making κ_{latt} primarily depend on Λ which is determined by phonon-phonon scattering.

Taking into consideration the contribution of each phonon mode q with transverse (T) or longitudinal (L) polarizations, Equation 2.2 becomes:

$$\kappa = \frac{\hbar^2}{3VK_B T^2} \sum_{qs} v_{qs}^2 \omega_{qs}^2 \tau_{qs} n_{qs} (n_{qs} + 1) \quad 2.5$$

where \hbar is the reduced Planck's constant, V the total volume, T the temperature, K_B is the Boltzmann constant, ω_{qs} the phonon frequency, v_{qs} the group velocity, n_{qs} the Bose-Einstein equilibrium phonon distribution function and τ_{qs} the total relaxation time of each mode. From equation 2.5 it is clear that to model the lattice thermal conductivity we need the dispersion relation, the total relaxation time of each mode and a numerical scheme for the integration within the Brillouin zone. The phonon dispersion relation can be calculated by several methods. However, the calculation of the intrinsic relaxation time and the summation over the Brillouin zone can be very time-consuming. Furthermore, knowledge of the anharmonic phonon-phonon scattering strengths is not yet sufficiently well-established [90].

2.2 Nanoscale thermal conductivity

Recent experimental and theoretical reports point to an enhancement of the thermoelectricity figure of merit, $ZT = S^2 \sigma / KT$, in thin films [38, 91-93], nanowires [26, 27, 94, 95], superlattices [96, 97] and suspended phononic crystals [98, 99]. This is explained primarily a result of the thermal conductivity decrease compared to the bulk counterpart, without a

corresponding decrease in electrical properties. The reduction of the thermal conductivity in these studies has been associated mainly with two factors:

- (i) The modification of the acoustic dispersion relation due to the additional periodicity (superlattices and phononic crystal structures) [100-102] or spatial confinement of the phonon modes (thin films and nanowires) [103-105] and,
- (ii) The shortening of the phonon mean free path due to the diffuse scattering of phonons at the boundaries [106-108].

To model heat transport in nanostructures, advanced theoretical models are required which correctly take into account the frequency dependence of phonon properties. The majority of thermal conductivity models are derived from the phonon Boltzmann transport equation under the single mode relaxation-time approximation [17]. For low-dimensional systems Zou *et al.* [109] classified the theoretical models into three types. The first one takes the bulk formulation for the thermal conductivity, introduces the modified dispersion relation caused by the spatial confinement and adds a boundary scattering rate to the total scattering rate through Matthiessen's rule [103]. The second model uses the bulk dispersion relation and derives an exact solution of the PBTE after introducing the diffusive boundaries conditions, according to a Knudsen flow model [106, 110]. The third model, proposed by Zou *et al.* [109], is a combination of these previous two approaches. This model takes the modified expression of the thermal conductivity, including the Knudsen flow model, in addition to the modified dispersion relation and phonon anharmonicity. More recently Huang *et al.* [105] developed 1- and 2-dimensional expressions for the thermal conductivity of nanowires and thin films, which include a modified expression of the relaxation time due to the boundaries.

Thus it is seen that there is much to be understood about thermal conductivity in nanostructured materials. In this thesis we will focus on preparing and measuring novel oxide structures, with the methods described in chapter 3 considering the assumptions made in the various approaches mentioned above when analyzing the data.

2.3 Considerations to optimize material parameters

Despite the linear dependence of the power factor (PF) on electrical conductivity, it is not always advantageous to have a high conductivity because this increases the electronic contribution of k according to the Wiederman– Franz (WF) law ($k_e = L\sigma T$, where L is the

Lorenz number) as explained in section 2.1. For metals and degenerate semiconductors the Lorenz number is taken to be $2.45 \cdot 10^{-8} \text{ W}\Omega\text{K}^{-2}$, however it can vary depending on temperature and material. According to WF law the electrical conductivity scales linearly with the carrier thermal conductivity k_e and thus very high electrical conductivities ($>2000 - 3000 \text{ Scm}^{-1}$ at room temperature) may not be appropriate. While in this thesis we research oxides, we will see in chapter 4, that sometimes the carrier densities are well within the semiconducting regime and, therefore, these considerations may become relevant.

Let us consider the total thermal conductivity of the best thermoelectrics used at present for power generation applications, say, n-type PbTe with a total thermal conductivity of $1.3 \text{ Wm}^{-1}\text{K}^{-1}$ at 700 K. For optimized samples, about $0.15 \text{ Wm}^{-1}\text{K}^{-1}$ of this value is due to k_{el} , which arises from an electrical conductivity of approximately 200 Scm^{-1} at 700 K. Therefore, for every 200 Scm^{-1} increase in conductivity, the thermal conductivity is burdened with an additional $0.15 \text{ Wm}^{-1}\text{K}^{-1}$ (at 700 K). This illustrates the importance of compromises for specific applications, as only considering the electrical conductivity places severe constraints on the magnitude of the lattice thermal conductivity to achieve high ZT.

Chapter 3

Experimental Techniques

In this chapter the various experimental and characterization techniques and their working principles are explained in detail together with the specifications and parameters used in this thesis.

3.1 Pulsed laser deposition: Sample Preparation Fabrication Technique

The samples grown for this work was prepared by pulsed laser deposition (PLD) which is a versatile technique used for deposition of a wide range of materials for several reasons, which not only the energy source in the chamber is located outside the chamber, but also the use of ultrahigh vacuum (UHV) and ambient gas combined with a stoichiometry transfer between target and substrate and its pulsed nature that allows depositing high-temperature superconductors, oxides, semiconductors, metals and even polymers or fullerenes along with multilayers. Tuning of the film properties such as stress, texture, reflectivity, magnetic properties, etc. is possible by the deposition in an inert gas environment and varying the kinetic energy of the deposited particles. Due to all these reason PLD becomes an attractive deposition technique for the growth of high-quality thin films [111].

For the first time PLD was used by Smith and Turner [112] in 1965 for the preparation of semiconductors and dielectric thin films and was finally established by Dijkkamp and co-workers [113] to grow high-temperature superconductors in 1987. Their work demonstrated the main characteristics of PLD which are the stoichiometry transfer between target and the deposited film and high deposition rates of about 0.1 nm per pulse.

Versatility of the PLD technique

By changing first the laser parameters such as laser fluence, wavelength, pulse duration and repetition rate a strong influence on the film properties can be observed. They can also be influenced by the growth conditions such as, target-to-substrate distance, substrate temperature, background gas and pressure. Some of these conditions are explained below which are also important for the growth of the thin films and multilayers used in this work:

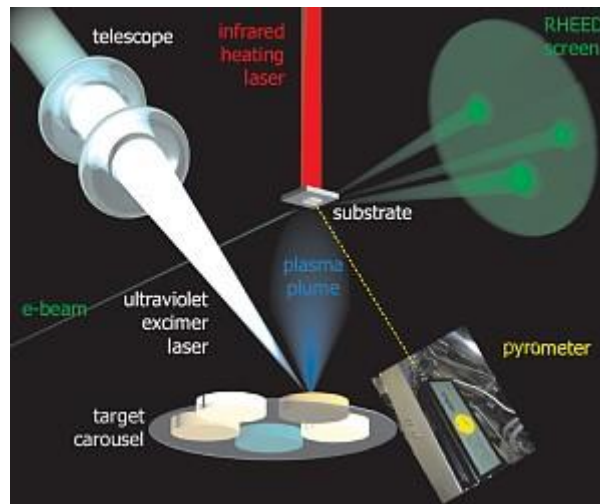


Figure 3.1 Pulsed Laser Deposition with RHEED

UHV and different gas atmospheres

Table 3.1, shows a non-exhaustive list of materials deposited for the first time after 1987. Along with the growth of other materials, during the growth of oxides, oxygen is used often to incorporate a sufficient amount of oxygen. For example, an oxygen pressure of about 0.3 mbar is necessary for the formation of perovskite structures at high substrate temperatures [113]. In other techniques its difficult to prepare such samples, for instance, in case of sputtering its only possible to introduce oxygen or nitrogen in special oven facilities close to the substrate surface as commonly argon is used as background gas in this technique.

Material		Literature
High-temperature superconductors	YBa ₂ Cu ₃ O ₇	Dijkkamp et al. (1987)
	BiSrCaCuO	Guarnieri et al. (1988)
	TlBaCaCuO	Foster et al. (1990)
	MgB ₂	Shinde et al. (2001)
Oxides	SiO ₂	Fogarassy et al. (1990)
Carbides	SiC	Balooch et al. (1990)
Nitrides	TiN	Biunno et al. (1989)
Ferroelectric materials	Pb(Zr,Ti)O ₃	Kidoh et al. (1991)
Diamond-like carbon	C	Martin et al.(1990)
Buckminster fullerene	C ₆₀	Curl and Smalley (1991)
Polymers	Polyethylene, PMMA	Hansen and Robitaille (1988)
Metallic systems	30 alloys/multilayers	Krebs and Bremert (1993)
	FeNdB	Geurtsen et al. (1996)

Table 3.1 List of some materials deposited for the first time by PLD since 1987 [111].

Small Target Size

Complex samples for research purposes can be achieved by PLD as the spot size of the focused laser beam is small and also the target area may even be less than 1 cm^2 . The flexibility of the PLD technique helps if the sample or one component is expensive for the required growth due to the possibility of easily exchanging and adjusting the targets.

Stoichiometry transfer

The stoichiometry transfer between the target and substrate and the preservation of that stoichiometry in the deposited film has made PLD quite popular to grow complex systems, for instance, in high temperature growth of perovskite structures and samples for technical applications like sensors, etc. in comparison to other sputtering or evaporation techniques where stoichiometry transfer is obtained with difficulty, the reasons for stoichiometry transfer in PLD can be explained by two main reasons:

- a. Energetic Particles:** For the deposition of metallic materials in UHV, high ablation rates (on the order of 0.01 nm per pulse) with laser fluences of more than 5 J/cm^2 are necessary as then only the film deposition with energetic particles can take place. At a laser fluence of 8 J/cm^2 the velocities of the plasma plume expansion correspond to average kinetic energies of the ablated ions of more than 100 eV [114] in agreement with results of Lunney [115]. In the literature, the higher energies of the ablated ions are due to the acceleration of the ions in the strong space charge field by the more mobile electrons, which collectively move away from the ions [116].
- b. Tunable Particle Energy:** Varying the kinetic energy of the deposited particles from an average energy of 50 to about 150 eV for metallic systems can be achieved by increasing the laser fluence from 2 to about 10 J/cm^2 which will change the film properties slightly. The energy can be reduced to below 1 eV when the particle energy is lowered by an inert gas pressure and the film properties will have a much stronger influence [111].

3.2 STO sample growth

A KrF excimer laser (Lambda Physik) with a wavelength of 248 nm was used as the ablation source. The excimer laser functions by energizing an excimer premixed gas (KrF with an inert buffer) with a high voltage, which creates a short lived dimer species from the premix

gas. When the dimer decomposes, the characteristic wavelength light is released. The laser light is then directed through a focusing lens with adjustable position and onto an ablation target inside a vacuum chamber. Typical base pressure for ablation is in the high vacuum range about 10^{-6} Torr. During ablation, the target can be rastered and rotated for even ablation. Ablation creates a plume of plasma and vapour which is released orthogonally from the surface of the target. This plume is directed onto a substrate, which is typically heated and crystalline. Gases can be added to the vacuum chamber to control growth characteristics and serve as reactants with the plume.

Before each ablation, the laser energy is measured via an Orion hand-held photo detector. If the laser energy is within an acceptable range (100 to 150 mJ) the experiment can proceed. Otherwise the premixed gas is replenished via an automated refilling procedure. After measuring the laser energy, the energy density can be calculated dividing it by the laser spot area.

The spot size is measured directly using UV-fluorescent laser paper. The position of the focusing lens is adjusted to set the desired energy density for the measured laser energy. Laser repetition rate can also be specified. For a given set of experimental parameters (laser energy density, repetition rate, chamber pressure and substrate temperature) a step sample is made via masking technique. In this way, a desired film thickness can be selected by choosing the corresponding number of laser pulses.

Prior to all PLD experiments, the chamber is cleaned with acetone and laboratory grade tissue paper. Blank (un-patterned) substrates are dried under flowing nitrogen and placed on the substrate heater using silver paint. Ablation targets are mounted onto target holders. Once the target and substrate are mounted in the vacuum chamber, a turbo molecular pump with a rotary vane backing pump is used to draw high vacuum. Once under vacuum, the targets are pre-ablated with 1000 pulses of the laser at a frequency of 8 Hz to remove oxides or other contaminants from the target surface. During pre-ablation the substrate is covered by a moveable shield. Process conditions vary for the desired final product, however, film roughness, crystallographic orientation, or physical properties are the typical factors to optimize in the deposited film. Films were deposited directly onto the cleaned substrates at elevated temperature, either in high vacuum or a reaction gas.

We deposited thin films and multilayers by optimising the growth conditions, i.e., keeping the temperature at 1200K and vacuum within 10^{-2} - 10^{-3} mTorr with laser energy of 100 mJ and deposition rate of 1p/sec with proper toggling and rotation. The samples used in most of this work were grown by PLD with the optimized conditions as specified above. The samples were thin films of various thicknesses on various substrates (LaAlO₃, LSAT, SrLaAlO₄, DyScO₃, SiO₂ and MgO). Multilayers were also grown using the doped and undoped target of STO under the same optimized conditions. Representative samples which were studied in this thesis are listed in table 3.2.

Sample name	Thickness(nm)
2 mol% Nb-STO/LaAlO ₃	30
2 mol% Nb-STO/LaAlO ₃	66,
2 mol% Nb-STO/LaAlO ₃	99,
2 mol% Nb-STO/LaAlO ₃	160
2 mol% Nb-STO/LaAlO ₃	165
2 mol% Nb-STO/LaAlO ₃	200
5 mol% Nb-STO/LaAlO ₃	50
15 mol% Nb-STO/LaAlO ₃	50
2 mol% Nb-STO/LSAT	50
2 mol% Nb-STO/SLAO	50
2 mol% Nb-STO/SLAO	66
2 mol% Nb-STO/DyScO ₃	50
2 mol% Nb-STO/DyScO ₃	66
5×[2 mol% Nb-STO]/LSAT	160
5×[2 mol% Nb-STO]/LaAlO ₃	160
C	50
2 mol% Nb-STO-Gr/ LaAlO ₃	50
3×[2 mol% Nb-STO-Gr]/LaAlO ₃	160
2 mol% Nb-STO/MgO	10
2 mol% Nb-STO/MgO	60
2 mol% Nb-STO/MgO	140
2 mol% Nb-STO/MgO	424

Table 3.2 List of samples deposited using PLD in my thesis.

3.3 Structural characterization techniques

3.3.1 XRD (X-Ray Diffraction)

The principle of the X-Ray diffraction (XRD) is based on Bragg's law i.e., when an X-ray beam hits a crystal surface at an angle θ , it gets reflected by the crystal planes (see Figure 3.2). Depending on the phase of the incident and diffracted beams, the interference could be constructive or destructive. Geometrically speaking, the path difference between the incident and the reflected beam from two parallel planes in the crystal arises due to the specular reflection from a crystal with an interplanar spacing d and it has to be equal to an integer multiple of the X-ray wavelength. In this case, the beams are in phase and the path difference is obtained from i.e.

$$n\lambda = 2d\sin\theta \quad 3.1$$

where λ is the X-ray wavelength, θ is the incident angle and n is an integer (1,2,3...).

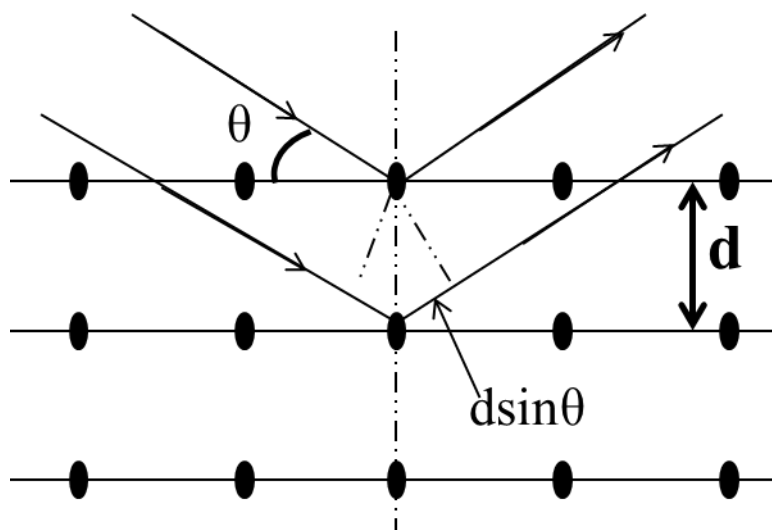


Figure 3.2 Illustration of X-ray diffraction from lattice planes in an ordered material. The diagram illustrates the relation between incident angle and lattice plane separation known as Bragg's law.

In a crystal structure there could be diffraction from multiple planes of atoms with different intensities as a function of the angle called Miller indices. The interplanar spacings are dependent on either the Miller indices, or the diffracting planes, and the lattice parameter of

the structure. We can rewrite Bragg's law as $n\lambda = 2d_{hkl}\sin\theta$ for a particular interplanar spacing where d_{hkl} is the Bragg lattice.

In this work XRD was performed using a Panalytical Xpert Pro XRD. Samples were mounted using modeling clay and manually centered and rotated for maximum diffraction intensity. X-ray analysis provided the crystallographic analysis of films.

High resolution XRD of the thin films was carried out in a 4X Ge (220) monochromator. Following Bragg's law, where λ is the wavelength of the interrogating x-rays, which for Cu $K\alpha_1$ is 1.54059 Å. The measured angle of diffraction θ is obtained from the XRD experiment, and is used in the Bragg equation to solve for d , the lattice spacing. Changes in lattice spacing and relative intensity of diffraction peaks are used to determine the extent of crystallization and changes in composition or morphology. The lattice parameters are calculated for the thin films using the reciprocal space map obtained by XRD by the following equations:

$$\begin{aligned} a &= n\lambda / 2Q_x & c &= n\lambda / 2Q_y & 3.2 \\ (Q_x &= \sin\theta \sin(\theta-\omega) & (Q_y &= \sin\theta \cos(\theta-\omega) \end{aligned}$$

Where a is the in-plane and c is the out-of-plane parameters of the epitaxial film and ω is the rotating axis for the measurement. From the reciprocal space map and knowing the lattice constants of the substrate we can easily establish whether the film is strained or relaxed in a quantitative manner. (Figure 3.3)

The relative positions of reciprocal lattice points change depending on lattice matching and the presence or absence of lattice relaxation. The term lattice relaxation can be understood in two ways. If there is a mismatch between equilibrium structures of film and substrate the film may grow coherently with the substrate lattice and accommodate the difference in in-plane lattice parameters at the interface up to a critical thickness, and the film grows in a strained state. In the other way, the progressively larger accumulated elastic energy due to strain could be released forming defects, or any other plastic deformation mechanism. In such conditions the strain in the film is (partially) released as shown in Figure 3.3.

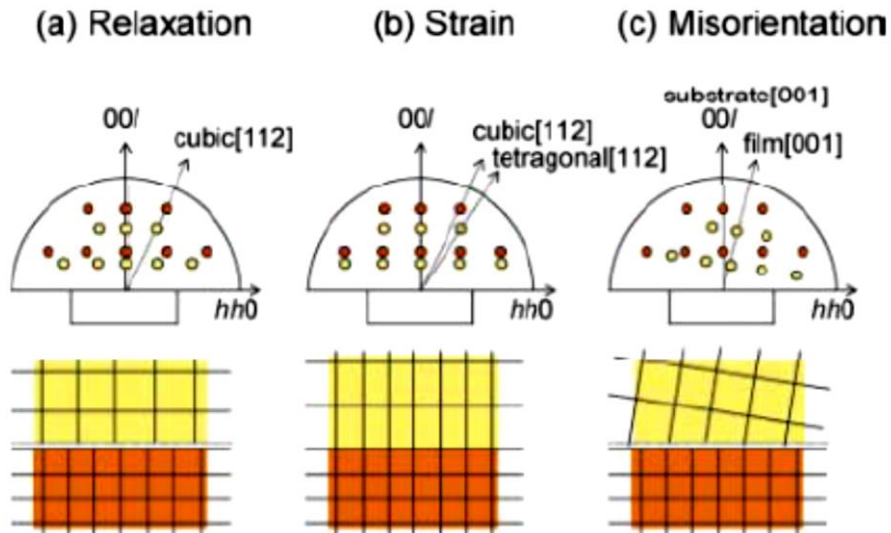


Figure 3.3 Reciprocal space maps of heteroepitaxial layers.

Thickness determination using XRR data from XRD measurements

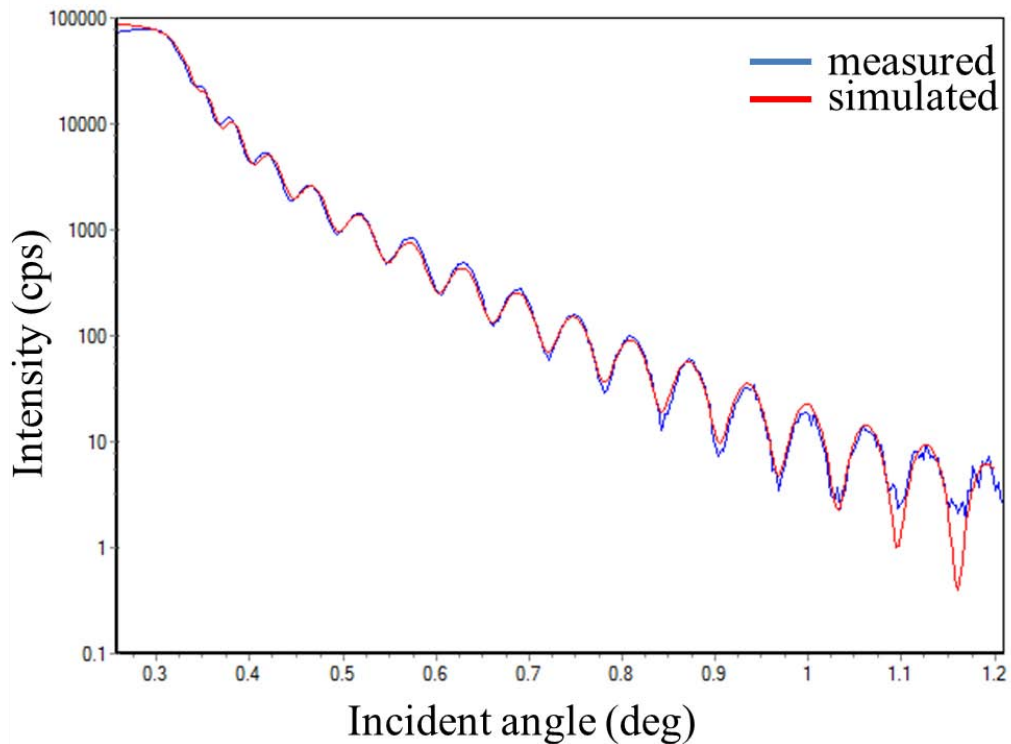


Figure 3.4 Reflectometry map using XRR for a Nb-STO/LAO 66 nm thick film.

XRR of the films was obtained by measuring the X rays reflections from the thin film sample at different angles and satisfying the condition $2\theta/2$ of the Cu K α radiation with a monochromator. Working in the θ - 2θ mode we assure that the incident angle is half the diffracted angle. For incidence angles θ below the critical angle θ_c , the penetration depth is a few nanometres only but above θ_c the depth increases rapidly. We record the thickness fringes due to the interference between the X-ray beams scattered from the different interfaces wherever the electron density changes and these fringes have maxima intensity, i.e., constructive interference and minima due to the destructive interference. The period of the interference fringes and the decrease in intensity are related to the thickness of the film. We also perform the simulation as well using X'pert pro reflectivity software to recheck the calculated data. Figure 3.4 shows an example of a 66 nm Nb-doped STO film on LAO substrate and comparing the simulated and measured reflectivity of the thin film.

Calculation of lattice parameters

The in-plane and out-of-plane (a and c , respectively) are determined by measuring the angular position of the -103 reflection of Nb-doped STO film in reciprocal space using the X-Ray diffractometer. For growth of a good epitaxial film, it is very important to understand how the lattice parameter of film behaves compared to the substrate which will be explained further in chapter 4. Here in figure 3.4 we show an example of 66 nm film of Nb doped STO on LAO substrate and we can easily see that it's not strained. We calculate the $a= 3.9022 \text{ \AA}$ and $c= 3.9462 \text{ \AA}$ which are near to the bulk value of crystalline STO, i.e., 3.90 \AA . Due to the compressive strain in the films, the thinner films are strained and in the thicker the strain relaxes and reached the bulk value of Nb-doped STO as will be shown in the results of 2% doped Nb:STO thin films in Chapter 4.

3.3.2 Electron Microscopy

We have used TEM and HRTEM for the atomic scale structural characterisation of the films. The principle of TEM is similar to their optical counterparts, the optical microscope. In TEM, a focused beam of electrons is used to "image" and achieve information about the structure and composition of the specimen. An electron source produces a stream of electrons which are accelerated towards the specimen using a positive electrical potential. Using metal apertures and magnetic lenses (condenser lenses) this stream is focused into a thin, focused,

monochromatic beam. The beam strikes the specimen and a part of it is transmitted. This portion of the beam is again focused by a set of lenses (objective lenses) into an image. This image is then fed down the column through the intermediate and projector lenses, to enlarge it, depending on the set magnification. A phosphor image screen is used to produce the image. The image strikes the screen and light is emitted, thus enabling the user to see the image. The darker areas of the image represent the thicker or denser region of the sample (fewer electrons were transmitted) and the lighter areas of the image represent those areas which are thinner or less dense (more electrons were transmitted).

A main advantage of TEM over other microscopes is that it can simultaneously give informations in real space (in imaging mode) and reciprocal space (in diffraction mode). The ICN2 instrument (FEI Company, Model: Tecnai G2 F20 HRTEM) has a single tilt stage with a maximum tilt angle of -10° to $+10^{\circ}$ in the goniometer. The instrument can operate in bright-field, dark-field, high resolution, SAED and CBED modes. TEM is fitted with a Gatan digital camera for digital image processing. The instrument has a maximum magnification of 1.5 million, and an ACD (anti contamination device) working at liquid nitrogen temperature, helps to keep the filament free from contamination caused by volatile sample.

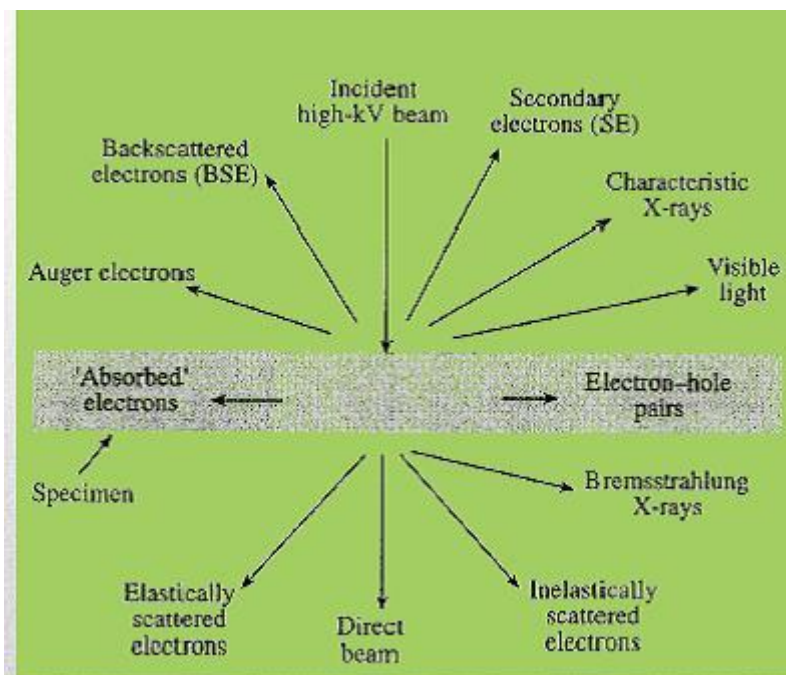


Figure 3.5 The interaction of electron beam with the sample in TEM.

An Ultra-high resolution scanning transmission electron microscope fitted with a high angle annular dark field (HAADF) detector was used to image the sample to inspect the

incorporation of Nb, defects and grain boundaries in thin films grown on LAO substrates. Figure 3.5 shows the system installed in the Advanced Microscopy Laboratory, Zaragoza. A high brightness gun (60-300 kV) was used with monochromator (Wien Filter, $\Delta E < 0.2$ eV) and a STEM resolution of < 1 Å (BF, ADF, HAADF). The samples were prepared for TEM measurements by FIB (Focused Ion Beam).

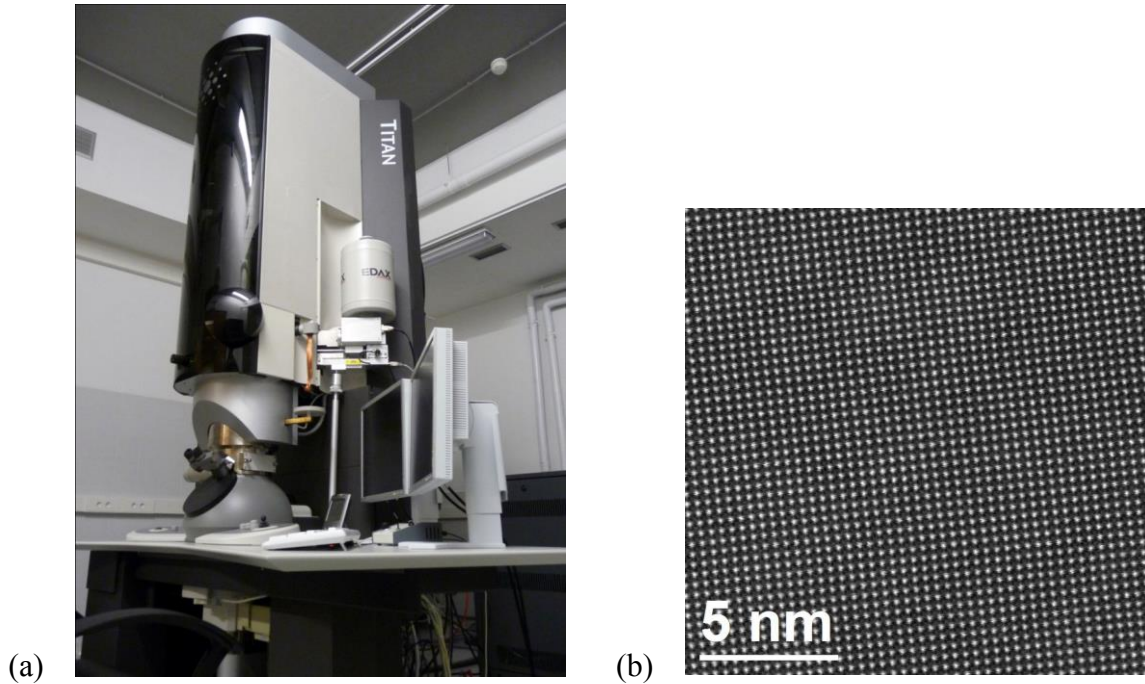


Figure 3.6 HRTEM (a) FEI TITAN low base instrument. (b) Example of the quality TEM images of the reference LaAlO_3 substrate.

3.3.3 Energy-dispersive X-ray spectroscopy (EDS)

Energy-dispersive X-ray spectroscopy (EDS or EDX) is an analytical technique used for the elemental analysis or chemical characterization of thin films. It relies on the interaction of X-ray excitation with a sample[117]. The working principle is the excitation of an electron in an inner shell by an incident beam, ejecting it from the shell and creating an electron hole pair. The energy difference between the higher-energy shell and the lower energy shell may be released in the form of an X-ray when an electron from an outer higher-energy shell fills the hole. The number and energy of the X-rays emitted from a specimen can be measured by an energy-dispersive spectrometer as the energy of the X-rays which is due to the difference in energy between the two shells, and of the atomic structure of the elements from which they

were emitted. We used this technique to determine the elemental compositions of the thin films. An example of an EDX spectrum is shown in Figure 3.7 in which Ka and Kb of elements like Fe, O etc are shown which are the energies when the electron is ejected from innermost K shell to L shell we get Ka and when its ejected from K to L shell we get the Kb and different peaks corresponds to the difference between the shells and the atomic structure of the element from which they are emitted.

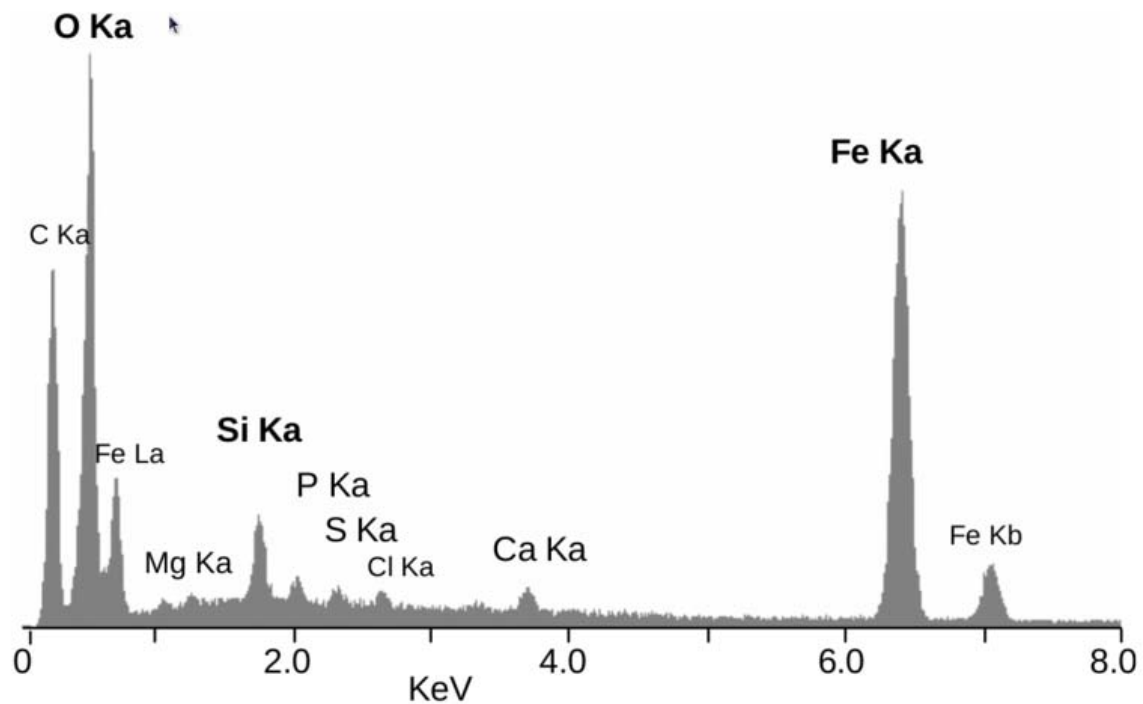


Figure 3.7 Example of a EDX spectrum

3.3.4 X-Ray Photoelectron Spectroscopy

X-ray photoelectron spectroscopy (XPS) is a surface-sensitive quantitative spectroscopic technique that measures the elemental composition in the parts per thousand range, depending on the empirical formula, chemical state and electronic state of the elements of a material. XPS spectra are obtained by irradiating a material with a beam of X-ray beam while simultaneously measuring the kinetic energy and number of electrons that escape from the top 0 to 10 nm of the material under analysis. In XPS, the working principle includes photoemission, i.e., the ejection of an electron from a core level by an X-ray photon of energy $h\nu$. The energy of the emitted photoelectrons is then analysed by the electron spectrometer and the data presented as a graph of intensity (usually expressed as counts or counts/s) versus

electron energy - the X ray induced photoelectron spectrum. The kinetic energy (E_K) of the electrons is the experimental quantity recorded by the spectrometer, which is dependent on the photon energy of the X-rays employed and, therefore, is not an intrinsic material property. Infact, it is the binding energy of the electron (E_B) the parameter that identifies the electron specifically, both in terms of its parent element and atomic energy level. The relationship between the parameters involved in an XPS experiment is:

$$E_B = h\nu - E_K - W \quad 3.3$$

where $h\nu$ is the photon energy, E_K is the kinetic energy of the electron, and W is the spectrometer work function. Since all three quantities on the right-hand side of the equation 3.3 are known or measurable the binding energy is easily obtained [118]. XPS requires high vacuum ($P \sim 10^{-8}$ mbar) or ultra-high vacuum (UHV; $P < 10^{-9}$ mbar) conditions, although a current area of development is ambient-pressure XPS, in which samples are analyzed at pressures of a few tens of mbar.

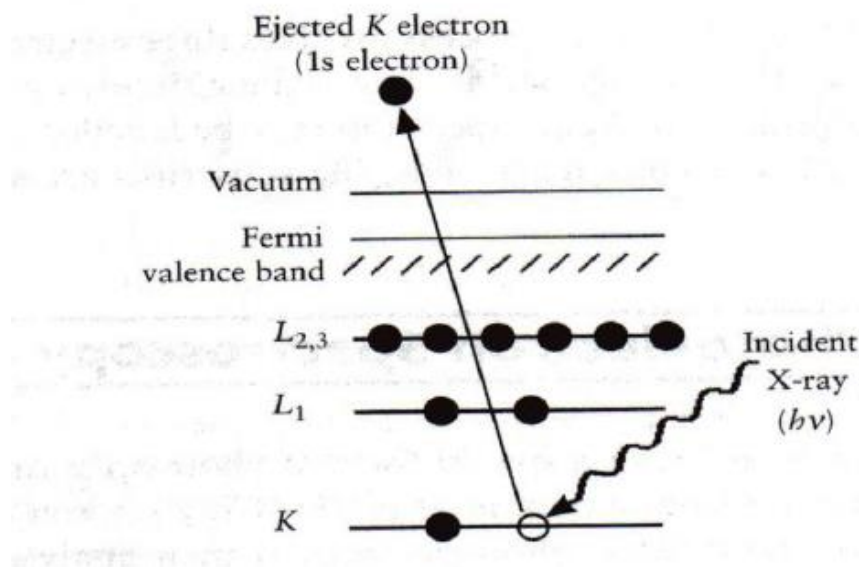


Figure 3.8 Schematic diagram of the XPS process showing the photoionization of an atom by the ejection of a 1s electron[118].

A typical XPS spectrum is a plot of the number of electrons detected (sometimes per unit time) (y-axis) versus the binding energy of the electrons detected (x-axis). Each element produces a characteristic set of XPS peaks at characteristic binding energy values that directly identify each element that exists in or on the surface of the material being analyzed. These characteristic spectral peaks correspond to the electron configuration of the electrons

within the atoms, e.g., $1s$, $2s$, $2p$, $3s$, etc. The number of detected electrons in each of the characteristic peaks is directly related to the amount of element within the XPS sampling volume. To generate atomic percentage values, each raw XPS signal must be corrected by dividing its intensity (number of electrons detected) by a "relative sensitivity factor" (RSF), and normalising it over all the elements detected. Since hydrogen is not detected, these atomic percentages exclude hydrogen.

To count the number of electrons during the acquisition of a spectrum with a minimum of error, XPS detectors must be operated under ultra-high vacuum (UHV) conditions because electron counting detectors in XPS instruments are typically one meter away from the material irradiated with X-rays. This long path length for detection requires vacuum. We have used the XPS ((SPECS PHOIBOS 150) with a base pressure of 1×10^{-10} mbar using monochromatic Al K_{α} radiation (1486.74 eV) as excitation source to determine the atomic composition of the thin films.

3.3.5 Atomic Force Microscopy

The AFM consists of a cantilever with a sharp tip (probe) at its end that is used to scan the specimen surface. The cantilever is typically silicon or silicon nitride with a tip radius of curvature on the order of 10s of nanometers. When the tip is brought in proximity with sample surface, forces between the tip and the sample lead to a deflection of the cantilever according to Hooke's law [119]. The AFM can be operated in a number of modes, depending on the application. In general, possible imaging modes are divided into static (also called *contact*) modes and a variety of dynamic (non-contact or "tapping") modes where the cantilever is vibrated or oscillated at a given frequency[120].

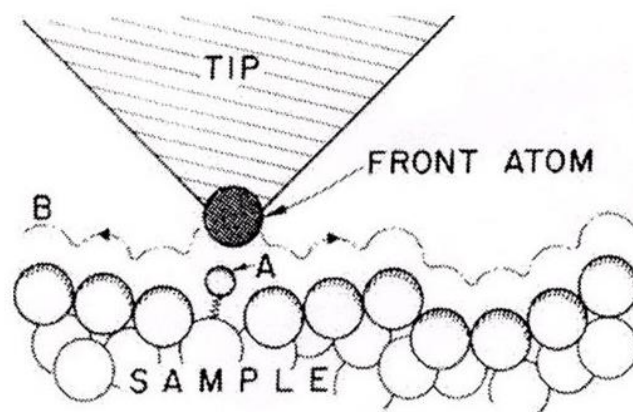


Figure 3.9 the basic working principle of AFM[120]

The working principle is that the tip follows contour B (see figure 3.9), in one case to keep the scanning tunneling current constant (STM) and in the other to maintain constant force between tip and sample (AFM, sample, and tip either insulating or conducting). The STM itself may probe forces when a periodic force on the adatom varies its position in the gap and modulates the tunneling current in the STM. The force can come from an ac voltage on the tip, or from an externally applied magnetic field for adatoms with a magnetic moment. AFM images are obtained by measurement of the force on a sharp tip (insulating or not) created by the proximity to the surface of the sample[120].

We measure our films using Bruker AFM (model: OTESPA-R3) and in the tapping (non-contact mode) for the roughness analysis. (Images are shown in chapter 4)

3.4 Electrical Characterization

3.4.1 Van Der Pauw technique

The specific resistivity and Hall effect are measured on a bar shaped sample as shown in the figure 3.10. Current contacts A and B and voltage contacts C, D, E and F are attached to the bar. The specific resistivity is derived from the potential drop between the point C and D or E and F and from the dimensions of the sample. The Hall voltage can be measured between the points C and E or D and F. The current contacts must be far away from the points C, D, E and F to make sure that the lines of flow are parallel and are not changed on application of magnetic field.

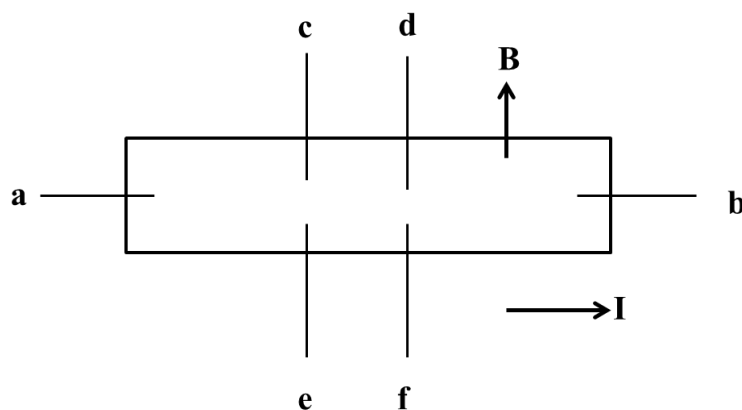
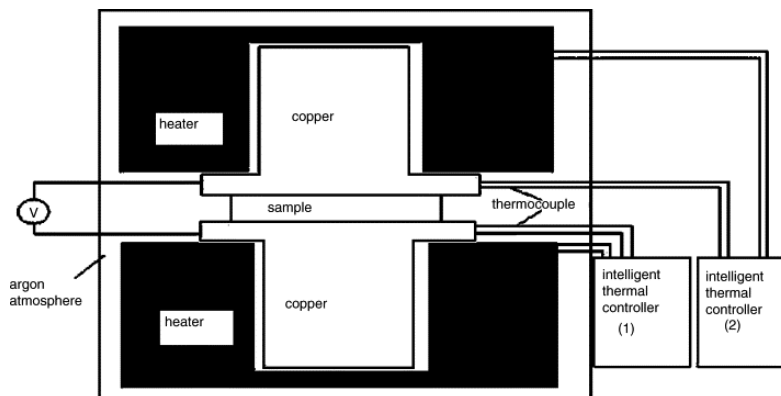


Figure 3.10 Schematic for hall measurement

A Keithley 4200 SCS van der Pauw sheet resistance measurement system was used to measure electrical conductivity of film samples. Films are most commonly measured using a 4-point collinear setup, however this method is extremely sensitive to sample size and probe placement. As the films in this project were on 5 x 5 mm substrates, the necessary geometric arrangement for accurately measuring electrical conductivity with the collinear technique was possible. To perform the measurements using 100nm thick gold contacts along with 5nm of Cr to give it better adhesion were deposited using the electron beam with the help of an optical mask. The van der Pauw method also uses 4 contact probes, however their arrangement is arbitrary. Instead, the sheet resistance is calculated by alternating an applied current to two probes at a time and measuring the voltage potential from the other two. The measurements performed in this thesis are typically accurate to 95% due to inhomogenities in the geometrical positions of contacts or the variations in the quality of the contacts.

3.4.2 Seebeck measurement



Figures 3.11 Schematics of the Seebeck measurement set up

The measurements were taken using an LSR from room to high temperature (300-800 K). A sample (5 by 10 mm) of cylindrical or prism shape is vertically positioned between two electrodes. The lower electrode block contains a heater, whilst the entire measuring arrangement is located in a furnace. The measuring arrangement inside the furnace heats the sample to a specified temperature. A set temperature gradient is created by the secondary heater in the lower electrode block at this temperature. Two thermocouples in contact with the sample then measure the temperature gradient between T1 and T2. A unique thermocouple contact mechanism permits high accuracy measurements of the electromotive

force dE at each of the two thermocouples as shown in figure 3.11. In addition the samples were heated at the rate of 10K/min and hold this temperature for 10 min to get the temperature gradient and corresponding Seebeck coefficient.

The dc four-terminal method is used to measure the electric resistance. By applying a constant current (I) at both ends of the sample and measuring the change in voltage dV between one wires at each of the two thermocouple pares. Possible sources of errors in this system can arise due to the poor contacts between the electrodes and the accuracy of measurement depends on the thermocouple and the electrical contacts on the sample.

In this work, we used this set up to measure the Seebeck coefficient and also the resistivity of the thin films and multilayers grown on various substrates and as a function of temperature. It is very important to see how these electrical properties behave as a function of different substrate and it affects the properties of thin films gown on them in terms of mobility, carrier concentration and conductivity. In the beginning we got very high Seebeck values but later on we discovered this system was not suitable for high resistivity thin film measurements.

3.5 Thermal conductivity

3 ω method for bulk and thin films

The idea of thermal conductivity technique was initially suggested by Corbino in 1912 with an aim to study the thermal behaviour of metal filaments used in incandescent light bulbs [121]. Then it was developed to measure frequency dependent heat capacity and measuring the thermal diffusivity of liquids [122]. The first application of 3ω method for measuring the thermal conductivity of solids was introduced by Cahill in 1987 [123]. Later on this method was applied to a wide range of materials by other researchers all around the world.

The thermal conductivity of solids is usually determined by measuring the temperature gradient produced by a steady flow of heat in a one-dimensional geometry. Below 50 K, where radiation of heat from the surface of the sample is small compared to the transport of heat through the solid, the steady-state technique is accurate and convenient. Problems arise, however, in extending the technique to room temperature and above, especially for materials that are poor conductors of heat; for example, amorphous solids. A large fraction of the heat that is intended to flow through the sample is radiated away; radial or pancake geometries for the heat flow and the use of heated shields that maintain the same temperature gradient as the

sample are proven ways of reducing the errors of black-body radiation. Unfortunately, these techniques often require large, precisely shaped samples and extreme care to be used successfully.

A recently developed ac thermal conductivity technique, the 3ω method, overcomes these difficulties [124]. The method is insensitive to errors from black-body radiation because the effective thickness of the sample is extremely small, on the order of 100 pm , when compared to standard geometries where 1 cm is more typical. Errors due to blackbody radiation can be shown to scale with a characteristic length of the experimental geometry by estimating the ratio of the heat radiated to the heat conducted through the sample. For example, if the temperature difference used to measure the thermal conductivity is held constant while all dimensions of the experimental geometry are reduced by a factor f , the power radiated through black-body radiation is reduced by f^2 while the heat conducted by the sample is reduced by only f . Therefore, in this example, errors from radiation have been reduced by the factor f . In comparing the 3ω method to standard techniques, the errors are reduced by the ratio of 1 cm to $100\text{ f}\mu\text{m}$, a factor of 100 [124].

For the purpose of measuring thermal conductivity of our grown thin film, we have employed our home-built 3ω setup. The 3ω technique has been extensively used to measure thermal conductivity of thin films as well as bulk materials. In comparison to other methods of measuring thermal conductivity, the 3ω technique, via its use of the frequency dependence of temperature oscillations, offers several major advantages including eliminating errors from black-body radiation, reducing thermalisation time, and the ability to measure both in-plane and cross-plane thermal conductivity values.

The principle operation of the technique is based on the use of a thin electrically conductive wire deposited on the specimen to be measured. Figure 3.12 shows a sample with contacts for the 3ω measurements made of gold deposited on the specimen with four pads for current and voltage connection. The wire acts as both the heater and a temperature sensor. As an ac current with an angular frequency of ω is supplied to the wire, the Joule heating causes the temperature of the wire to fluctuate at twice the current frequency. The generated heat diffuses into the specimen. Since the resistance is proportional to temperature, the wire resistance will also be modulated at 2ω . The voltage drop across the metal wire then oscillate at 3ω , which allows the extraction of the thermal conductivity.

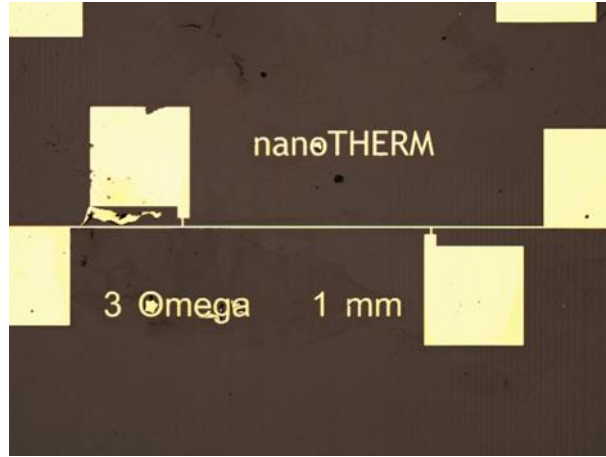


Figure 3.12 Optical image of contacts for measuring thermal conductivity with the 3ω method.

In the limit of thin and infinitely long wire, which is satisfied in most of the thin film cases studied in this thesis, the temperature rise caused by the joule heating on a substrate can be approximated by [124]

$$T = \frac{P}{\pi l k} \left(0.5 \ln \frac{D}{b^2} - 0.5 \ln(\omega) + \text{const} \right) \quad (2)$$

This shows that the thermal conductivity, K , can be obtained from the slope of the temperature rise plotted against the logarithmic of the frequency.

The experimental measurement of the thermal conductivity involves two steps: heating die to the thermal energy introduced in the system and sensing i.e., detection of the change of temperature or related physical properties due to the increase in thermal energy. Both heating and sensing can be measured, mainly, by electrical, optical and/or the combination of both methods.

For the case of thin film on substrate, the thermal conductivity can be obtained from the temperature drop across the film itself, i.e., from the difference between the experimental temperature rise of the heater and the calculated temperature rise of the substrate as is in slope method. Another method is to obtain the temperature of the substrate directly using differential technique, for example, by using the measured temperature rise on a bare substrate a reference.

We used MgO as the substrate to measure the thermal conductivity using 3ω to enable the comparison between the film and substrate as the thermal conductivity of the Nb-doped STO

thin films deposited on the substrates used in this thesis are comparable and does not follow the requirement of 3ω measurement of thin films i.e. We deposited the Nb-doped STO thin films in the similar conditions of the similar thicknesses as deposited on the other oxide substrates to make the comparison easily.

The analysis of the thin film measurements in this thesis by 3ω was done by the differential method which is the extension of the classical method followed for the thin films. In this approach the average temperature rise difference was measured with two sets of samples, i.e., the substrate and the substrate with as deposited thin film which was done to isolate the 3ω signal drop caused by thin film.

The common background contribution of the parasitic interfacial thermal resistances can be subtracted by removing the signal of the reference sample from that of the thin film such as the one between the heater and the underlying film and the one between the substrate and the first deposited layer. Subtraction of the additional elements, such as buffer or nucleation layers, can also be performed from the total experiment temperature rise, which is obtained at comparable power inputs by similar heaters deposited on the thin film and the reference substrate. Under this condition, the effective thermal conductivity of the film [125]

$$K_{eff} = \frac{L}{2} \left[\left(\frac{2V_{3\omega}b}{P_l\alpha V_{1\omega}} \right)_{R+F} - \left(\frac{2V_{3\omega}b}{P_l\alpha V_{1\omega}} \right)_R \right]_{avg}^{-1} \quad 3.4$$

The subscripts R + F and R correspond to the specimen with the studied film and the reference, respectively. Although the differential 3ω method requires two sets of measurements, a detailed study performed showed that it is advantageous compared to the slope-method because it can reduce the uncertainty in the measurement of the thermal conductivity of the thin films and multilayers [125]. The value of k_{eff} obtained from Eq.3.4 is not affected by the substrate thermal conductivity, and the contributions from any additional layers are almost eliminated by the measurement on the reference sample. Because of the mentioned advantages, the differential method was used to perform the thermal conductivity measurements in this work.

3.6 Graphene transfer on oxide substrates

Growth and transfer of graphene films

CVD prepared graphene on Cu foil are used for this method and the fabrication procedure can either be with the evaporation of a Ni film on a SiO₂/Si substrate[126] or by growing graphene films on 25- μ m thick Cu foils in a hot wall furnace consisting of a 22-mm ID fused silica tube heated in a split tube furnace; several runs were also done with 12.5- and 50- μ m thick Cu foils. A typical growth process flow is:

- (1) Load the fused silica tube with the Cu foil, evacuate, back fill with hydrogen, heat to 1000°C and maintain a H₂(g) pressure of 40 mTorr under a 2 sccm flo.
- (2) Stabilize the Cu film at the desired temperatures, up to 1000°C, and introduce 35 sccm of CH₄(g) for a desired period of time at a total pressure of 500 mTorr.
- (3) After exposure to CH₄, the furnace was cooled to room temperature.

The experimental parameters temperature profile, gas composition/flow rates, and system pressure can be found in [127]. The cooling rate was varied from > 300°C/min to about 40°C/min which resulted in films with no discernible differences.

Graphene films were removed from the Cu foils by etching in an aqueous solution of iron nitrate. The etching time was found to be a function of the etchant concentration, the area, and thickness of the Cu foils. Typically, a 1 cm² by 25- μ m thick Cu foil can be dissolved by a 0.05 g/ml iron nitrate solution in few minutes. Since graphene grows on both sides of the Cu foil, two films are exfoliated during the etching process. We used two methods to transfer the graphene from the Cu foils: (1) after the copper film is dissolved, a substrate is brought into contact with the graphene film and it is ‘pulled’ from the solution; (2) the surface of the graphene-on-Cu is coated with polydimethylsiloxane (PDMS) or poly-methyl methacrylate (PMMA) and after the Cu is dissolved the PDMS graphene is lifted from the solution. The first method is simple, but the graphene films break and tear more readily. In this work we use the second method as the graphene films are easily transferred to our desired substrates such as LAO or LSAT, with significantly fewer holes or cracks maintaining the quality of single or few layer graphene(< 5% of the film area)[127].

Using the above method we performed etching of Cu with graphene and after the copper is removed we put the graphene layer in per chloric acid for 10 minutes and then wash four times with water to transfer the pure clean layer of graphene on the oxide substrates (LaAlO₃

and LSAT). After transferring graphene layer on the oxide substrate we leave it overnight for it to settle down completely and it is ready to use the next day (as shown in figure 3.12).

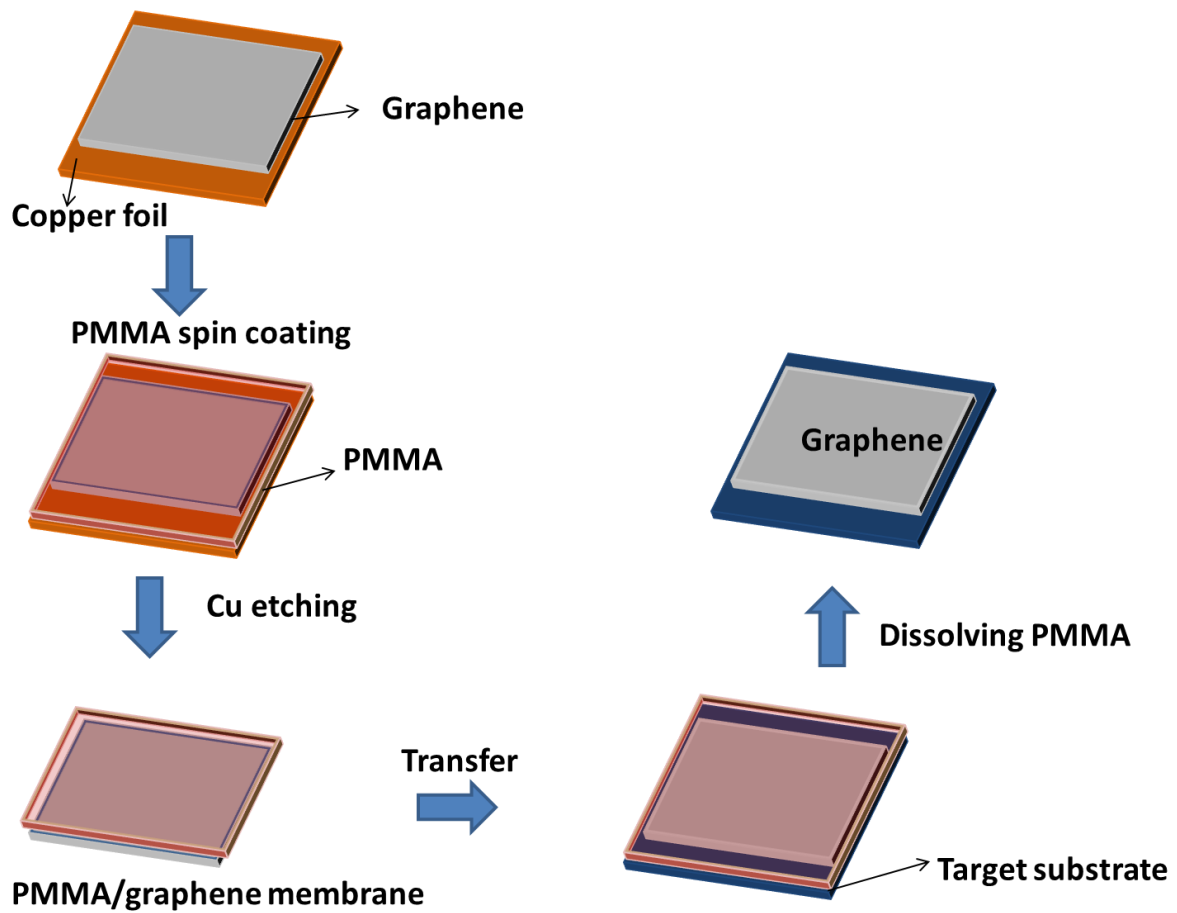


Figure 3.13 Schematic of the wet transfer of graphene on a substrate by etching away the copper.

Chapter 4

Thermoelectric properties of Nb-doped SrTiO₃ thin films

One strategy to obtain efficient thermoelectric materials is to engineer their properties to ensure a high power factor and low thermal conductivity [21, 128]. In this respect Strontium titanate (SrTiO₃), known simply as STO, is becoming a material of choice among oxide thermoelectrics as carrier concentration and Seebeck coefficients became increasingly promising [129] as mentioned in section 1.7. For this thesis STO was selected to investigate the dependence of thermoelectric properties on several parameters. The focus is initially on thin films but later in this work, studies of STO-based superlattices and heterostructures will also be reported. This chapter deals with the impact on thermoelectric properties of several parameter, namely, doping level, film thickness, substrate type and whether the layers are just thin films or multilayers of STO doped with Nb.

To get a high performance n-type thermoelectric film or multilayer structure, we started first by varying the niobium doping concentration to decide which doping concentration is optimum for getting the best TE properties. That doping concentration was then taken forward with varying the thicknesses so that the optimum thickness could be decided and by taking the optimum thickness and doping concentration a decision on the most appropriate substrate surface was made for the epitaxial growth of Nb doped STO film and superlattices.

4.1 Nb-doping of SrTiO₃ thin films

As explained in Chapter 3, the samples for this work have been grown by PLD. However, an important step is the preparation of the targets for PLD epitaxial growth, which will be described in the section below.

4.1.1 Target Preparation

STO targets doped with 2, 5 and 15 mol% Nb were prepared by a conventional solid-state reaction method. SrCO₃, TiO₂ and Nb₂O₅ powders were mixed in suitable stoichiometric ratios and annealed at 1050° C for 48 hours in a high temperature oven during which oxygen vacancies are generated so that they can contribute excess electrons to enhance the electrical conductivity of the PLD n-type SrTiO₃. The annealed powders were checked with XRD and then they were ball milled again, pressed into disks at ~150 MPa and sintered at 1400°C for

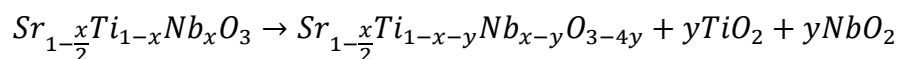
48 hours in a high temperature oven, to increase the pellet density and remove any additional oxygen vacancies. The main purpose of the annealing process is to guaranty that the Nb⁵⁺ ion is incorporated in Ti⁴⁺ sites rather than formation of oxygen vacancies. In these Nb doped STO material, it is also known that other than producing oxygen vacancies there could also be the existence of cation vacancies (mostly in Sr sites) that might be not useful for the compensation of the excess charge generated upon Nb substitution rather than generating excess delocalized electronic charges.

These targets were then used in the PLD reactor to deposit thin films of various thicknesses at high temperature (1200k) and low pressure (10⁻²-10⁻³ mtorr) at 1 pulse/s rate with systematic toggling and rotation at the rate of 15 rpm as mentioned in chapter 3. These conditions were found to be important to ensure the epitaxial growth of the films in a particular crystallographic axis.

All targets and films were characterized by scanning electron microscopy (SEM) and X-ray diffraction (XRD). Fig. 4.1a shows XRD patterns of the solid targets and the resulting thin films with 2, 5 and 15 mol% Nb-doped STO.

4.1.2 Structural Properties

The Nb-STO thin film samples in this study exhibit high quality with a single phase cubic perovskite structure, comparable to pure STO [129]. The slightly broadened diffraction peaks implies that the particle sizes are significantly small as shown in figure 4.1a and the broadening in figure 4.1c. It is also noted from XRD data that the unit-cell volumes estimated increase with increasing doping level. Such an increase in the cell volume is related to the replacement of small-sized Ti⁴⁺ ions (60.5 pm) in the B site of the perovskite structure by the larger Nb⁵⁺ ions (64.0 pm). In the XRD patterns of as-sintered samples shown in Fig. 1a, some unexpected weak peaks are found around 2θ = 28 degrees, implying the presence of a second rutile phase (TiO₂ or Nb-doped TiO₂). A second phase formation at higher Nb doping concentration at high temperature and high vacuum may take place as [130] following:



Where $y < x \leq 0.15$ and substitution of Nb (n-type) atoms replacing Ti atoms in stoichiometric SrTiO₃ leads to the creation of conduction electrons in a reducing environment

and at high temperatures. This electronic compensation mechanism can be expressed using Kröger-Vink notation as [131]

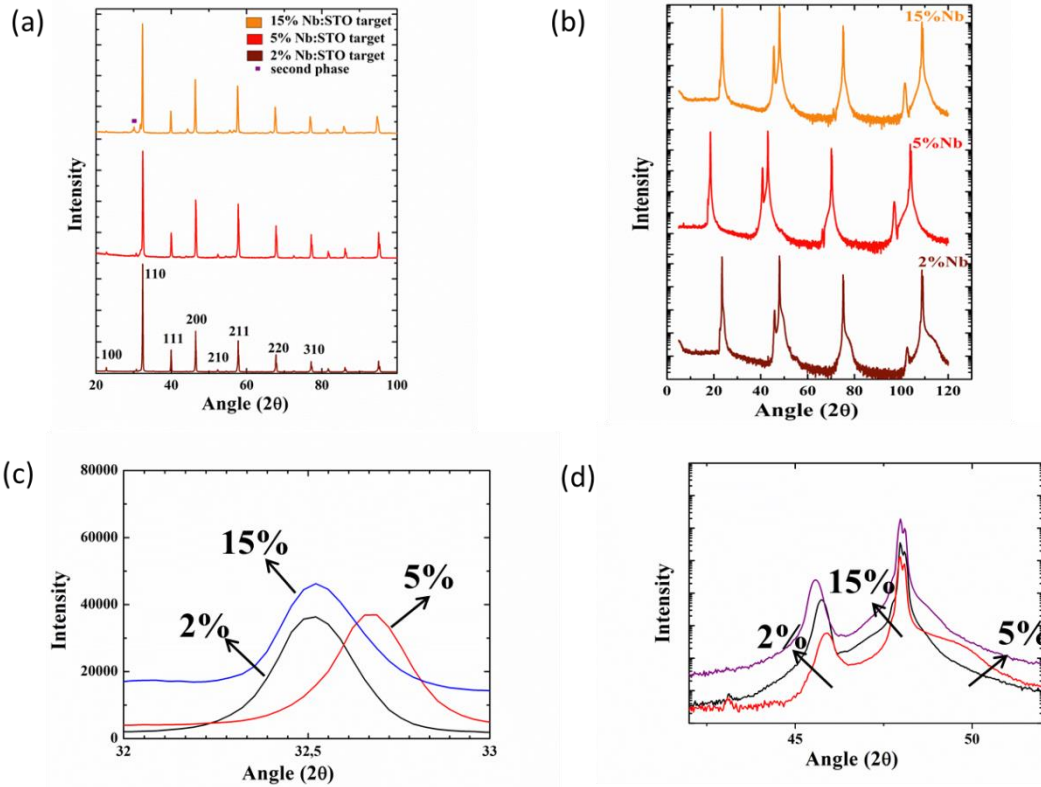
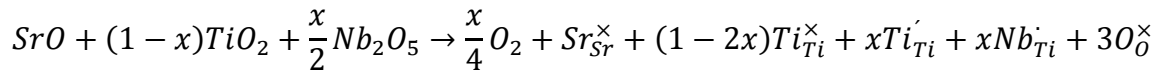


Figure 4.1 XRD crystallographic planes of (a) targets with different doping concentration and (b) the resulting doped PLD Nb:STO films (c) (200) diffraction peak with different dopant concentration (d) (002) peak of the Nb doped STO film with different doping concentration on LAO substrate.

This donor compensation mechanism also supports the increase of the unit-cell volume upon replacement of Ti^{4+} ions by Nb^{5+} ions. The increased cell volume corresponds to the sharp diffraction peak observed in XRD results for as-sintered samples (Fig. 4.1a). Figure 4.1b exhibits the XRD diffraction from the films grown by PLD using different Nb doped STO targets under optimised conditions showing the direction of growth to be 001 and all the planes of the Nb doped $SrTiO_3$ thin films. There is a shift in the diffraction peaks in the films from the different targets as seen in figure 4.1c which shows the slight shift in the 002 peak of the film from the three different dopant concentration films.

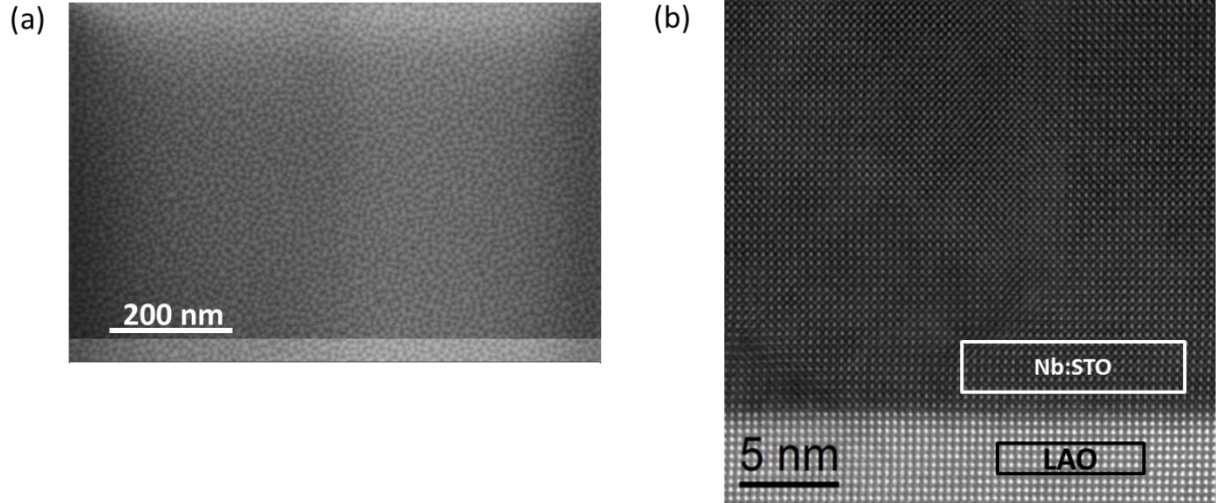


Figure 4.2. Electron microscopy images. (a) SEM image of a film on LaAlO_3 substrate and (b) HR TEM of the epitaxial growth of Nb doped SrTiO_3 thin film on the LaAlO_3 substrate.

Figure 4.2a and 4.2b, display a SEM and a high-resolution TEM (HRTEM) image of a 2 mol% Nb-doped SrTiO_3 thin film. The SEM images show the homogeneity of the grown film on the substrate. The STEM image confirms the epitaxial growth of the Nb-doped STO on a LAO substrate (Fig. 4.2b) in the 001 direction. Due to the step by step growth method followed, electron microscopy shows sharp interfaces and homogeneous films, which may lead to a reduction of interface scattering of electrons, enhance carrier mobility, and hence increase the electrical conductivity, as will be discussed later [132, 133].

4.1.3 Thermopower measurements

The Seebeck coefficient of the samples was measured from 300 to 800 K in a helium atmosphere. The highest values of the Seebeck coefficient were found in films doped with 2 mol% Nb grown on LAO.

The temperature dependence of Seebeck coefficient of a 66 nm thick Nb-doped STO films with different doping concentration are shown in Fig. 4.3a. The variation of Seebeck coefficient as a function of temperature can be explained by Cutler-Mott formula [134]:

$$S = \frac{\pi^2 K_B^2 T}{3e} \left. \frac{\partial(\ln \sigma)}{\partial \epsilon} \right|_{\epsilon_F} = \frac{\pi^2 K_B^2 T}{3e} \left| \frac{\partial(\ln n)}{\partial \epsilon} + \frac{\partial(\ln \mu)}{\partial \epsilon} \right|_{\epsilon=\epsilon_F} \quad 4.1$$

Where K_B is the Boltzmann constant, e the electronic charge, $\sigma(\epsilon) = en(\epsilon)\mu(\epsilon)K_B T$ and $\mu(\epsilon)$ are the spectral conductivity and mobility. The temperature dependence of these films can be

understood with Seebeck dependence on the mobility, carrier concentration and also the electrical conductivity.

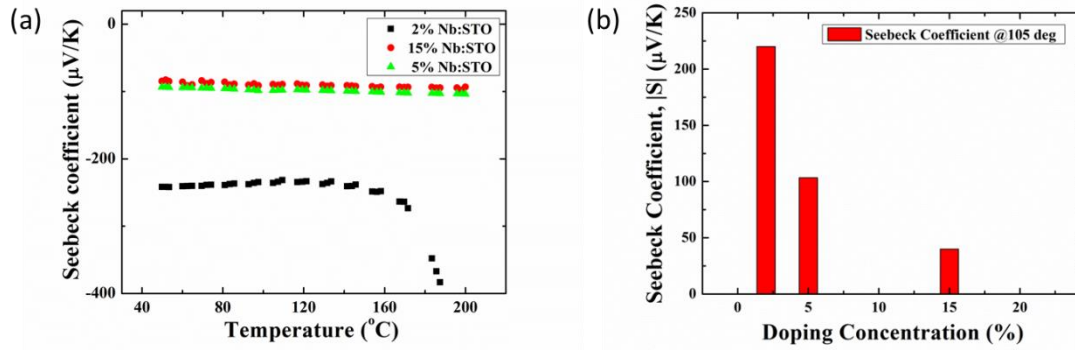


Figure 4.3. Seebeck coefficient of 2 mol% Nb-doped STO on LAO. (a) Temperature dependence of the Seebeck coefficient of the 66 nm thick film. (b) Seebeck coefficient dependence on doping concentration for thin films of 50 nm thickness at 105° C.

The Seebeck coefficient decreases with increasing doping level (see Fig. 4.3b), which is in good agreement with the result of Ohta et al [72], although in that reference the Nb doping level range was from 10 to 40 mol%. In this study, samples with a doping level of 2, 5 and 15 mol% show larger Seebeck coefficients compared to the reported bulk STO ($S_{\text{bulk}} = -61 \mu\text{V/K}$) and also we tried a series of thicknesses of thin films with the undoped STO and they were all insulating. The decrease of S with increasing doping level can be understood considering that the carrier concentration plays a dominant role in S rather than the contribution from a slightly enhanced m^* . Also, assuming that the electrical conductivity does not degrade, the selected doping for the remaining of this work is chosen to be 2 mol%, which promises the highest power factor ($S^2\sigma$) and low thermal conductivity.

4.2 Thickness studies of Nb-doped SrTiO₃ thin films

The lattice mismatch between STO and the different crystals chosen as the substrates impacts the strain in the PLD-grown films. To optimise the film thickness samples were grown on (100)-oriented LaAlO₃ (LAO) single crystal substrates (Crystec GmbH, size 10×5×5mm³) at 1200K and 10⁻²-10³ mtorr, without introducing background gas. Targets prepared as described in section 4.1 were used with 2% Nb. Films were grown with thicknesses 30, 66, 99, 150, 165 and 200 nm, with an uncertainty of ±2 nm.

4.2.1 Thickness measurements

The film thickness was measured by X-ray reflectivity (XRR), up to 100 nm. Thicker samples were measured by Ellipsometry with a rotating analyser over angles of incidence from 55 to 75° in steps of 5° from 1.22 to 5.53 eV. The in-plane and out-of-plane lattice parameters were obtained from reciprocal space maps of the (-103) reflection obtained from XRD.

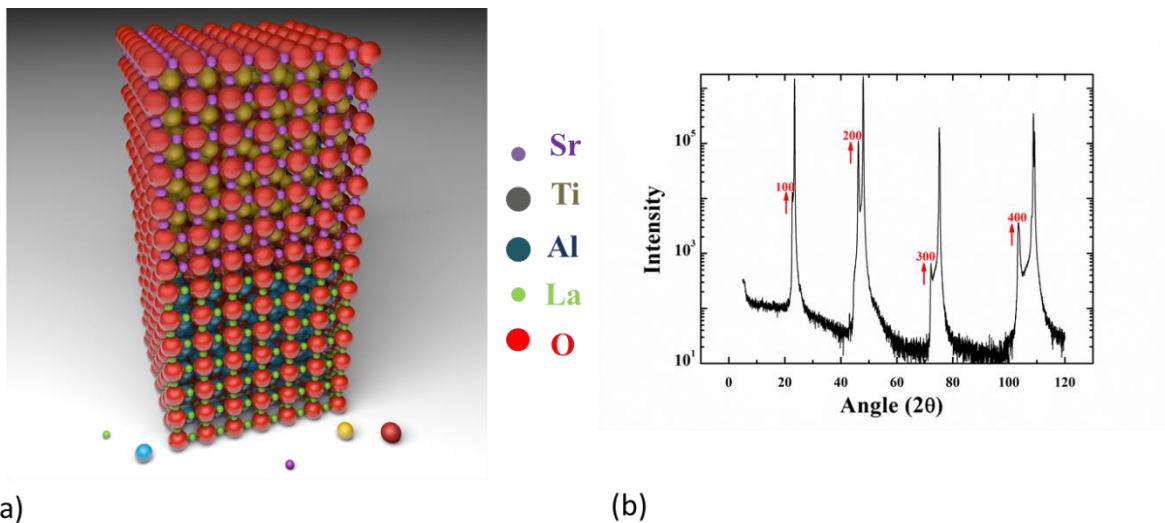


Figure 4.4 (a) schematic of atomic arrangement of STO grown on LaAlO₃ (Sr, Ti, Al, La, O) (b) X-Ray diffraction pattern of a Nb-SrTiO₃ film deposited on LAO showing the film reflections marked by red arrow. The most intense peaks correspond to substrate reflections.

Figure 4.4a shows a schematic of the 2D atomic arrangement of a SrTiO₃ film on a LaAlO₃ substrate. The green and blue spheres are La and Al, while purple, golden and red ones represent Sr and Ti and the oxygen atoms respectively. SrTiO₃ is cubic in nature but when doped with niobium the lattice is slightly expands due to the atomic size of niobium Nb⁵⁺ (64 pm) substituting Ti⁴⁺ (60.5 pm) atoms in the octahedrally coordinated B-sites and also due to the rotation of the TiO₆ octahedra [135]. This rotation can cause the perfectly cubic structure to either expand in all the three directions giving it a rhombohedral orientation or either two directions resulting in the tetragonal structure. The crystallographic XRD (2θ-ω) data in Figure 4.4b shows sharp diffraction peaks of the thin film and the LaAlO₃ substrate confirming the epitaxial growth in (001) direction which can also be confirmed by HRTEM cross-section image analysis in Figure 4.5(b).

4.2.2 XRD and HRTEM analysis

The structural analysis of the thin films is shown in Figures 4.4, 4.5 and 4.6 consisting of XRD data showing the crystallographic planes and the XPS analysis of the thin film of Nb:SrTiO₃ on LaAlO₃ substrate. Figure 4.5a shows the variation of the in-plane and the out-of-plane lattice parameters and as we can see toward the thicker film it comes near to the bulk value (3.92Å) but when we towards lower thickness the large out of plane parameter arises due to the tetragonal strain in the structure which can arise from various factors such as the rearrangement of atoms in the STO structure, epitaxial strain or could be due to some vacancy formation. The HRTEM images in figure 4.5 b,c and d shows the evidence of the epitaxial growth and also the variation of the grain boundaries with comparison to the thickness.

4.2.3 XPS analysis

After the XRD and HRTEM measurements we performed the XPS analysis to know the atomic composition of the thin films and which orbitals take part in formation of the thin film and also to know if there were some oxygen vacancies or not. The XPS was done at a base pressure of 1×10^{-10} mbar using monochromatic Al K_α radiation (1486.74 eV) as excitation source.

XPS data in Figure 4.6a shows the binding energies of the Sr 3d-doublet lines at 133.7 and 135.5 eV, which are attributed to Sr 3d_{5/2} and Sr 3d_{3/2}, respectively. In the case of strontium these values are attributed to Sr atom [136]. The binding energies of the Ti 2p_{3/2} and Ti 2p_{1/2} of Nb-SrTiO₃ samples are 459 and 464.8 eV, and of Nb 3d_{5/2} 206.5 eV as shown in (Figure 4.6b and 4.6c).

These values are close to the reported values for α-Ti atoms in the perovskite structure of SrTiO₃ and correspond to Ti with oxidation state of 4⁺ and to no oxidation state of 3⁺ [137, 138]. The absence of peaks around 456 and 462 eV [5], marked in grey, suggests that oxidation states of Ti³⁺ are not present in the films, indicating a non-detectable presence of oxygen vacancies. Finally, the high binding energy shoulder of the O(1s) peak near 532 eV is observed for this surface (Figure 4.6d), consistent with the O(1s) spectra of epitaxial SrTiO₃ films hydroxylated due to air exposure [138, 139].

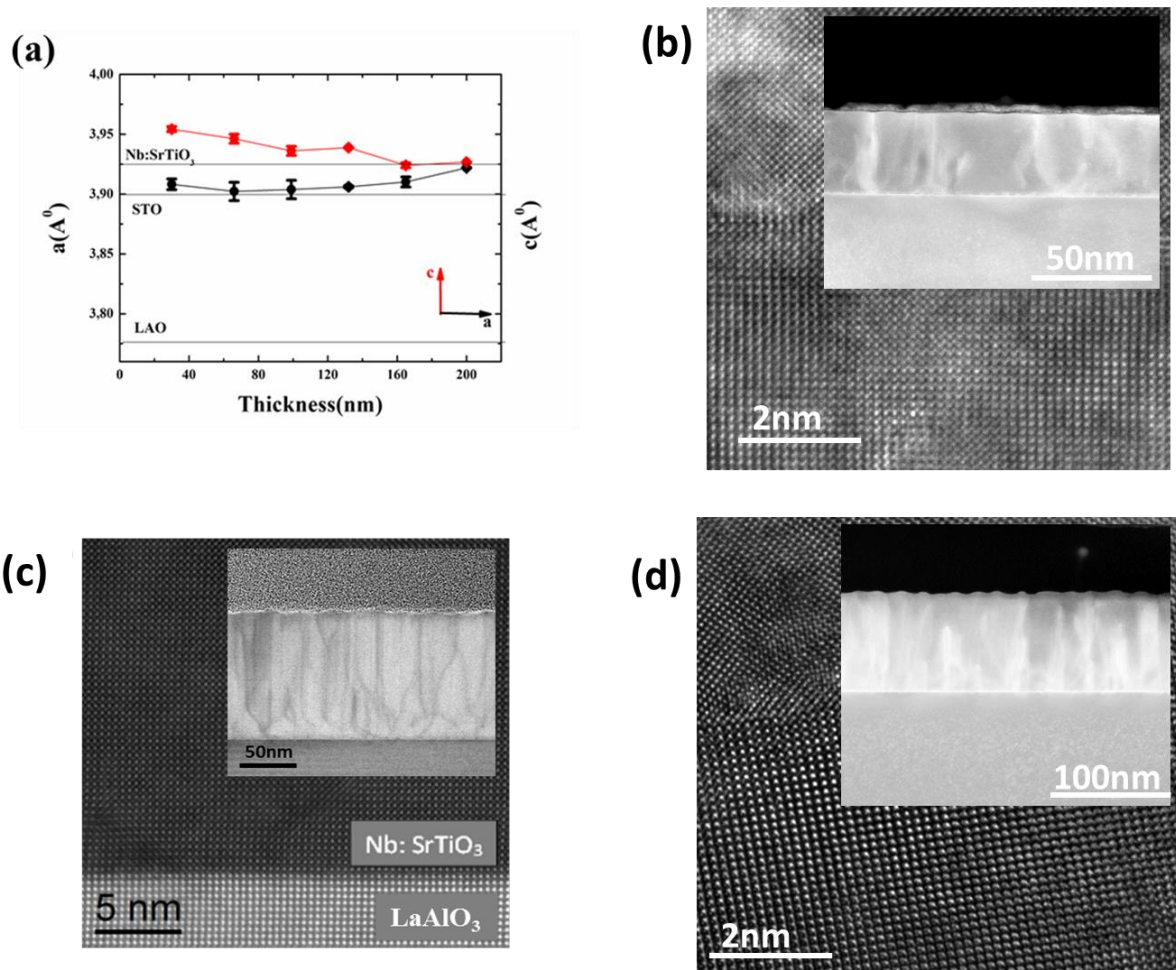


Figure 4.5 (a) In-plane (a) and out-of-plane (c) lattice parameters calculated from reciprocal space maps. (b, c and d) HRTEM cross-section image of the interface region showing the substrate and the epitaxial growth of the 30, 66 and 200 nm thick thin film of Nb-doped SrTiO₃ on LaAlO₃ substrate and inset is the BF-STEM image showing the variation of the grain boundaries in the 30, 66 and 200 nm thick films.

4.2.4 Electrical measurements

Hall measurements were made in $5 \times 5 \text{ mm}^2$ square-shaped samples in the van der Pauw geometry with ohmic contacts of Cr/Au (5 nm/200 nm) deposited by electron beam evaporation. The Seebeck coefficient was measured in samples of $10 \times 5 \text{ mm}^2$ ensuring that for each temperature gradient sufficient time elapsed to stabilize the temperature and voltage differences. The thermal conductivity was measured using a home-made 3-omega set up [124].

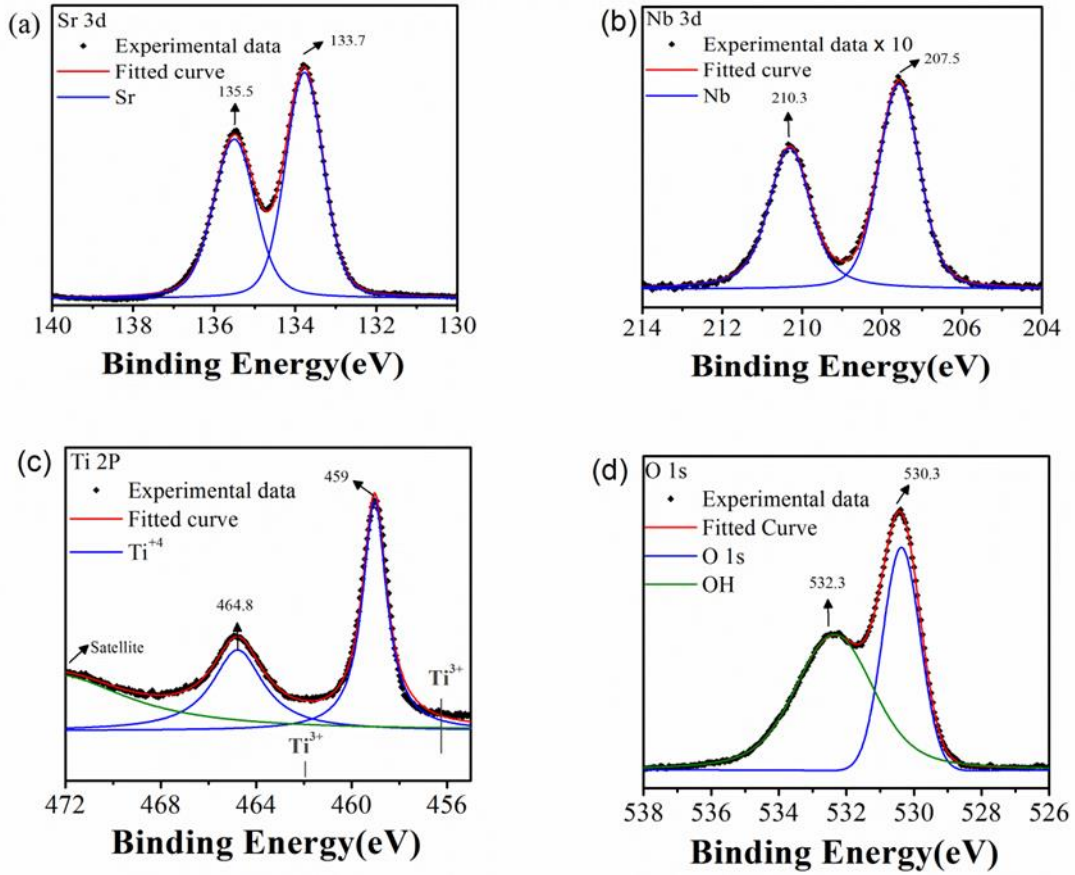


Figure 4.6. XPS spectra of the different elements in a thin film of Nb:STO.

Figure 4.7 (a and b) shows the room temperature carrier concentration and the Seebeck coefficient of the thin films as a function of thickness while Figure 4.7 (c and d) shows the Seebeck coefficient and power factor as a function of temperature. The high value of Seebeck coefficients can be partly explained due to the d-band nature of the electronic shells of STO, as this material belongs to the 3d transition metals series. The associated electron effective mass is relatively large ($m^* = 4.5 - 10 m_0$) in STO, resulting in a high bulk Seebeck coefficient which is directly proportional to m^* for bulk materials [140].

$$S = \frac{8m^*\pi^2k_B^2}{3eh^2} T \left(\frac{\pi}{3n} \right)^{2/3} \quad (4.1)$$

where k_B is the Boltzmann constant, e is the electronic charge, and n is the electron concentration of a doped semiconductor. The temperature and doping concentration dependence of S observed in our samples are in good agreement with other doped STO

materials for e.g. 40%Nb doped film the reported Seebeck is $-160\mu\text{V/K}$ and for 20% Nb doped and undoped superlattice structures $-320\mu\text{V/K}$ [71, 72, 141, 142].

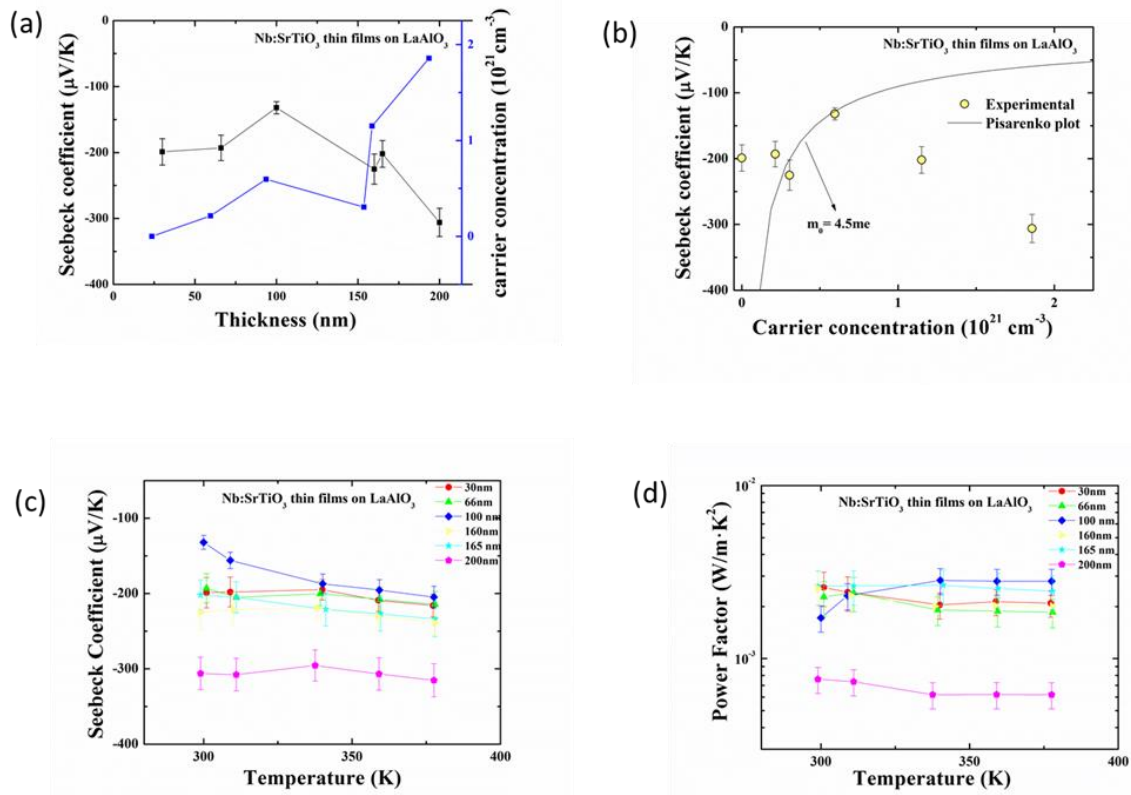


Figure 4.7 Thermoelectric properties of Nb: SrTiO₃ films. (a) Charge carrier concentration and Seebeck coefficient at room temperature as a function of thickness. (b) Seebeck coefficient as a function of charge carrier concentration compared to the Pisarenko plot. The solid curve is based on the single parabolic band model described by eq. 4.1 with $m^* = 4.5 m_e$ at 300 K. (c) Seebeck coefficient as a function of temperature (d) power factor as a function of temperature using the values from table 4.1.

As can be seen from Eqn. 4.1, an increase in carrier concentration will lead to a decrease of the Seebeck coefficient, whereas a heavier effective mass, m^* , will enhance it. The m^* appears to increase with increasing doping level, which could be mainly due to an increase in the lattice parameter, or an increase in the distance between two neighbouring Ti ions in the unit cell, as found experimentally and theoretically in doped STO [72, 143].

In these thin films, and in 2D superlattices structures, the enhanced Seebeck coefficient can be explained in terms of the changes in the Fermi energy, as well as in the electronic density of states (DOS), as seen in the next two equations derived from the equation 4.1:

$$S = -\frac{K_B}{e} \left(\frac{2F_1}{F_0} - \chi_{2D}^* \right) \quad (4.2a)$$

$$\chi_{2D}^* = \frac{1}{k_B T} \left(E_F - \frac{\pi^2 K_B^2 T^2}{12 E_F} - \frac{\hbar^2 \pi^2}{2 m_z^* W^2} \right) \quad (4.2b)$$

where E_F is the Fermi energy, m_z^* is the z-component of the effective mass (along c-axis), W is the quantum well width related to the lateral dimension where electrons are confined, F_1 is the Fermi Dirac integral of order 1 and χ_{2D}^* is the reduced chemical potential in 2-dimensional structures. The dependence of the Seebeck coefficient of Nb-SrTiO₃ films on the effective mass can be better understood by considering the direct correlation of m^* with lattice constant. The effective mass taken into account is the one in the direction of confinement for the 2D structure, $m^* = m_z^*$, and from our data the linear fit of the Seebeck coefficient against temperature yields a value smaller than the bulk one as shown in figure 4.7b [144]. The enhanced power factor, i.e., Seebeck coefficient and electrical conductivity, can be explained taking into account the theoretical approach in which, for a given lattice thermal conductivity, K_l , the ideal transport-distribution function that maximizes ZT is a bounded delta function, approximately realized as a sharp function with a large slope in the density of states (DOS) at the Fermi level E_F (see figure 4.8) [8].

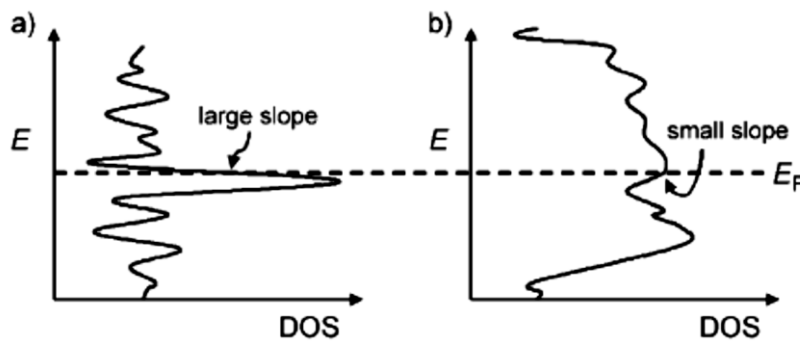


Figure 4.8 Illustrates the ideal density of states for a high and low value of S depending on the slope at the fermi level[8].

A better understanding requires the knowledge of the electronic level at the interface, calculations which were beyond the scope of this thesis.

All the measured data as a function of different thicknesses taken into consideration for the calculation of the overall ZT of Nb doped thin films on LAO substrate.

Thickness (nm)	Carrier concentration $n(\text{cm}^{-3})$	Mobility (cm^2/Vs)	Seebeck coefficient ($\mu\text{V}/\text{K}$)	Power factor (mW/mK^2)	Thermal conductivity (W/mK)	ZT at 300 K
30	-3.17×10^{16}	2.26	199 ± 19	2.25	2.4 ± 0.01	0.28 ± 0.02
66	-2.14×10^{20}	0.68	193 ± 9	2.27	2.4 ± 0.01	0.28 ± 0.03
99	-5.96×10^{20}	0.55	132 ± 9	2.82	2.4 ± 0.01	0.35 ± 0.02
160	-3.73×10^{21}	0.29	225 ± 20	2.54	3.8 ± 0.015	0.20 ± 0.03
165	-7.01×10^{20}	0.29	202 ± 20	2.63	3.8 ± 0.015	0.21 ± 0.03
200	-1.98×10^{20}	0.28	306 ± 20	0.75	3.9 ± 0.01	0.05 ± 0.01

Table 4.1 Thermoelectric properties of 2% Nb-doped STO films on LAO as a function of thickness at room temperature.

4.3 Results and discussion

In the literature, the Seebeck Coefficient in such low dimensional films is said to increase by electron filtering, i.e., high energy electrons can pass through the barrier while others are scattered, thus decoupling the S from n [83, 145-147]. However, in our work one explanation for the enhancement of Seebeck coefficient is the confinement of the charge carriers. We estimate the Fermi energy to be low as explained elsewhere [148] assuming that only one confined sub-band is occupied and that it lies inside the conduction band.

The relationship between the bulk Seebeck coefficient and the charge carrier concentration can be expressed empirically as [149]:

$$S(\mu\text{V}/\text{K}) = 1180 - 254 \log \frac{(n_{3D})}{10^{17} \text{cm}^{-3}} \quad (4.3)$$

In degenerate semiconductors like doped SrTiO₃, a carrier concentration-dependent correction introduced by Fermi–Dirac statistics is necessary [9, 70, 144]. The conductive state in 2% Nb doped thin film is barely metallic with a low Fermi energy and is similar to the situation of the n-type degenerate semiconductor, then the low Fermi energy in these compounds is expected to give rise to a large Seebeck coefficient due to a large entropy term arising from the six-fold degeneracy of the Ti 3d-t_{2g} conduction bands, since in these thin films the bottom of the conduction band is predominantly formed by Ti 3d orbitals [150]. The carrier concentration (10^{18} - 10^{21} cm⁻³) in the films studied here closely corresponds to the Nb concentration, indicating that probably most Nb donors are ionized. Such high carrier concentration can be explained by the filling up of the Ti 3d orbitals in the monolayer deposited near to the surface of the LAO and STO interface. In our thin film samples, the Seebeck coefficient and its dependence on carrier concentration (10^{18} - 10^{21} cm⁻³) are comparable to the SrTiO₃:Nb single crystals, which attest to the high quality of the PLD grown films. Figure 4.4 (a) shows the Seebeck coefficient and carrier concentration dependence on Nb:STO film thickness and Figure 4.7 (b) shows the dependence of Seebeck coefficient on carrier concentration. The Seebeck coefficient is shown as a function of carrier concentration, clearly deviating from the Pisarenko plot. The Pisarenko plot describes the variation of the Seebeck coefficient with an isotropic effective mass [151]. The deviation from it point to a strong anisotropy, as expected. Instead, the Seebeck coefficient resembles that of a 2DEG, as demonstrated in [152]. The effective mass can be estimated from the temperature dependence of the Seebeck coefficient (Figure 4.7 c). Furthermore, this plot also suggests electron degeneracy as it shows a linear increase of the Seebeck coefficient with temperature.

Power factors in the range of 2.5×10^{-2} to 2.2×10^{-3} W/mK² were obtained using the measured Seebeck coefficient and electrical conductivity. These values are higher than those reported in the literature for Nb-substituted bulk titanates between 0.1 and 1×10^{-3} W/mK²) [153].

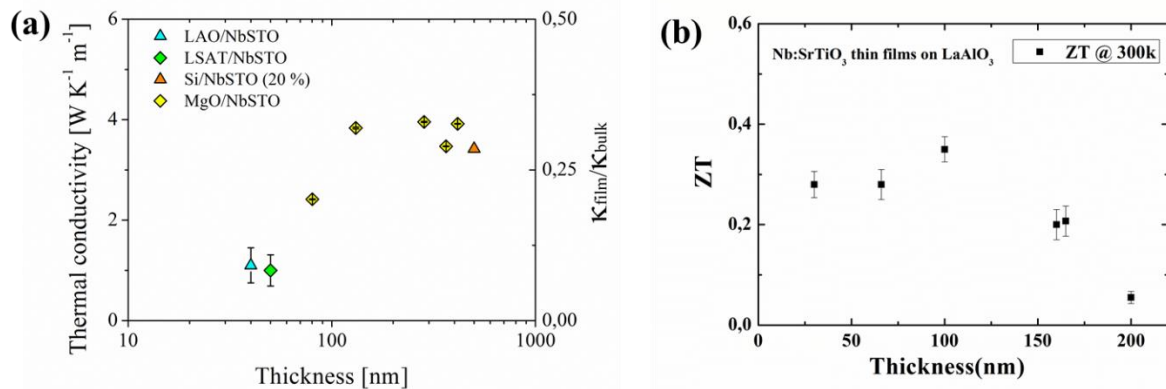


Figure 4.9 (a) Thermal conductivity of Nb:STO using the 1-dimensional model as a function of thickness on various substrates. (b) Thermoelectric figure of merit as a function of thickness for Nb:STO on LAO at room temperature.

A 8-fold decrease in thermal conductivity with respect to bulk STO (12 W/mK) was measured by the 3ω method at room temperature. This decrease is attributed to structural defects in the form of long grains in the thin films (seen in Figure 4.5 for three different thicknesses). We measure 3.8 W/mK for the 200 nm thick film and 2.4 W/mK for the 66 nm thick film. From the study of the dependence of the thermal properties on film thickness the preliminary conclusion is the need for a better understanding of the interface between the thin film and the substrate as in these thin film systems the thermal conductivity reduction take place mainly due to the scattering mechanisms which can be either interface scattering which can induce the thermal resistance at the substrate surface closer to the interface, boundary scattering or the phonon electron scattering which helps in reducing the phonon lifetimes and hence the thermal conductivity. Here we have shown the data through the HRTEM imaging that there are some grain boundary formations in the film during the growth process despite the epitaxial nature of the film, which in turn is responsible for the lowering of the thermal conductivity.

To enable a comparison to thermal conductivity calculations of thin films using the 1-dimensional model, MgO was chosen as a suitable substrate [154]. The reason being that as the 3-omega technique has its own limitations and the thermal conductivity between the substrate and thin film to be measured should have a difference of at least of a factor of 10. MgO is very well suited for that and enables the frequency relation of the 3-omega method to be applied and the thermal conductivity determination of the thin films studied in this work.

Several types of deviations from crystallinity may influence the thermal conductivity, such as point defects, dislocations, and grain boundaries. As we do not detect oxygen vacancies in Nb-SrTiO₃ thin films, we deduce that grain boundaries, shown in the HRTEM images in Figs. 4.5a, b and c, play the major role and could be the main source of phonon scattering hence decreasing the thermal conductivity [155].

Using the measured data obtained in this work, a ZT value of 0.35 (as shown in table 4.1) is calculated for a 100 nm thin film at room temperature, which is beyond the reported value of the state of the art.

4.4 Thermoelectric properties as a function of different substrates

4.4.1 Introduction

STO has been studied for various applications using (LaAlO₃)_{0.3}-(Sr₂AlTaO₆)_{0.7} (LSAT) (001) substrates, and room-temperature ferroelectricity has been demonstrated when STO is grown with in-plane tensile strain on DyScO₃ [156]. Several substrates investigated in this work, for the deposition of 2% Nb:STO and were LaAlO₃ (LAO), (LaAlO₃)_{0.3}-(Sr₂AlTaO₆)(LSAT), SrLaAlO₄ (SLAO), DyScO₃ (DSO) and SiO₂ respectively. STO is also usually grown on LAO as thin films and superlattices for thermoelectric properties [11, 149, 157]. Despite being structurally compatible with STO, LSAT and other substrates are not well studied. In fact, surprisingly little is known about the thermoelectric properties of STO thin films on LSAT, SLAO and DSO substrates and its interface, despite their potentially important role in affecting the overall electronic structure of system.

The study of PLD-grown epitaxial STO thin films and their enhanced thermoelectric properties is the core of this section.

4.4.2 Growth and thermoelectric studies

The substrates were selected for the growth of Nb doped STO thin films depending most importantly on their lattice parameters. The low lattice mismatch with STO with interesting electrical, thermal or superconducting properties and strain management has favoured single crystalline LSAT, SLAO and DSO to become substrate of choice in this study along with LAO. The growth and structural analysis of Nb doped STO thin films were carried out on these substrates to understand the effect on the thermoelectric properties as a function of different substrate surface. Along with the lattice mismatch and other properties the stacking

at the interface or the self-organised growth of the Nb doped STO thin films depends mainly on the chemical termination of these substrates which could be either AO or BO₂.

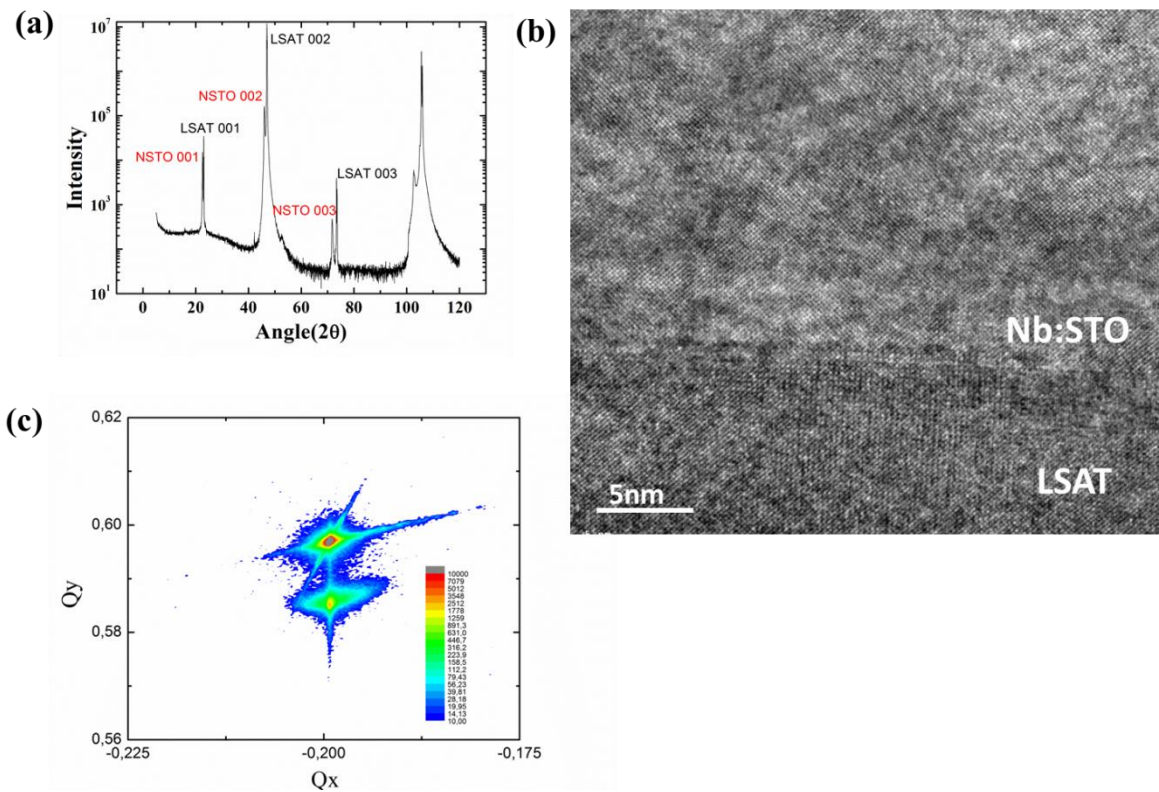


Figure 4.10 Nb:STO on LSAT. (a) XRD scans. (b) HRTEM image showing the promising crystalline quality of 2 mol% Nb-doped STO grown on LSAT. (c) Reciprocal space map of the thin film of Nb:STO on LSAT showing excellent lattice matching of the epitaxial film and the substrate.

After a detailed structural and thermoelectric study, LSAT proved to be the best substrate for the epitaxial growth of Nb-doped STO thin film. There are many reasons behind choosing LSAT, for example, it exhibit a reduced optical band gap and enhanced photocatalytic properties [158] making the surface an ideal candidate for solar photochemistry experiments.

Other heterostructures and superlattices involving STO were grown on LSAT substrates taking advantage of its cubic structure and the good lattice matching to STO (as shown in table 4.3), as also shown in the reciprocal space map in figure 4.7c). Figure 4.10 shows the structural analysis performed on the best substrate in this study, i.e., LSAT. The growth direction of the film is 001 to the LSAT substrate. The HRTEM image shown in figure 4.10b shows the excellent crystalline quality of a thin film of Nb:STO on LSAT substrate. In several of these heterostructures, a 2DEG is observed within the STO layer, although it is not

clear whether free electrons diffuse into the LSAT substrate or not. In the literature evidence is emerging on the understanding of valence and conduction band offsets at semiconductor and insulator interfaces, which is critically important to predict the behaviour of thin films in structures using Si-STO system[65, 139, 158]. LSAT films grown on STO have also yielded evidence of 2DEG formation at the interface, attributed to the polar discontinuity between the mixed polarity of LSAT and non-polar STO [159]. In their work, Huang et al. [160] postulate a mixture of localized holes and the 2DEG within the STO substrate as a result of the mixed polarity of LSAT, which is claimed to have regions of LaAlO_3 - like and $\text{Sr}_2\text{AlTaO}_6$ -like character. Clearly, much remains to be examined and generalised to make progress.

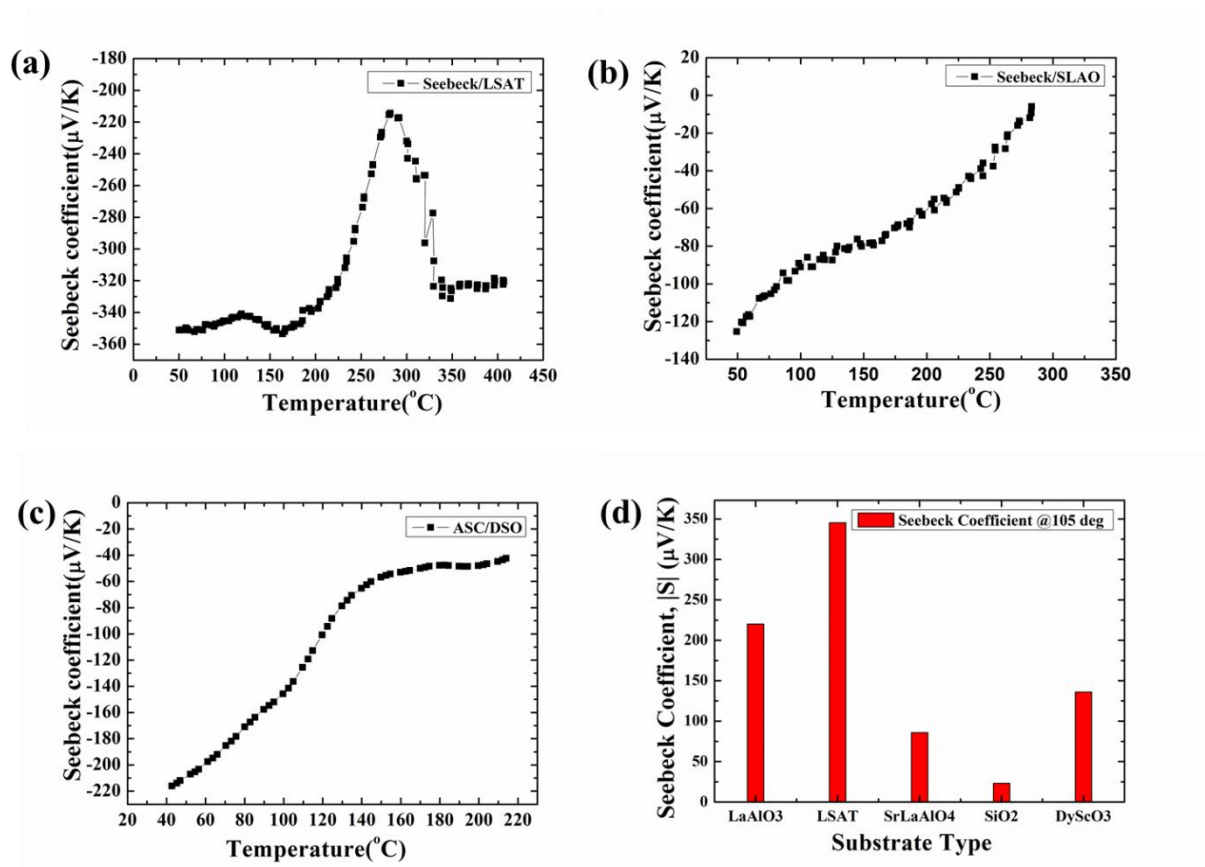


Figure 4.11 Seebeck coefficient of Nb:STO on several substrates. (a) on LSAT, (b) on SrLaAlO_4 , (c) on DyScO_3 and (d) full set of data for one thickness of Nb:STO thin film.

There are many studies reported on the reconstruction of the SrO terminated surfaces of these films on LSAT or LAO substrate [161-163]. It's very important for the surface and the interface of the film that the substrate be smooth for better mobility and electrical properties of the structure.

To the best of our knowledge this is the first time that the thermoelectric properties of samples with low doped Nb:STO thin films on LSAT substrates of excellent structural properties are reported. We measured the highest Seebeck coefficient at room temperature, namely, $-320 \mu\text{V/K}$. The mobility, charge carrier concentration and electrical conductivity were measured in the thin films on various substrates, giving a carrier concentration of the order of 10^{21} cm^{-3} . The highest conductivity was measured in the Nb:STO/LSAT combination, reaching 723 S/cm and the film exhibited a 3-fold reduction in thermal conductivity down to 2.7 W/mK (cf. the bulk value of 5.1 W/mK).

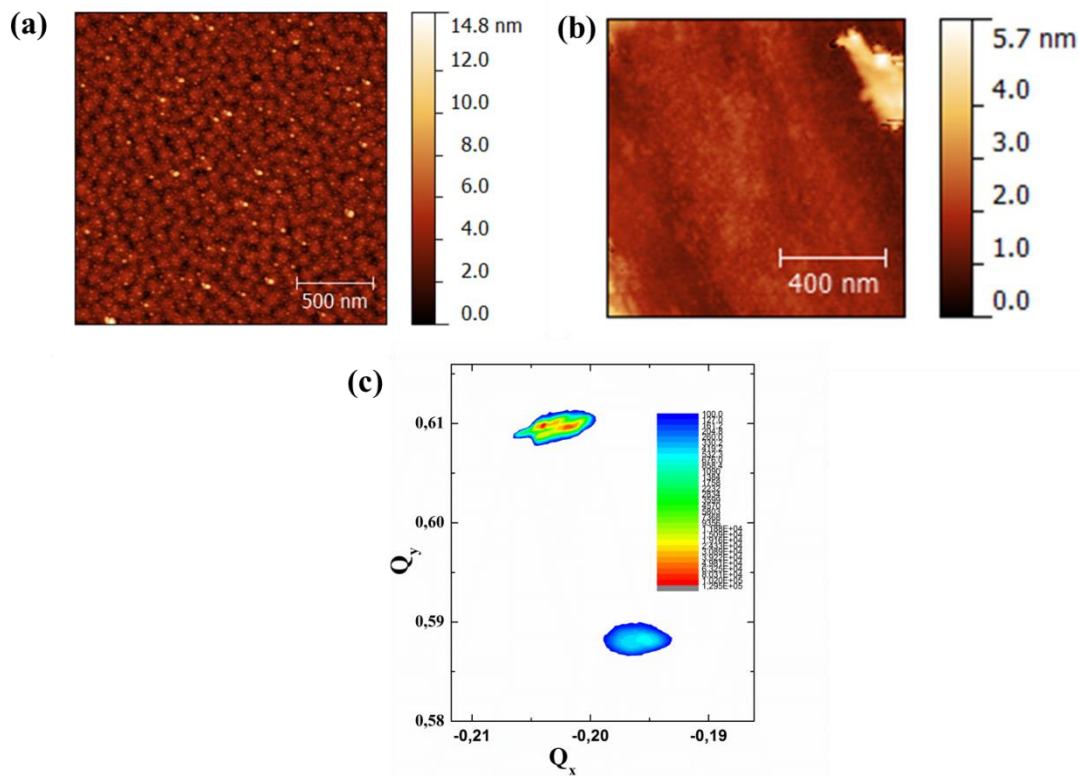


Figure 4.12 AFM images of Nb:STO on (a) a LAO substrate and (b) a LSAT substrate showing roughness $<1 \text{ nm}$ and a smooth interface (c) Reciprocal space map of the thin film of Nb:STO on LAO showing the lattice mismatch of the epitaxial film and the substrate.

Using these measured values we calculate a room temperature ZT of 0.8, the highest reported so far. The high Seebeck coefficient may be attributed to the presence of a hard-to-prove 2DEG at the interface, supported by the Seebeck coefficient dependence on temperature shown in Figure 4.11a. as shown in the table 4.2 there is not much effect that can be seen on the n_e but definitely on the mobility of the films on different substrates due to the biaxial

strain and also the degeneracy of the Ti octahedral orbitals which is modified under compressive strain[164].

Substrate	Carrier concentration (10^{20} cm^{-3})	Mobility (cm^2/Vs)	Electrical conductivity (S/cm)	Seebeck coefficient ($\mu\text{V}/\text{K}$)	Thermal conductivity (W/mK)	ZT at 300 K
LAO	-2.14	0.68	69.4	-193±19	2.4±.01	0.28±.02
LSAT	-8.37	5.40	723.5	-320±15	2.7±.01	0.8±.1
SLAO	-8.22	4.44	584.4	-125±10	-	-

Table 4.2 Transport properties of Nb doped STO films on different substrates as the main charge carriers are electrons in thin films so is the sign of the carrier concentration. The thermal conductivity measurement for the SLAO substrate is in process.

The other substrates are being used to understand the strain and its effect on the thermoelectric properties of the structures. The thermopower of samples on DyScO₃ substrate already show very promising values compared to the SLAO substrate. This may be due to the small lattice mismatch, which is compensated by tensile strain in the layer and its strain-mediated interaction with the upper face of the substrate [165, 166]. The thermal properties are still under analysis and it is expected that ZT values of the films will be reported in the future.

Considering the lattice parameter of the bulk STO as 3.905 Å and for Nb doped STO as 3.92 Å, and to understand better the strain on different substrates it is important to know the lattice mismatch with the substrates calculated as ε [$\varepsilon = (a_{\text{sub}} - a_{\text{STO}})/a_{\text{sub}}$].

Substrate	Lattice parameter, a(A ^o)	Lattice mismatch (%)
LAO	3.792	-2.98
LSAT	3.868	-0.96
SLAO	3.75	-2.70
DSO	3.944	+0.99

Table 4.3 the lattice mismatch between STO and the different substrates.

In summary, taking the measured values as $S = -320 \mu\text{V/K}$ and conductivity from hall measurement as $\sigma = 723 \text{S/cm}$ and the thermal conductivity as 2.7W/mK and putting them into the figure of merit equation as $ZT = S^2 \sigma / K$, we get the ZT as 0.8 at room temperature. With this value we arrive to our parameters required for high performance thin film of Nb:STO to be 50 nm film of 2% Nb-doped STO on LSAT substrate. As can be seen from the results obtained, Nb-doped SrTiO_3 films, synthesized by PLD, generally exhibited higher Seebeck coefficient but lower σ compared to bulk crystals[71]. This could be due to the enhanced scattering of charge carries at interfaces with decreasing thickness. However, high values of both S and σ are obtained in our films of Nb-doped SrTiO_3 on LAO and LSAT.

4.5 Nb-doped STO multilayers

The motivation for growing multilayers was to understand better the variation of electrical and thermal properties when there more than one interface in the system and hows the high Seebeck and thermal conductivity behave with the interfacial resistance and different scattering mechanisms. Considering the best two substrates identified so far, i.e., LAO and LSAT, multilayers of doped and undoped STO layers were grown by PLD at high temperature and low pressure.

Figure 4.13a shows the arrangement of the doped and undoped STO layers on the LSAT substrate. Figure 4.13b shows the XRD diffraction and the Seebeck coefficient of the $\text{TiO}_2/\text{SrTiO}_3$ interface as a function of temperature. The values of the Seebeck coefficient are unusually high with respect to those reported for superlattices of STO on LAO substrate [11], which were hard to reproduce. In this preliminary test optimized growth conditions were followed to grow superlattices of Nb-doped STO and undoped STO on LAO and on LSAT substrates.

We measured a value of S of $-350 \mu\text{V/K}$ on LAO and $-650 \mu\text{V/K}$ at around 100°C on LSAT substrate in 5-period superlattices (40 nm each) in both cases. Studies are on-going to understand the role of interfaces and to calculate the ZT value.

The presence of a 2DEG still needs to be clarified, for example, at which interface, or at all interfaces in the 5-period superlattice. The deviation from linearity in the Seebeck coefficient as a function of temperature can be described due to the change in the scattering mechanism of the free electrons as they are scattered predominantly by acoustic phonons at high temperatures[167]. In preliminary attempts, the width of the peaks measured by ARPES

rendered the data unusable which was performed for observing the formation of band near to the Fermi level if we assume there is 2DEG formation due to confinement of electrons and attribute this reasoning to the high Seebeck coefficient.

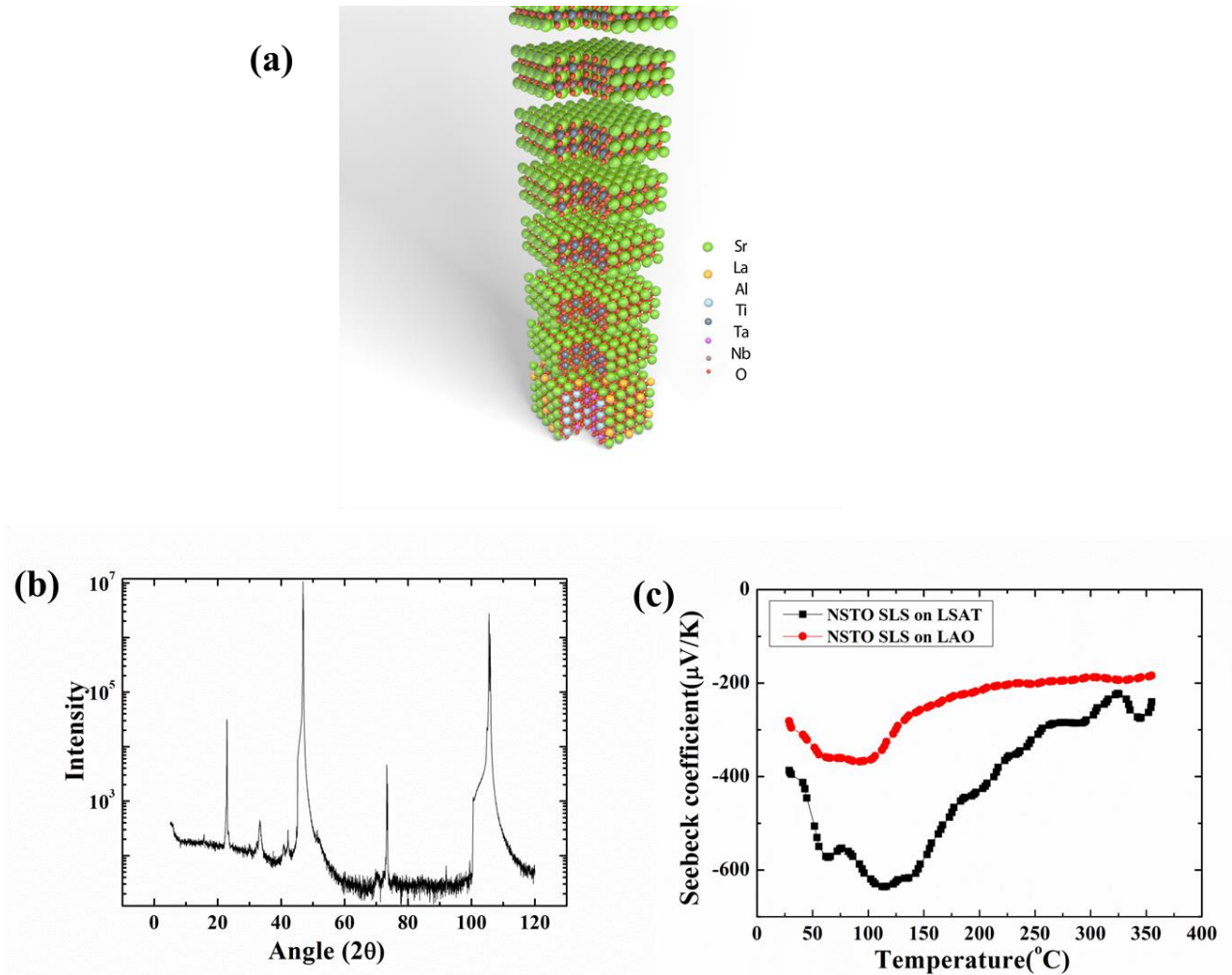


Figure 4.13 (a) 2D arrangement of atoms of the doped and undoped layers of STO on LSAT substrate (b) the XRD planes of the layers on LSAT substrate (c) the Seebeck coefficient as a function of temperature of doped and undoped STO layers on LAO and LSAT substrate.

Although these results strongly suggest that the peaks in the $|S|$ - T curves could be associated with the phonon drag effect [168] if the phonon–electron interaction were predominant at the phonon temperature T_p , the phonons would tend to push the electrons to one end of the material, giving rise to an enhancement of $|S|$. At lower temperatures, there are fewer phonons available for drag, and at higher temperatures they tend to lose momentum in phonon–phonon scattering instead of phonon–electron scattering. Thus, the phonon drag effect exhibits a maximum at T_p in the $|S|$ - T curve. This effect has been left for future work.

In summary, with further measurement of the thermal conductivity of this multilayer structure, testing for the presence of a 2DEG by synchrotron-based ARPES (Angle Resolved Photoemission Spectroscopy) and comparing to electronic energy level calculations at the interface, the STO multilayer on LSAT may prove to be a most promising n-type oxide thermoelectric material.

4.6 A novel concept: Graphene as interface dopant

As explained in chapter 3 about the growth process of the Nb doped thin film of STO on LAO and LSAT substrate with graphene as an electrical interface, we analysed the samples structurally. We also deposited superlattice structure using graphene.

Structural analysis

The PLD-grown thin films of STO on graphene/LAO and LSAT substrates were examined by x-ray diffraction (XRD). As shown in Figure 4.14, the XRD data suggest an epitaxial growth of the thin films in the 001 direction of graphene when supported on the LAO substrate. As a control, the X-ray crystallographic analysis of PLD deposited films on the transferred graphene on bare LAO substrates is also shown in Figure 4.14. The diffraction peaks corresponding to the (001) planes (c-axis preferential orientation perpendicular to the substrate surface) are typically enhanced when the substrate is heated during the PLD [78, 157, 169]. It is noteworthy that the (001) peaks increased further when the Nb-doped SrTiO₃ film was deposited onto the heated surface of the monolayer graphene (900°C), which indicate high crystalline quality.

The Raman scattering spectrum of graphene sandwiched between Nb-doped STO and LAO is shown in Figure 4.15. It exhibits the characteristic G and 2D bands with a very weak D-band merged with weak signatures of STO Raman phonons. The Raman spectrum signature of graphene indicates the CVD-graphene to be a single layer with minimal defects.

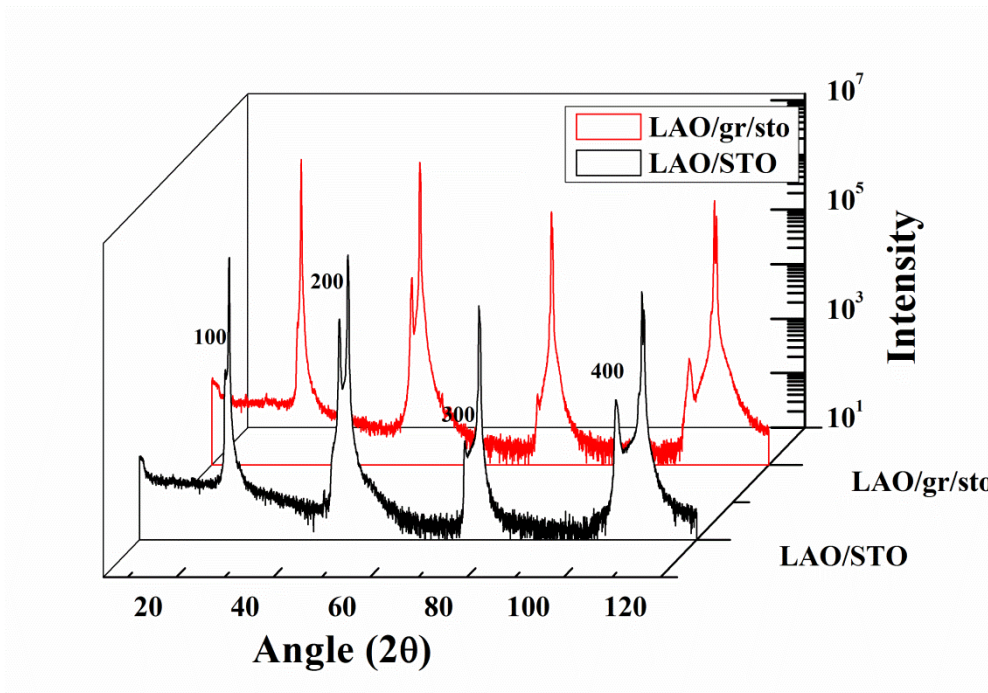


Figure 4.14 Crystal planes of Nb-doped SrTiO₃ film with and without graphene in 001 direction.

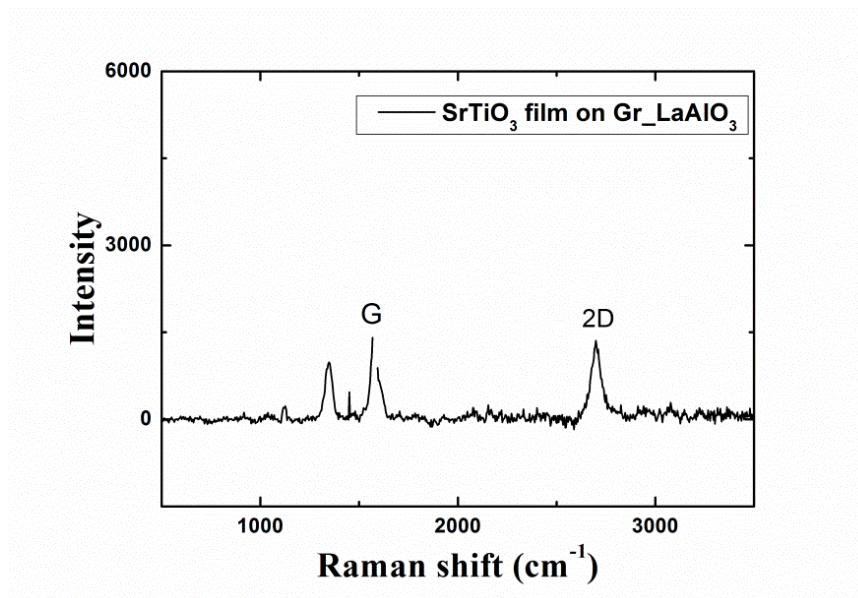


Figure 4.15 Raman spectrum of Nb:SrTiO₃/graphene showing the G and 2D peaks.

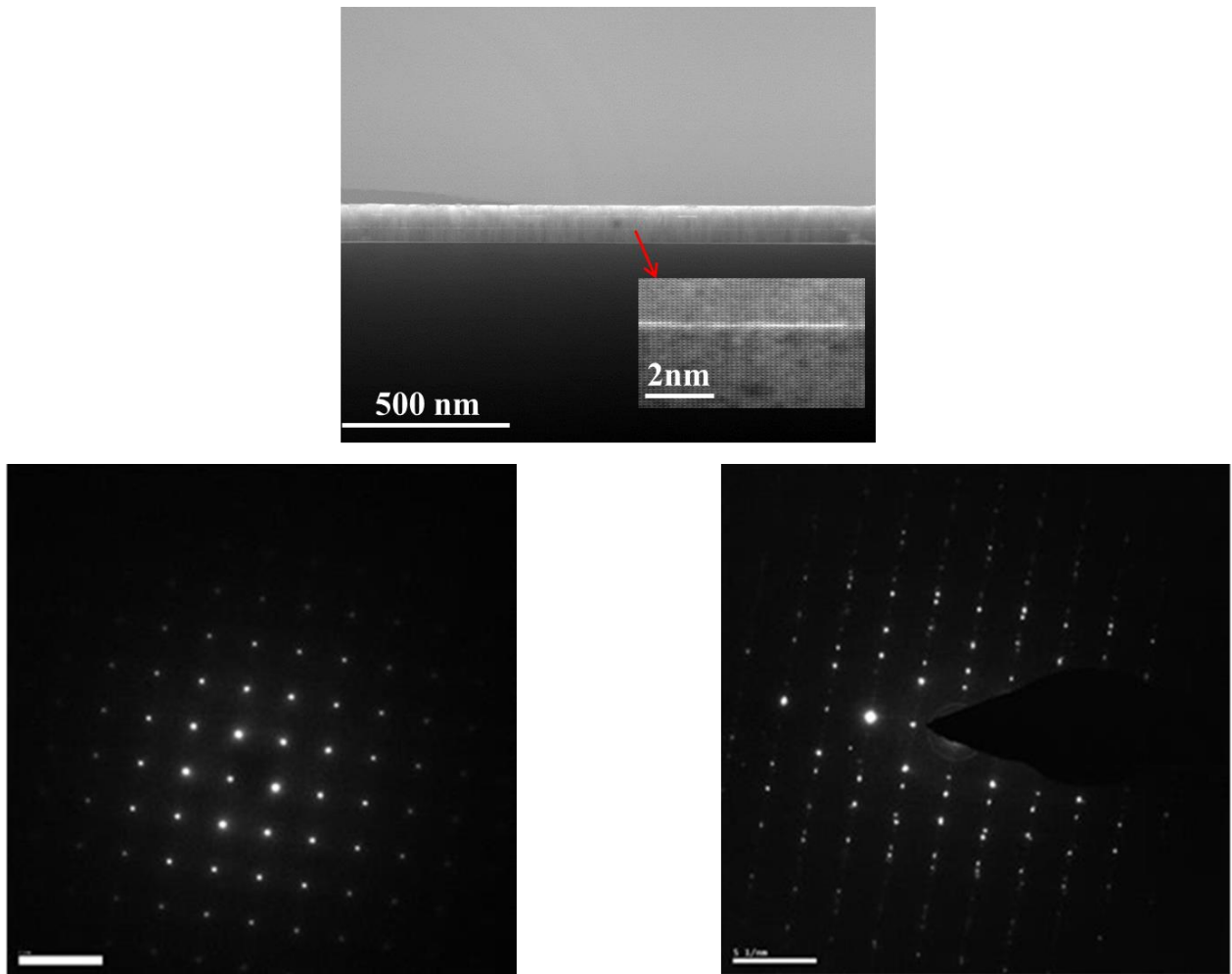


Figure 4.16 HRTEM data showing the superlattice structure of Gr/STO with the inset showing one of the interface and the diffraction pattern of Nb doped SrTiO film and graphene supported by LAO substrate.

Figure 4.16 shows the HRTEM image of superlattices of Gr-STO on LAO and inset shows one of the interface showing the graphene between the two layers of doped Nb:STO. It also shows the diffraction pattern of the LAO substrate supported by Graphene. STEM EDX data was analysed in order to determine the elemental composition and elemental distribution in the Gr-STO material system as shown in Figure 4.17.

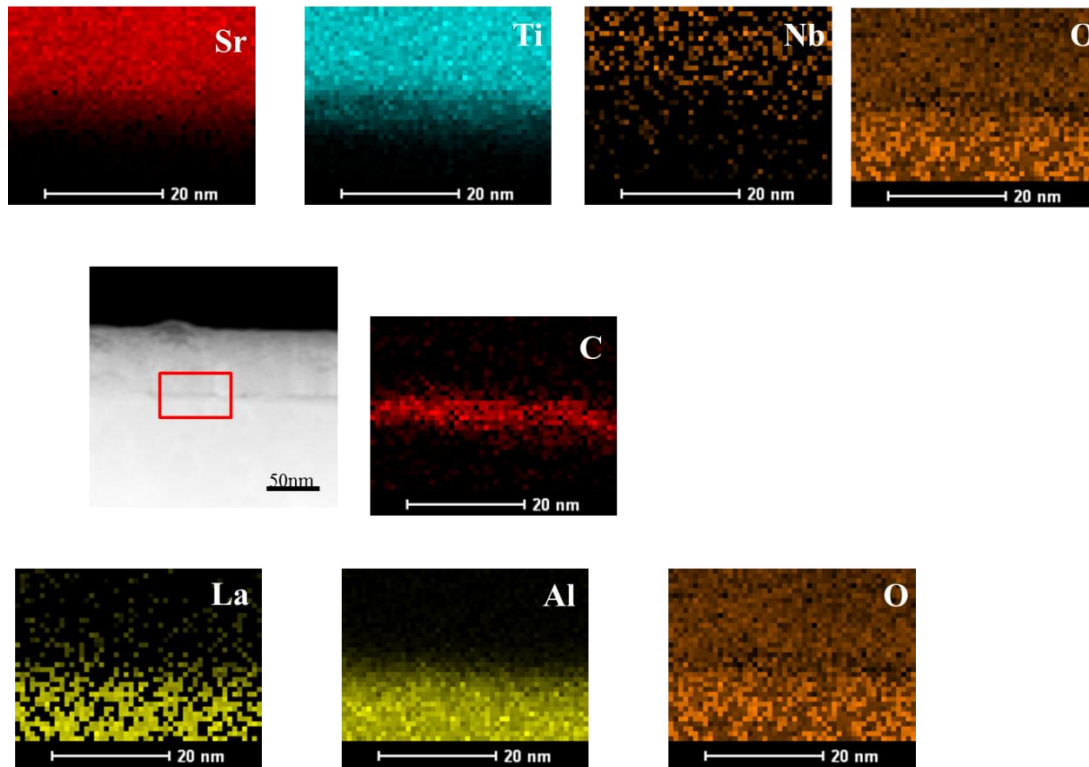


Figure 4.17 STEM-EDX mapping distribution of elements contributing to the LAO/Gr/STO thermoelectric system using HRTEM.

It was carried out in the selected area of the cross section of one of the image as shown in the figure (pointed in red square) and depending on the arrangement of the atoms we got the intensity and the STEM-EDX maps where it can be clearly seen that the O signal decreases at the interface exactly at the position where C signal is measured which indicates the presence of the C layer, compatible with the presence of monolayer graphene along with the distribution of the La, Al And O elements corresponding to the bulk LAO substrate and Sr, Ti, Nb and O elements corresponding to the Nb-doped STO thin film. These spectra are the evidence of the distribution of graphene at the interface with the growth of Nb-doped STO film on top of it. This work opens the new doors for understanding of the thin film system with graphene as an interface and how it can affect the thermal and electrical properties. The electrical and thermal properties of this system are part of the future work

Chapter 5

Conclusions and suggestions for future work

Due to the depleting reserves of the fossil fuels and accompanying detrimental effects of using them such as global warming, pollution, etc., it is high time that we focus on developing new and better technologies for sustainable energy. In this context, thermoelectricity is a fascinating physical phenomenon where temperature differences, such as in waste heat, can be directly converted to electrical energy. However, due to the low efficiency of thermoelectric conversion, its applications are limited to niche technologies such as powering satellites and car seat coolers. But after years of research on semiconductors high efficiency materials have been produced but the production cost of these materials remains prohibitively high. Current favourite materials, like Bi_2Te_3 have the disadvantage of toxicity and are scarce. Thus, our effort in this thesis was to explore key aspects thermoelectricity in complex oxides of the perovskite type as n-type thermoelectric material, since a p-type with $ZT \geq 1$ already exists, of relatively abundant and non-toxic materials.

This thesis reports the research carried out on thermoelectric properties of the oxide material, Nb:SrTiO_3 in the form of complex oxide films and superlattices. It goes from growth through structural characterisation to thermoelectric measurements. The latter constitute a crucial aspect of this research since careful measurements of the three thermoelectric quantities are required to arrive at the figure of merit ZT .

Samples were prepared with a well-defined sample preparation methodology that ensured epitaxial nature, sharp interfaces and excellent crystalline quality. These factors contributed to the quality of data obtained, which was confirmed by meticulous structural analysis.

The electrical and thermal properties were determined with commercially and home-made equipment, to ensure reliable measurements of the thin films. Measurements were cross-checked with other equipment and repeated at least two times.

A systematic method to dope SrTiO_3 thin films with Nb was developed, considering oxygen vacancies and their role in the control of carrier concentration. Carrier concentrations of the order of $10^{21}/\text{cm}^3$ were measured. The measured Seebeck coefficient was comparable and better than the highest reported one and was obtained with a 10^{th} of the doping level and in

thinner films compared to the literature. One of the most important quantities determining the transport properties of materials is the Seebeck coefficient which not only depends on carrier concentration but also on the effective mass of the charge carriers. Using niobium the effective mass could be tuned over a wide range, from 4.5 to 10 m_0 .

While the physics behind the carrier concentration level and its possible connection to charge accumulation at the interface with the substrate in the form of a two-dimensional electron gas, the presence of it could not be confirmed even though the carrier concentrations are consistent with those in the literature for such electron gas.

The first conclusion is, that a doping level of 2% suffices to optimise the Seebeck coefficient and obtain ZT at room temperature of 0.35, compared to 0.24 in the literature.

The second conclusion is related to the film thickness and the optimum value was found to be 50 nm on LSAT substrates. Since the physics of oxides interfaces is extremely complex and theoretical calculations were beyond the scope of this thesis, empirical studies were performed on a variety of well-chosen substrates.

The third conclusion relates to the choice of substrate. LSAT was found to be the most convenient substrate yielding improved ZT values of 0.8 at room temperature.

Besides the 8-fold decrease in thermal conductivity in Nb-doped thin films of STO on LAO at room temperature, which we propose is associated to the grain boundary scatterings, there was also significant increase in the power factor. This gave rise to increase in the figure of merit (ZT) at room temperature for our films compared to bulk single crystals.

The high power factor or the thermopower is most likely associated not only to the high carrier concentration but probably to the elusive 2DEG expected at the interface. Of particular importance is the extraordinary value of the Seebeck coefficient of $-640 \mu\text{V/K}$ in a superlattice of Nb:STO and undoped STO. The origin of it is still under investigation.

In this thesis, a novel idea of including graphene as a interface material between substrate and the Nb-doped STO thin film was done to enhance the overall thermoelectric properties specifically enhancing the electrical conductivity of the system and its effect on thermal properties are under investigation.

Considering all the results, it has been proved that thin film and superlattices of Nb-doped SrTiO_3 with low doping concentration is a very promising n-type oxide TE material, with

specific advantages in its growth at lower temperatures than STO with close figures of merit, ZT of 0.24 at 300K in superlattices by ohta et al.

Based on this study, there are several scientific questions which can be posed and answered with regards to complex oxide thermoelectricity in future work, such as:

1. Further exploration of the new TE system of Nb-doped SrTiO₃ with graphene by tailoring different number of single layer and its effect on overall thermoelectric properties.
2. The effect of oxide interfaces on thermal transport can be further explored by using systems with larger acoustic impedance mismatch. The most interesting question will be whether it is possible to create a large mismatch in the density of states of the phonons between two materials to reproduce the ultra-low thermal conductivity behaviour observed in disordered WSe₂ and in a crystalline superlattice.
3. The ability to consider this system for use in solar thermoelectric panels due to its ZT of 0.8 with LSAT substrate. In particular, the aspects of 2DEG formation in the presence of a specific interface configuration and lattice mismatch as well as the relation to thermal conductivity by understanding the electronic and phononic energy levels in it.
4. The tunability of thermoelectricity in titanates has been explored in terms of a different concentration of dopants, thicknesses and substrates. But the parameter window, guided by theoretical work could yield designs of thin films and superlattices for hybrid applications of this rich materials.

APPENDICES

Appendix I: Historical overview of thermoelectric parameters

1. Thermoelectric effects
 - 1.1. Seebeck coefficient

With the discovery of the Seebeck effect in 1823 due to the experiment performed with the compass needle placed between two dissimilar conductors and its deflection when one junction was heated. Seebeck erroneously concluded that the interaction was a magnetic phenomenon and related the Earth's magnetism to the temperature difference between the equator and the Poles. He investigated this phenomenon in a large number of materials, which are now called as semiconductors, and arranged them in order of the product $S\sigma$, where S is the Seebeck coefficient and σ the electrical conductivity. The Seebeck coefficient is expressed in volts per degree, or more often in microvolts per Kelvin μVK^{-1} . The Seebeck series formed in this way is very similar to the present-day thermoelectric series and, if that time Seebeck would have used the first and last members of his series in a thermocouple, he could have converted thermal energy into electricity in 1821 with an efficiency of about 3%, which compares very favourably with the most efficient steam engine of the day. The phenomenon observed by Seebeck was caused by an electric current flowing in the circuit and led to the discovery of the thermoelectric effects.

After around 12 years with the work of Peltier who observed the change in temperature at the junction between dissimilar conductors when current is passed. Although Seebeck effect was used by him but he failed to justify it and so the Peltier effect was explained by Lenz in 1838 who concluded that, heat is absorbed or generated at a junction between two conductors depending upon the direction of the flow of current, and the demonstration was done by freezing water at a bismuth-junction and melting the ice by reversing the direction of current flow.

Due to the era of other important and exciting discoveries like electromagnetism, formulation of electromagnetic laws by Faraday created the lack of interest in thermoelectrics and it took

the back seat for a period of time and it came back into limelight from 1850 with thermodynamics development and energy conversion became subject of interest.

Year **1851** came as the year of establishing the relationship between the Seebeck and Peltier coefficients experimentally and predicting the third thermoelectric effect, the Thomson effect by W. Thomson (Lord Kelvin). It states that when the current passes along a homogeneous conductor with a temperature different both heating and cooling takes place. In 1855, Rayleigh was the first who incorrectly but for the first time calculated the efficiency of thermoelectric generator by using thermoelectricity for electricity generation. But the most reliable theory came in **1909** and **1911** by Altenkirch who predicted good TE materials should have large Seebeck coefficients with low thermal conductivity (K) to retain the heat at the junction and for the thermoelectric generation and refrigeration application low electrical resistance is required to minimize Joule heating. All these properties together gave the figure-of-merit Z , where $Z = S^2\sigma/K$ and the unit of Z is $1/K$. but at a given temperature as Z may vary with T it's called a non-dimensional figure-of-merit, ZT . Even after knowing the properties required for thermoelectric applications, still researcher's attentions focused on metal and metal alloys and the important advantages of Seebeck's mineral semiconductors took a backseat.

In the late 1930s again interest developed in thermoelectricity with the development of the synthetic semiconductors having Seebeck coefficients of $100 \mu V/K$ and the fully operational generator with efficiency of 5% was constructed by Telkes in 1947. During this time there were many people who contributed to the field like Ioffe in 1949 who developed a theory of semiconductor thermoelements and Goldsmid and Douglas in 1954 stated that cooling from ordinary ambient temperatures down to below $0^\circ C$ was possible through a demonstration? But again unfortunately, the interest waivered out on thermoelectrics as the semiconductors had greater thermal to electrical conductivity ratio as compared to the metals and hence the poor electrical conductivity. The research took an amazing turn in 1950s when compound semiconductors which were used for the transistor applications gave pathway for the new materials with much improved thermoelectric properties which was demonstrated by Ioffe and his co-workers in 1956 by decreasing this ratio using alloying with an isomorphous element or compound. With this in mind discovery of semiconductors with ZT approaching 1.5 took place at RCA Laboratories in the U.S and was also being considered for the military applications.

Electrical conductivity and mobility

The electrical properties are very important in the thermoelectric phenomenon which contributes to the Seebeck as well. The momentum of a free electron is related to the wavevector by $m\mathbf{v} = \hbar\mathbf{k}$. Force of an electron with a charge $-e$ in the presence of an electric field \mathbf{E} and magnetic field \mathbf{B} is $-e[\mathbf{E} + (1/c)\mathbf{v} \times \mathbf{B}]$, with this the Newton's second law of motion becomes

$$\mathbf{F} = m \frac{d\mathbf{v}}{dt} = \hbar \frac{d\mathbf{k}}{dt} = -e \left[\mathbf{E} + \frac{1}{c} \mathbf{v} \times \mathbf{B} \right] \quad 1$$

With the constant applied electric field with the fermi sphere moves in k space at a uniform rate in the absence of collisions. We integrate (1) with $\mathbf{B} = \mathbf{0}$ to obtain

$$\mathbf{k}(t) - \mathbf{k}(0) = -e\mathbf{E}t/\hbar \quad 2$$

The sphere is displaced to a new center at a later time t when the force $\mathbf{F} = -e\mathbf{E}$ is applied at time $t = 0$ to an electron gas that at the origin of k space and fills the Fermi sphere, this displacement is given by,

$$\delta\mathbf{k} = -e\mathbf{E}t/\hbar \quad 3$$

The Fermi sphere is displaced as a whole because every electron is displaced by the same $\delta\mathbf{k}$. The displaced sphere may be maintained in an electric field in a steady state because of collisions of electrons with impurities, lattice imperfections, and phonons. If the collision time is τ , the displacement of the Fermi sphere in the steady state is given by (3) with $t = \tau$. If in a constant electric field \mathbf{E} there are n electrons of charge $q = -e$ per unit volume, the electric current density is

$$\mathbf{j} = nq\mathbf{v} = ne^2\tau\mathbf{E}/m \quad 4$$

This is **Ohm's law**.

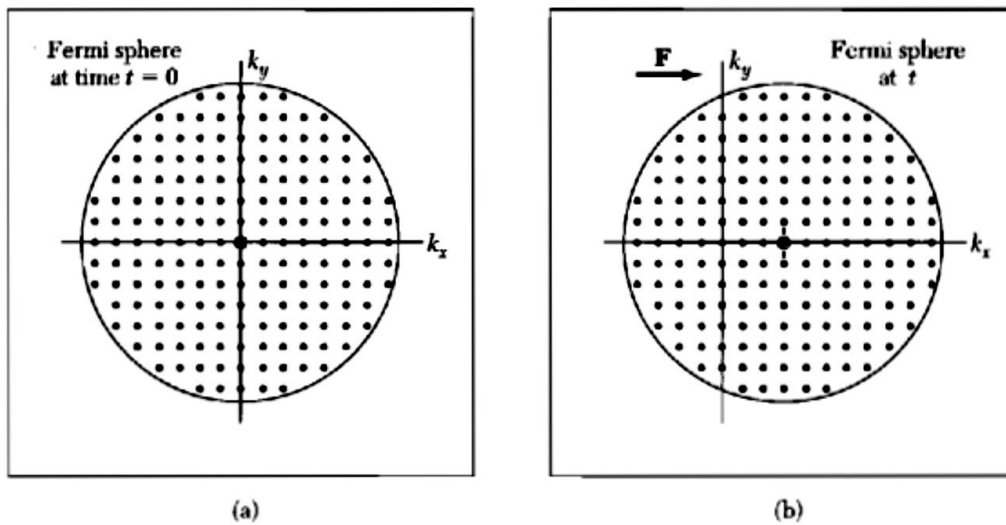


Figure 1 (a) Fermi sphere at rest i.e. $t=0$ and (b) Fermi sphere under the influence of a force, F [170].

The electrical conductivity σ is defined by $\mathbf{j} = \sigma \mathbf{E}$,

$$\sigma = \frac{ne^2\tau}{m} \quad 5$$

The electrical resistivity ρ is defined as the reciprocal of the conductivity, so that

$$\rho = \frac{m}{ne^2\tau} \quad 6$$

It is easy to understand the equation (5) for the conductivity of a Fermi gas as the charge transport is expected to be proportional to the charge density ne but as the acceleration is directly proportional to e and inversely proportional to the mass m in a given electric field so the factor e/m is introduced (5). The time τ describes the free time during which the field acts on the carrier. Closely the same result for the electrical conductivity is obtained for a classical (Maxwellian) gas of electrons, as realized at low carrier concentration in many semiconductor problems[170].

For the enhancement of the figure of merit it's very important to understand fundamentally the nature of thermoelectric coefficients. Generally, transport coefficients for materials which satisfy conventional band theory are derived using the Boltzmann transport theory. These transport coefficients are the response of a material to any applied external field such as an electric potential gradient, chemical concentration gradient or a temperature gradient. By disregarding the higher order responses, all these quantities can be derived in the linear response regime. The macroscopic relationship between current applied on the particle and the applied field is important to derive the microscopic description of the transport coefficients. Onsager reciprocal relations took into account the local equilibrium but also the generalized formalism defining the relationship between forces and flows in a thermodynamic system out of equilibrium. The Onsager's reciprocal relations are given as:

$$J = -L_{\mu\mu} \frac{\nabla\mu}{q} - L_{\mu T} \nabla T \quad 7$$

$$U = -L_{T\mu} \frac{\nabla\mu}{q} - L_{TT} \nabla T \quad 8$$

where J and U are the particle and energy currents, respectively, under the action of a chemical potential ($\nabla\mu$) and temperature (∇T) gradients. The coupling coefficients such as $L_{\mu\mu}$, $L_{\mu T}$, $L_{T\mu}$ and L_{TT} can be related to various transport coefficients. By comparing the reciprocal relations to the Boltzmann transport equation microscopic, the definition of coupling coefficients can be derived. Using the Boltzmann transport the detailed development of the transport coefficients relations and for that the basic assumptions can be found elsewhere [171-173]. Boltzmann transport formalism was primarily developed for obtaining transport coefficients for rarefied gases which follow a one particle statistical distribution. Interestingly, classical particles and wave packets too can also have the application of this equation hence it extends beyond gases. There are a few important assumptions behind the formalism. The knowledge of the statistical distribution function for the particle is essential, for example, Fermi distribution for electrons, Bose distribution for phonons etc. A generic energy distribution $f(E)$ will be taken in this discussion for the suitable distribution of any given particle. The particles will be flowing under excitation and will undergo several collisions before attaining steady state when they will be subjected to an external perturbation so that the new distribution of the particles doesn't change with time. Once steady state is achieved, the rate of change of the distribution function can be approximated as shown below:

$$\left. \frac{df(\mathbf{E})}{dT} \right|_{\text{scattering}} = \frac{-f(\mathbf{E}) - f_0(\mathbf{E})}{\tau} \quad 9$$

where τ is the relaxation time, which typically follows the Matthiessen's rule when more than one scattering mechanism is relevant. The Boltzmann transport equation is given as

$$\frac{\partial f(\vec{r}, \vec{k}, t)}{\partial t} + \vec{\partial} \vec{k} \cdot \frac{\partial f(\vec{r}, \vec{k}, t)}{\partial \vec{r}} + \frac{\partial \vec{k}}{\partial t} \cdot \frac{\partial f(\vec{r}, \vec{k}, t)}{\partial \vec{k}} = \left. \frac{\partial f(\vec{r}, \vec{k}, t)}{\partial t} \right|_{\text{scattering}} \quad 10$$

Under steady state,

$$\frac{\partial f(\vec{r}, \vec{k}, t)}{\partial t} = 0 \quad 11$$

Substituting Eq. 11 and Eq. 9 in Eq. 10,

$$\vec{\partial} \vec{k} \cdot \frac{\partial f(\vec{r}, \vec{k}, t)}{\partial \vec{r}} + \frac{\partial \vec{k}}{\partial t} \cdot \frac{\partial f(\vec{r}, \vec{k}, t)}{\partial \vec{k}} = - \frac{-f(\mathbf{E}) - f_0(\mathbf{E})}{\tau} \quad 12$$

In the limit of small applied external perturbation (linear response regime),

$$f(\vec{r}, \vec{k}) = f_0(\mathbf{E}) + f_1(\vec{r}, \vec{k}) \quad 13$$

Substituting Eq. 13 in Eq. 12 and simplifying,

$$\vec{\partial} \vec{k} \cdot \frac{\partial (f_0(\vec{r}, \vec{k}) + f_1(\vec{r}, \vec{k}))}{\partial \vec{r}} + \frac{\partial \vec{k}}{\partial t} \cdot \frac{\partial (f_0(\vec{r}, \vec{k}) + f_1(\vec{r}, \vec{k}))}{\partial \vec{k}} = - \frac{-f_1}{\tau} \quad 14$$

The gradient of the perturbation function can be neglected to simplify the expression as

$$\vec{\partial}(\vec{k}) \cdot \frac{\partial f_0(\vec{r}, \vec{k})}{\partial \vec{r}} + \frac{\partial \vec{k}}{\partial t} \cdot \frac{\partial f_0(\vec{r}, \vec{k})}{\partial \vec{k}} = - \frac{f_1}{\tau} \quad 15$$

Using,

$$\hbar\vec{k} = \vec{p} \quad 16$$

we get,

$$\vec{\vartheta}(\vec{k}) \cdot \frac{\partial f_0(\vec{r}, \vec{k})}{\partial \vec{r}} + \frac{\partial \vec{p}}{\partial t} \cdot \frac{\partial f_0(\vec{r}, \vec{k})}{\partial \vec{p}} = -\frac{f_1}{\tau} \quad 17$$

With the above equation we focused on understanding the electronic transport in the TE materials, so now with the following segment we will deal with the phonon transport related to thermoelectricity i.e. the lattice component of the thermal conductivity. For electrons under a field, we can use the following relations,

$$\dot{p} = q\vec{E} \quad 18$$

$$\frac{dE}{d\vec{p}} = \vartheta \quad 19$$

and

$$f_0(\vec{k}) = \frac{1}{\exp\left(\frac{E(\vec{k}) - \mu}{k_B T}\right) + 1} \quad 20$$

Simplifying Eq. 17,

$$\vec{\vartheta} \cdot \left[\frac{\partial f_0(\vec{r}, \vec{k})}{\partial \vec{r}} + q\vec{E} \frac{\partial f_0}{\partial E} \right] = -\frac{f_1}{\tau} \quad 21$$

To map the location of the chemical potential (μ), we use the bottom of the conduction band as the reference and we obtain,

$$\frac{\partial f_0(\vec{r}, \vec{k})}{\partial \vec{r}} = \frac{\partial f_0}{\partial E} \left(\frac{\partial \mu}{\partial \vec{r}} + \frac{E - \mu}{T} \frac{\partial T}{\partial \vec{r}} \right) \quad 22$$

Substituting Eq.22 in Eq.21 and using $\vec{E} = \frac{-\partial \phi}{\partial \vec{r}}$

$$\vec{\vartheta} \cdot \left[\frac{\partial f_0}{\partial E} \left(\frac{\partial \mu}{\partial \vec{r}} + \frac{E - \mu}{T} \frac{\partial T}{\partial \vec{r}} \right) - q \frac{\partial \phi}{\partial \vec{r}} \frac{\partial f_0}{\partial E} \right] = -\frac{f_1}{\tau} \quad 23$$

where ϕ is the electric potential of the system.

Thus,

$$f_1 = -\tau \vec{\vartheta} \cdot \left[-\frac{\partial \phi}{\partial \vec{r}} - \frac{E - \mu}{T} \frac{\partial T}{\partial \vec{r}} \right] \frac{\partial f_0}{\partial E} \quad 24$$

where $\Phi = \mu + q\phi$.

Now, the generalized electric charge current (\vec{J}) and the heat current (\vec{U}) are given as

$$\vec{J} = \int e \vec{\vartheta}(\vec{K}) f(\vec{r}, \vec{k}) d\vec{k} \quad 25$$

$$\vec{U} = \int (E(\vec{k}) - E_f) \vec{\vartheta}(\vec{K}) f(\vec{r}, \vec{k}) d\vec{k} \quad 26$$

As we have the Boltzmann transport equation defined in terms of energy, so we can simplify the current relations by converting the integrals from k-space to the energy space, as to do this it is very important to understand the concept of energy dependent density of states. For an electron in a three dimensional space, the energy-momentum relationship is given as,

$$E(\vec{k}) = \frac{\hbar^2 (k_x^2 + k_y^2 + k_z^2)}{2m}. \quad 27$$

The number of states available for the electron between E and $E + dE$ is given as $fD(E)dE$, where f is the distribution function and $D(E)$ is the density of states. $D(E)$ scales as \sqrt{E} for a 3D isotropic distribution of electrons. Recognizing the relationship between the energy space and k-space, the current equations can be simplified using Eq.24. Also for the ease of interpretation, let us assume the current flow in only one direction, say 'z' direction, resulting in the following equations.

$$J_z = \frac{2q}{m} \int_{E=0}^{\infty} \frac{\partial f_0}{\partial E} D(E) E \tau \left(\frac{d\Phi}{dz} + \frac{E - \mu}{T} \frac{dT}{dz} \right) dE \quad 28$$

$$U_z = \frac{2}{m} \int_{E=0}^{\infty} \frac{\partial f_0}{\partial E} D(E) E (E - \mu) \tau \left(\frac{d\Phi}{dz} + \frac{E - \mu}{T} \frac{dT}{dz} \right) dE + \frac{\mu J_z}{q}. \quad 29$$

Now, comparing Eq.28 and Eq.29 with Eq.7 and Eq.8, we get,

$$L_{\mu\mu} = \frac{2q^2}{3m} \int_{E=0}^{\infty} \left(-\frac{\partial f_0}{\partial E} \right) D(E) E \tau dE \quad 30$$

$$L_{\mu T} = \frac{2q}{3mT} \int_{E=0}^{\infty} \left(-\frac{\partial f_0}{\partial E} \right) D(E)E(E - \mu)\tau dE \quad 31$$

$$L_{T\mu} = \frac{2q}{3m} \int_{E=0}^{\infty} \left(-\frac{\partial f_0}{\partial E} \right) D(E)E(E - \mu)\tau dE \quad 32$$

$$L_{TT} = \frac{2}{3mT} \int_{E=0}^{\infty} \left(-\frac{\partial f_0}{\partial E} \right) D(E)E(E - \mu)^2\tau dE. \quad 33$$

Now using the coefficients of Onsager's reciprocal relations we can derive the thermoelectric parameters such as electrical conductivity (σ), thermopower (S) and electronic component of thermal conductivity (κ_e) which are given below:

$$\sigma = L_{\mu\mu} = \frac{2q^2}{3m} \int_{E=0}^{\infty} \left(-\frac{\partial f_0}{\partial E} \right) D(E)E\tau dE \quad 34$$

$$S = \frac{L_{\mu T}}{L_{\mu\mu}} = \frac{1}{qT} \frac{\int_{E=0}^{\infty} \frac{\partial f_0}{\partial E} D(E)E(E - \mu)\tau dE}{\int_{E=0}^{\infty} \frac{\partial f_0}{\partial E} D(E)E\tau dE} \quad 35$$

$$\kappa_e = \left(L_{TT} - \frac{L_{T\mu}L_{\mu T}}{L_{\mu\mu}} \right) = \frac{2}{3mT} \left(\frac{\left(\int_{E=0}^{\infty} \left(-\frac{\partial f_0}{\partial E} \right) D(E)E^2\tau dE \right)^2}{\int_{E=0}^{\infty} \left(-\frac{\partial f_0}{\partial E} \right) D(E)E\tau dE} - \int_{E=0}^{\infty} \left(-\frac{\partial f_0}{\partial E} \right) D(E)E^3\tau dE \right) \quad 36$$

we need to use the Fourier's law of heat conduction to derive the lattice component of the thermal conductivity, which can be readily obtained from a reduced form of Eq.7 and is given below:

$$U = -\kappa \nabla T \quad 37$$

For the derivation of the phonon thermal conductivity relationship, it is important to develop a microscopic understanding of phonons. A detail treatment of the understanding of the dispersion of phonons and derivation of thermal conductivity can be found elsewhere [8]. using a ball and spring model we can easily mimic the behaviour of the Phonons which are quasi-particles representing the atomic vibrations in solids and some liquids. A collection of harmonic oscillators can be used for modelling the displacement behaviour of a simple one

dimensional chain of ball and spring model by simple harmonic motion. The energy of each mode of a harmonic oscillator using the elementary quantum mechanics can be given by:

$$E_k = \left(n_k + \frac{1}{2}\right)\hbar\omega_k,$$

38

where k is the wave vector and ω is the frequency of the mode. From statistical mechanics, we know that phonons are bosons and hence follow the Bose-Einstein distribution. The average occupation number of bosons as a function of energy is given by:

$$n_0(\vec{k}) = \frac{1}{\exp\left(\frac{\hbar\omega(\vec{k})}{k_B T}\right) + 1}$$

39

Using Eq.38 and Eq.39 to solve Eq.37 and Eq.26, we obtain the phonon thermal conductivity (κ_{ph}) as,

$$\kappa_{ph} = \sum_{\text{phonon modes}} \frac{1}{3} \int (\hbar\omega)\tau(\omega)v^2(\omega)D(\omega) \langle n(\omega) \rangle d\omega$$

40

Where $\langle n(\omega) \rangle$ is the average occupation number for a given mode with frequency ω . Thus using Boltzmann transport theory, we have obtained the microscopic picture of the thermoelectric transport parameters. But it is very important to understand the limitation of these expressions due to the inherent assumptions in arriving to the final result. For example, when there are no interactions or many body effects, all these results are applicable for one particle picture.

Bibliography

1. Wang, X., Z.M. Wang, and SpringerLink (Online service), *Nanoscale thermoelectrics*, in *Lecture Notes in Nanoscale Science and Technology*,. p. 1 online resource (xi, 529 pages).
2. Cao, G., *Nanostructures & nanomaterials : synthesis, properties & applications*. 2004, London ; Hackensack, NJ: Imperial College Press. xiv, 433 p.
3. Rowe, D.M., *Thermoelectrics and its energy harvesting. Modules, systems, and applications in thermoelectrics*. 2012, CRC Press,,: Boca Raton, FL. p. 1 online resource (567 pages).
4. Dresselhaus, M.S., et al., *Low dimensional thermoelectrics*. Proceedings Ict'97 - Xvi International Conference on Thermoelectrics, 1997: p. 12-20.
5. Alam, H. and S. Ramakrishna, *A review on the enhancement of figure of merit from bulk to nano-thermoelectric materials*. *Nano Energy*, 2013. **2**(2): p. 190-212.
6. Minnich, A.J., et al., *Bulk nanostructured thermoelectric materials: current research and future prospects*. *Energy & Environmental Science*, 2009. **2**(5): p. 466-479.
7. Kanatzidis, M.G., *Nanostructured Thermoelectrics: The New Paradigm?* *Chemistry of Materials*, 2010. **22**(3): p. 648-659.
8. Sootsman, J.R., D.Y. Chung, and M.G. Kanatzidis, *New and old concepts in thermoelectric materials*. *Angew Chem Int Ed Engl*, 2009. **48**(46): p. 8616-39.
9. Rowe, D.M., *CRC handbook of thermoelectrics*. 1995, Boca Raton, FL: CRC Press. 701 p.
10. Li, J.F., et al., *High-performance nanostructured thermoelectric materials*. *Npg Asia Materials*, 2010. **2**(4): p. 152-158.
11. Ohta, H., et al., *Giant thermoelectric Seebeck coefficient of two-dimensional electron gas in SrTiO₃*. *Nature Materials*, 2007. **6**(2): p. 129-134.
12. Fukushima, K. and S. Shibagaki, *Nb doped SrTiO₃ thin films deposited by pulsed laser ablation*. *Thin Solid Films*, 1998. **315**(1-2): p. 238-243.
13. Rosi, F.D., *Thermoelectricity and Thermoelectric Power Generation*. *Solid-State Electronics*, 1968. **11**(9): p. 833-&.
14. Sales, B.C., D. Mandrus, and R.K. Williams, *Filled skutterudite antimonides: A new class of thermoelectric materials*. *Science*, 1996. **272**(5266): p. 1325-1328.
15. Nolas, G.S., D.T. Morelli, and T.M. Tritt, *Skutterudites: A phonon-glass-electron crystal approach to advanced thermoelectric energy conversion applications*. *Annual Review of Materials Science*, 1999. **29**: p. 89-116.
16. Nolas, G.S., *Semiconductor clathrates: A PGEC system with potential for thermoelectric applications*. *Thermoelectric Materials 1998 - the Next Generation Materials for Small-Scale Refrigeration and Power Generation Applications*, 1999. **545**: p. 435-442.
17. Nolas, G.S., et al., *Semiconducting Ge clathrates: Promising candidates for thermoelectric applications*. *Applied Physics Letters*, 1998. **73**(2): p. 178-180.
18. Slack, G.A., *Design concepts for improved thermoelectric materials*. *Thermoelectric Materials - New Directions and Approaches*, 1997. **478**: p. 47-54.
19. Hicks, L.D. and M.S. Dresselhaus, *Effect of Quantum-Well Structures on the Thermoelectric Figure of Merit*. *Physical Review B*, 1993. **47**(19): p. 12727-12731.
20. Hicks, L.D., T.C. Harman, and M.S. Dresselhaus, *Use of Quantum-Well Superlattices to Obtain a High Figure of Merit from Nonconventional Thermoelectric-Materials*. *Applied Physics Letters*, 1993. **63**(23): p. 3230-3232.
21. Vineis, C.J., et al., *Nanostructured Thermoelectrics: Big Efficiency Gains from Small Features*. *Advanced Materials*, 2010. **22**(36): p. 3970-3980.
22. Venkatasubramanian, R., et al., *Thin-film thermoelectric devices with high room-temperature figures of merit*. *Nature*, 2001. **413**(6856): p. 597-602.
23. Harman, T.C., et al., *Quantum dot superlattice thermoelectric materials and devices*. *Science*, 2002. **297**(5590): p. 2229-2232.

24. Hsu, K.F., et al., *Cubic AgPbmSbTe_{2+m}: Bulk thermoelectric materials with high figure of merit*. Science, 2004. **303**(5659): p. 818-821.
25. Hicks, L.D., et al., *Experimental study of the effect of quantum-well structures on the thermoelectric figure of merit*. Physical Review B, 1996. **53**(16): p. 10493-10496.
26. Boukai, A.I., et al., *Silicon nanowires as efficient thermoelectric materials*. Nature, 2008. **451**(7175): p. 168-171.
27. Hochbaum, A.I., et al., *Enhanced thermoelectric performance of rough silicon nanowires*. Nature, 2008. **451**(7175): p. 163-U5.
28. Poudel, B., et al., *High-thermoelectric performance of nanostructured bismuth antimony telluride bulk alloys*. Science, 2008. **320**(5876): p. 634-638.
29. Androulakis, J., et al., *Spinodal decomposition and nucleation and growth as a means to bulk nanostructured thermoelectrics: Enhanced performance in Pb_{1-x}Sn_xTe-PbS*. Journal of the American Chemical Society, 2007. **129**(31): p. 9780-9788.
30. Altenkirch, E., *Concerning the nutz effect on thermal columns*. Physikalische Zeitschrift, 1909. **10**: p. 560-568.
31. Altenkirch, E., *Electro-thermal generation of coldness and reversible electric heating*. Physikalische Zeitschrift, 1911. **12**: p. 920-924.
32. Goldsmid, H.J. and R.W. Douglas, *The Use of Semiconductors in Thermoelectric Refrigeration*. British Journal of Applied Physics, 1954. **5**(Nov): p. 386-390.
33. Goldsmid, H.J. and A.W. Penn, *Boundary Scattering of Phonons in Solid Solutions*. Physics Letters A, 1968. **A 27**(8): p. 523-&.
34. Rowe, D.M., V.S. Shukla, and N. Savvides, *Phonon-Scattering at Grain-Boundaries in Heavily Doped Fine-Grained Silicon-Germanium Alloys*. Nature, 1981. **290**(5809): p. 765-766.
35. Nolas, G.S., J. Poon, and M. Kanatzidis, *Recent developments in bulk thermoelectric materials*. Mrs Bulletin, 2006. **31**(3): p. 199-205.
36. Liu, W.S., et al., *Studies on the Bi₂Te₃-Bi₂Se₃-Bi₂S₃ system for mid-temperature thermoelectric energy conversion*. Energy & Environmental Science, 2013. **6**(2): p. 552-560.
37. Mehta, R.J., et al., *Seebeck Tuning in Chalcogenide Nanoplate Assemblies by Nanoscale Heterostructuring*. Acs Nano, 2010. **4**(9): p. 5055-5060.
38. Majumdar, A., *Thermoelectricity in semiconductor nanostructures*. Science, 2004. **303**(5659): p. 777-778.
39. Zhao, D.L. and G. Tan, *A review of thermoelectric cooling: Materials, modeling and applications*. Applied Thermal Engineering, 2014. **66**(1-2): p. 15-24.
40. Date, A., et al., *Progress of thermoelectric power generation systems: Prospect for small to medium scale power generation*. Renewable & Sustainable Energy Reviews, 2014. **33**: p. 371-381.
41. LeBlanc, S., et al., *Material and manufacturing cost considerations for thermoelectrics*. Renewable & Sustainable Energy Reviews, 2014. **32**: p. 313-327.
42. Yadav, G.G., et al., *Nanostructure-based thermoelectric conversion: an insight into the feasibility and sustainability for large-scale deployment*. Nanoscale, 2011. **3**(9): p. 3555-3562.
43. Toprak, M., Y. Zhang, and M. Muhammed, *Chemical alloying and characterization of nanocrystalline bismuth telluride*. Materials Letters, 2003. **57**(24-25): p. 3976-3982.
44. Martin-Gonzalez, M., O. Caballero-Calero, and P. Diaz-Chao, *Nanoengineering thermoelectrics for 21st century: Energy harvesting and other trends in the field*. Renewable & Sustainable Energy Reviews, 2013. **24**: p. 288-305.
45. Tritt, T.M., *Thermoelectric Phenomena, Materials, and Applications*. Annual Review of Materials Research, Vol 41, 2011. **41**: p. 433-448.
46. Shakouri, A., *Recent Developments in Semiconductor Thermoelectric Physics and Materials*. Annual Review of Materials Research, Vol 41, 2011. **41**: p. 399-431.
47. Snyder, G.J. and E.S. Toberer, *Complex thermoelectric materials*. Nature Materials, 2008. **7**(2): p. 105-114.

48. Weidenkaff, A., et al., *Development of thermoelectric oxides for renewable energy conversion technologies*. Renewable Energy, 2008. **33**(2): p. 342-347.
49. Tomes, P., et al., *Synthesis and Characterization of New Ceramic Thermoelectrics Implemented in a Thermoelectric Oxide Module*. Journal of Electronic Materials, 2010. **39**(9): p. 1696-1703.
50. Tomes, P., et al., *Thermoelectric oxide modules tested in a solar cavity-receiver*. Journal of Materials Research, 2011. **26**(15): p. 1975-1982.
51. Bocher, L., et al., *CaMn_{1-x}NbxO₃ (x ≤ 0.08) perovskite-type phases as promising new high-temperature n-type thermoelectric materials*. Inorganic Chemistry, 2008. **47**(18): p. 8077-8085.
52. Fujita, K., T. Mochida, and K. Nakamura, *High-temperature thermoelectric properties of NaxCoO₂-delta single crystals*. Japanese Journal of Applied Physics Part 1-Regular Papers Short Notes & Review Papers, 2001. **40**(7): p. 4644-4647.
53. Shikano, M. and R. Funahashi, *Electrical and thermal properties of single-crystalline (Ca₂CoO₃)_{0.7}CoO₂ with a Ca₃Co₄O₉ structure*. Applied Physics Letters, 2003. **82**(12): p. 1851-1853.
54. Pickett, W.E., *Electronic-Structure of the High-Temperature Oxide Superconductors*. Reviews of Modern Physics, 1989. **61**(2): p. 433-512.
55. Terasaki, I., Y. Sasago, and K. Uchinokura, *Large thermoelectric power in NaCo₂O₄ single crystals*. Physical Review B, 1997. **56**(20): p. 12685-12687.
56. Koumoto, K., I. Terasaki, and R. Funahashi, *Complex oxide materials for potential thermoelectric applications*. Mrs Bulletin, 2006. **31**(3): p. 206-210.
57. Terasaki, I., et al., *Novel thermoelectric properties of complex transition-metal oxides*. Dalton Transactions, 2010. **39**(4): p. 1005-1011.
58. Terasaki, I., *High-temperature oxide thermoelectrics*. Journal of Applied Physics, 2011. **110**(5).
59. Karvonen, L., P. Tomes, and A. Weidenkaff, *Thermoelectric performance of perovskite-type oxide materials*. Material Matters, 2011. **6**(4): p. 92.
60. Ohtaki, M., *Oxide Thermoelectric Materials for Heat-to-Electricity Direct Energy Conversion*. 2009.
61. Fritsch, V., et al., *Metal-to-insulator transition in La_{1-x}BaxTiO₃*. Physical Review B, 2001. **64**(4).
62. Lee, C.H., et al., *Effect of reduced dimensionality on the optical band gap of SrTiO₃*. Applied Physics Letters, 2013. **102**(12).
63. Xiang, W., et al., *Heteroepitaxial growth of Nb-doped SrTiO₃ films on Si substrates by pulsed laser deposition for resistance memory applications*. Applied Physics Letters, 2007. **90**(5): p. 052110.
64. Junquera, J., et al., *First-principles calculation of the band offset at BaO/BaTiO₃ and SrO/SrTiO₃ interfaces*. Physical Review B, 2003. **67**(15).
65. Peacock, P.W. and J. Robertson, *Band offsets and Schottky barrier heights of high dielectric constant oxides*. Journal of Applied Physics, 2002. **92**(8): p. 4712-4721.
66. Wunderlich, W., H. Ohta, and K. Koumoto, *Enhanced effective mass in doped SrTiO₃ and related perovskites*. Physica B-Condensed Matter, 2009. **404**(16): p. 2202-2212.
67. Salehi, H., *First Principles Studies on the Electronic Structure and Band Structure of Paraelectric SrTiO₃ by Different Approximations*. Journal of Modern Physics, 2011. **2011**.
68. Frederikse, H., W. Thurber, and W. Hosler, *Electronic transport in strontium titanate*. Physical Review, 1964. **134**(2A): p. A442.
69. Frederikse, H.P.R., W.R. Thurber, and W.R. Hosler, *Electronic Transport in Strontium Titanate*. Physical Review, 1964. **134**(2a): p. A442-+.
70. Okuda, T., et al., *Large thermoelectric response of metallic perovskites: Sr_{1-x}LaxTiO₃ (0 ≤ x ≤ 0.1)*. Physical Review B, 2001. **63**(11).

71. Ohta, S., et al., *High-temperature carrier transport and thermoelectric properties of heavily La- or Nb-doped SrTiO₃ single crystals*. Journal of Applied Physics, 2005. **97**(3).
72. Ohta, S., et al., *Large thermoelectric performance of heavily Nb-doped SrTiO₃ epitaxial film at high temperature*. Applied Physics Letters, 2005. **87**(9).
73. Geim, A.K., *Graphene: Status and Prospects*. Science, 2009. **324**(5934): p. 1530-1534.
74. Novoselov, K.S., et al., *Electric field effect in atomically thin carbon films*. Science, 2004. **306**(5696): p. 666-669.
75. Gannett, W., et al., *Boron nitride substrates for high mobility chemical vapor deposited graphene*. Applied Physics Letters, 2011. **98**(24).
76. Couto, N.J.G., B. Sacepe, and A.F. Morpurgo, *Transport through Graphene on SrTiO₃*. Physical Review Letters, 2011. **107**(22).
77. Balandin, A.A., *Thermal properties of graphene and nanostructured carbon materials*. Nature Materials, 2011. **10**(8): p. 569-581.
78. Seol, J.H., et al., *Two-Dimensional Phonon Transport in Supported Graphene*. Science, 2010. **328**(5975): p. 213-216.
79. Sevincli, H. and G. Cuniberti, *Enhanced thermoelectric figure of merit in edge-disordered zigzag graphene nanoribbons*. Physical Review B, 2010. **81**(11).
80. Hong, S., et al., *A hybridized graphene carrier highway for enhanced thermoelectric power generation*. Physical Chemistry Chemical Physics, 2012. **14**(39): p. 13527-13531.
81. Das Sarma, S. and Q.Z. Li, *Graphene on SrTiO₃*. Solid State Communications, 2012. **152**(19): p. 1795-1799.
82. Tritt, T.M., *Recent trends in thermoelectric materials research III - Semiconductors and semimetals - Preface*. Recent Trends in Thermoelectric Materials Research Iii, 2001. **71**: p. Ix-Xiv.
83. Dresselhaus, M.S., et al., *New directions for low-dimensional thermoelectric materials*. Advanced Materials, 2007. **19**(8): p. 1043-1053.
84. Ioffe, A.F., *Semiconductor thermoelements, and Thermoelectric cooling*. Rev. and supplemented for the English ed ed. 1957, London: Infosearch. 184 p.
85. Cahill, D.G., et al., *Nanoscale thermal transport. II. 2003-2012*. Applied Physics Reviews, 2014. **1**(1).
86. Klemens, P.G., *The Thermal Conductivity of Dielectric Solids at Low Temperatures (Theoretical)*. Proceedings of the Royal Society of London. Series A. Mathematical and Physical Sciences, 1951. **208**(1092): p. 108-133.
87. Callaway, J., *Model for Lattice Thermal Conductivity at Low Temperatures*. Physical Review, 1959. **113**(4): p. 1046-1051.
88. Glassbrenner, C.J. and G.A. Slack, *Thermal Conductivity of Silicon and Germanium from 3\ifmmode^\circ\else\textdegree\fi K to the Melting Point*. Physical Review, 1964. **134**(4A): p. A1058-A1069.
89. Srivastava, G.P., *The physics of phonons*. 1990, Bristol ; Philadelphia: A. Hilger. xiii, 421 p.
90. AlShaikhi, A. and G.P. Srivastava, *Theoretical investigations of phonon intrinsic mean-free path in zinc-blende and wurtzite AlN*. Physical Review B, 2007. **76**(19): p. 195205.
91. Mahan, G.D. and H.B. Lyon, *Thermoelectric Devices Using Semiconductor Quantum-Wells*. Journal of Applied Physics, 1994. **76**(3): p. 1899-1901.
92. Goyal, V., D. Teweldebrhan, and A.A. Balandin, *Mechanically-exfoliated stacks of thin films of Bi₂Te₃ topological insulators with enhanced thermoelectric performance*. Applied Physics Letters, 2010. **97**(13).
93. Ghaemi, P., R.S.K. Mong, and J.E. Moore, *In-Plane Transport and Enhanced Thermoelectric Performance in Thin Films of the Topological Insulators Bi₂Te₃ and Bi₂Se₃*. Physical Review Letters, 2010. **105**(16).
94. Davami, K., et al., *Synthesis of ZnTe nanostructures by vapor-liquid-solid technique (vol 504, pg 62, 2011)*. Chemical Physics Letters, 2011. **507**(1-3): p. 208-208.

95. Markussen, T., *Surface Disordered Ge-Si Core-Shell Nanowires as Efficient Thermoelectric Materials*. Nano Letters, 2012. **12**(9): p. 4698-4704.
96. Broido, D.A. and T.L. Reinecke, *Effect of Superlattice Structure on the Thermoelectric Figure of Merit*. Physical Review B, 1995. **51**(19): p. 13797-13800.
97. Jha, P., et al. *Giant cross-plane Seebeck effect in oxide metal semiconductor superlattices for spin-magnetic thermoelectric devices*. in *Electronic Material Conference 2013*. 2013.
98. Tang, J., et al., *Holey Silicon as an Efficient Thermoelectric Material*. Nano Letters, 2010. **10**(10): p. 4279-4283.
99. Yu, J.-K., et al., *Reduction of thermal conductivity in phononic nanomesh structures*. Nat Nano, 2010. **5**(10): p. 718-721.
100. Hopkins, P.E., et al., *Phonon considerations in the reduction of thermal conductivity in phononic crystals*. Applied Physics A, 2011. **103**(3): p. 575-579.
101. Reinke, C.M., et al., *Thermal conductivity prediction of nanoscale phononic crystal slabs using a hybrid lattice dynamics-continuum mechanics technique*. AIP Advances, 2011. **1**(4): p. 041403.
102. Dechaumphai, E. and R. Chen, *Thermal transport in phononic crystals: The role of zone folding effect*. Journal of Applied Physics, 2012. **111**(7): p. 073508.
103. Balandin, A. and K.L. Wang, *Significant decrease of the lattice thermal conductivity due to phonon confinement in a free-standing semiconductor quantum well*. Physical Review B, 1998. **58**(3): p. 1544-1549.
104. Li, D., et al., *Thermal conductivity of individual silicon nanowires*. Applied Physics Letters, 2003. **83**(14): p. 2934-2936.
105. Huang, M.J., et al., *A new lattice thermal conductivity model of a thin-film semiconductor*. International Journal of Heat and Mass Transfer, 2007. **50**(1-2): p. 67-74.
106. Asheghi, M., et al., *Phonon-boundary scattering in thin silicon layers*. Applied Physics Letters, 1997. **71**(13): p. 1798-1800.
107. Liu, W. and M. Asheghi, *Phonon-boundary scattering in ultrathin single-crystal silicon layers*. Applied Physics Letters, 2004. **84**(19): p. 3819-3821.
108. Tang, G.H., et al., *Phonon boundary scattering effect on thermal conductivity of thin films*. Journal of Applied Physics, 2011. **110**(4): p. 046102.
109. Zou, J. and A. Balandin, *Phonon heat conduction in a semiconductor nanowire*. Journal of Applied Physics, 2001. **89**(5): p. 2932-2938.
110. Walkauskas, S.G., et al., *Lattice thermal conductivity of wires*. Journal of Applied Physics, 1999. **85**(5): p. 2579-2582.
111. Krebs, H.U., et al., *Pulsed laser deposition (PLD) - A versatile thin film technique*. Advances in Solid State Physics 43, 2003. **43**: p. 505-517.
112. Smith, H.M. and A.F. Turner, *Vacuum Deposited Thin Films Using a Ruby Laser*. Applied Optics, 1965. **4**(1): p. 147-&.
113. Dijkkamp, D., et al., *Preparation of Y-Ba-Cu Oxide Superconductor Thin-Films Using Pulsed Laser Evaporation from High-Tc Bulk Material*. Applied Physics Letters, 1987. **51**(8): p. 619-621.
114. Fahler, S. and H.U. Krebs, *Calculations and experiments of material removal and kinetic energy during pulsed laser ablation of metals*. Applied Surface Science, 1996. **96-8**: p. 61-65.
115. Lunney, J.G., *Pulsed-Laser Deposition of Metal and Metal Multilayer Films*. Applied Surface Science, 1995. **86**(1-4): p. 79-85.
116. Demtrode, W. and W. Jantz, *Investigation of Laser-Produced Plasmas from Metal-Surfaces*. Plasma Physics, 1970. **12**(9): p. 691-&.
117. Goldstein, J., *Scanning electron microscopy and X-ray microanalysis*. 3rd ed ed. 2003, New York etc.: Springer. XIX, 689 p.
118. Watts, J.F. and J. Wolstenholme, *An introduction to surface analysis by XPS and AES*. 2003, Chichester: John Wiley & Sons. x, 212 p.

119. Cappella, B. and G. Dietler, *Force-distance curves by atomic force microscopy*. Surface Science Reports, 1999. **34**(1-3): p. 1-+.
120. Binnig, G., C.F. Quate, and C. Gerber, *Atomic Force Microscope*. Physical Review Letters, 1986. **56**(9): p. 930-933.
121. Corbino, O.M., *Periodic resistance changes of fine metal threads, which are brought together by alternating streams as well as deduction of their thermo characteristics at high temperatures*. Physikalische Zeitschrift, 1911. **12**: p. 292-295.
122. Birge, N.O. and S.R. Nagel, *Wide-Frequency Specific-Heat Spectrometer*. Review of Scientific Instruments, 1987. **58**(8): p. 1464-1470.
123. Cahill, D.G. and R.O. Pohl, *Thermal-Conductivity of Amorphous Solids above the Plateau*. Physical Review B, 1987. **35**(8): p. 4067-4073.
124. Cahill, D.G., *Thermal-Conductivity Measurement from 30-K to 750-K - the 3-Omega Method*. Review of Scientific Instruments, 1990. **61**(2): p. 802-808.
125. Borca-Tasciuc, T., A.R. Kumar, and G. Chen, *Data reduction in 3 omega method for thin-film thermal conductivity determination*. Review of Scientific Instruments, 2001. **72**(4): p. 2139-2147.
126. Reina, A., et al., *Large Area, Few-Layer Graphene Films on Arbitrary Substrates by Chemical Vapor Deposition*. Nano Letters, 2009. **9**(1): p. 30-35.
127. Li, X., et al., *Large-area synthesis of high-quality and uniform graphene films on copper foils*. Science, 2009. **324**(5932): p. 1312-4.
128. Zebarjadi, M., et al., *Perspectives on thermoelectrics: from fundamentals to device applications*. Energy & Environmental Science, 2012. **5**(1): p. 5147-5162.
129. Zhang, B.Y., et al., *High thermoelectric performance of Nb-doped SrTiO₃ bulk materials with different doping levels*. Journal of Materials Chemistry C, 2015. **3**(43): p. 11406-11411.
130. Kolodiazny, T. and A. Petric, *The applicability of Sr-deficient n-type SrTiO₃ for SOFC anodes*. Journal of Electroceramics, 2005. **15**(1): p. 5-11.
131. Suthirakun, S., et al., *Rational design of mixed ionic and electronic conducting perovskite oxides for solid oxide fuel cell anode materials: A case study for doped SrTiO₃*. Journal of Power Sources, 2014. **245**: p. 875-885.
132. Wang, N., et al., *Effects of YSZ Additions on Thermoelectric Properties of Nb-Doped Strontium Titanate*. Journal of Electronic Materials, 2010. **39**(9): p. 1777-1781.
133. Shang, P.P., et al., *Effect of sintering temperature on thermoelectric properties of La-doped SrTiO₃ ceramics prepared by sol-gel process and spark plasma sintering*. Solid State Sciences, 2010. **12**(8): p. 1341-1346.
134. Cutler, M. and N.F. Mott, *Observation of Anderson Localization in an Electron Gas*. Physical Review, 1969. **181**(3): p. 1336-&.
135. Aguesse, F., et al., *High-temperature conductivity evaluation of Nb doped SrTiO₃ thin films: Influence of strain and growth mechanism*. Thin Solid Films, 2013. **539**: p. 384-390.
136. Ehre, D., et al., *X-ray photoelectron spectroscopy of amorphous and quasiamorphous phases of BaTiO₃ and SrTiO₃*. Physical Review B, 2008. **77**(18).
137. Fuentes, S., et al., *Structural characterisation of slightly Fe-doped SrTiO₃ grown via a sol-gel hydrothermal synthesis*. Journal of Sol-Gel Science and Technology, 2015. **75**(3): p. 593-601.
138. Marshall, M.S.J., et al., *Atomic and electronic surface structures of dopants in oxides: STM and XPS of Nb- and La-doped SrTiO₃(001)*. Physical Review B, 2011. **83**(3).
139. Chambers, S.A., et al., *Band offset and structure of SrTiO₃/Si(001) heterojunctions*. Journal of Vacuum Science & Technology a-Vacuum Surfaces and Films, 2001. **19**(3): p. 934-939.
140. Walia, S., et al., *Transition metal oxides - Thermoelectric properties*. Progress in Materials Science, 2013. **58**(8): p. 1443-1489.
141. Park, K., et al., *Colloidal synthesis and thermoelectric properties of La-doped SrTiO₃ nanoparticles*. Journal of Materials Chemistry A, 2014. **2**(12): p. 4217-4224.

142. Ohta, S., H. Ohta, and K. Koumoto, *Grain size dependence of thermoelectric performance of Nb-doped SrTiO₃ polycrystals*. Journal of the Ceramic Society of Japan, 2006. **114**(1325): p. 102-105.
143. Wilfried Wunderlich, S.O., Hiromichi Ohta, Kunihito Koumoto, *Effective mass and thermoelectric properties of SrTiO₃-based natural superlattices* evaluated by *ab-initio* calculations. International Conference on Thermoelectrics, 2005.
144. Pichanusakorn, P. and P. Bandaru, *Nanostructured thermoelectrics*. Materials Science & Engineering R-Reports, 2010. **67**(2-4): p. 19-63.
145. Medlin, D.L. and G.J. Snyder, *Interfaces in bulk thermoelectric materials A review for Current Opinion in Colloid and Interface Science*. Current Opinion in Colloid & Interface Science, 2009. **14**(4): p. 226-235.
146. Vashaee, D. and A. Shakouri, *Improved thermoelectric power factor in metal-based superlattices*. Physical Review Letters, 2004. **92**(10).
147. Bahk, J.H., Z.X. Bian, and A. Shakouri, *Electron energy filtering by a nonplanar potential to enhance the thermoelectric power factor in bulk materials*. Physical Review B, 2013. **87**(7).
148. Davies, J.H., *The physics of low-dimensional semiconductors : an introduction*. 1st. ed ed. 1998, Cambridge: Cambridge University Press. XVII, 438 p.
149. Jalan, B. and S. Stemmer, *Large Seebeck coefficients and thermoelectric power factor of La-doped SrTiO₃ thin films*. Applied Physics Letters, 2010. **97**(4).
150. Kumar, S.R.S., A.Z. Barasheed, and H.N. Alshareef, *High Temperature Thermoelectric Properties of Strontium Titanate Thin Films with Oxygen Vacancy and Niobium Doping*. Acs Applied Materials & Interfaces, 2013. **5**(15): p. 7268-7273.
151. Dehkordi, A.M., et al., *Large Thermoelectric Power Factor in Pr-Doped SrTiO₃-delta Ceramics via Grain-Boundary-Induced Mobility Enhancement*. Chemistry of Materials, 2014. **26**(7): p. 2478-2485.
152. Ioffe, A.F., *Physics of semiconductors*. 1960, New York,: Academic Press. 436 p.
153. Kovalevsky, A.V., et al., *Effect of A-Site Cation Deficiency on the Thermoelectric Performance of Donor-Substituted Strontium Titanate*. Journal of Physical Chemistry C, 2014. **118**(9): p. 4596-4606.
154. Komar, P., et al., *Half-Heusler superlattices as model systems for nanostructured thermoelectrics*. Physica Status Solidi a-Applications and Materials Science, 2016. **213**(3): p. 732-738.
155. Prestat, E., et al., *Structure and magnetism in strained Ge_{1-x-y}Sn_xMny films grown on Ge(001) by low temperature molecular beam epitaxy*. Applied Physics Letters, 2013. **103**(1).
156. Haeni, J.H., et al., *Room-temperature ferroelectricity in strained SrTiO₃*. Nature, 2004. **430**(7001): p. 758-761.
157. Ohta, H., et al., *Critical thickness for giant thermoelectric Seebeck coefficient of 2DEG confined in SrTiO₃/SrTi_{0.8}Nb_{0.2}O₃ superlattices*. Thin Solid Films, 2008. **516**(17): p. 5916-5920.
158. Comes, R.B., et al., *Visible light carrier generation in co-doped epitaxial titanate films*. Applied Physics Letters, 2015. **106**(9).
159. Han, K., et al., *Controlling Kondo-like Scattering at the SrTiO₃-based Interfaces*. Scientific Reports, 2016. **6**.
160. Huang, Z., et al., *The Effect of Polar Fluctuation and Lattice Mismatch on Carrier Mobility at Oxide Interfaces*. Nano Letters, 2016. **16**(4): p. 2307-2313.
161. Fisher, P., et al., *Stoichiometric, nonstoichiometric, and locally nonstoichiometric SrTiO₃ films grown by molecular beam epitaxy*. Journal of Applied Physics, 2008. **103**(1).
162. Kajdos, A.P. and S. Stemmer, *Surface reconstructions in molecular beam epitaxy of SrTiO₃*. Applied Physics Letters, 2014. **105**(19).
163. Castell, M.R., *Scanning tunneling microscopy of reconstructions on the SrTiO₃(001) surface*. Surface Science, 2002. **505**(1-3): p. 1-13.

164. Huang, Z., et al., *Biaxial strain-induced transport property changes in atomically tailored SrTiO₃-based systems*. Physical Review B, 2014. **90**(12).
165. Huang, Z.F. and R.C. Desai, *Instability and decomposition on the surface of strained alloy films*. Physical Review B, 2002. **65**(19).
166. Desai, R.C., et al., *Epitaxial growth in dislocation-free strained asymmetric alloy films*. Physical Review B, 2010. **81**(23).
167. Abutaha, A.I., et al., *Enhanced Thermoelectric Figure-of-Merit in Thermally Robust, Nanostructured Super lattices Based on SrTiO₃*. Chemistry of Materials, 2015. **27**(6): p. 2165-2171.
168. Cantrell, D.G. and P.N. Butcher, *A Calculation of the Phonon-Drag Contribution to the Thermopower of Quasi-2d Electrons Coupled to 3d Phonons .1. General-Theory*. Journal of Physics C-Solid State Physics, 1987. **20**(13): p. 1985-1992.
169. Wang, J., et al., *Epitaxial BiFeO₃ multiferroic thin film heterostructures*. Science, 2003. **299**(5613): p. 1719-1722.
170. Kittel, C., *Introduction to solid state physics*. 8th ed. 2005, Hoboken, NJ: Wiley. xix, 680 p.
171. Ashcroft, N.W. and N.D. Mermin, *Solid state physics*. 1976, USA: Brooks/Cole. XXI, 826 p.
172. Ziman, J.M., *Principles of theory of solids*. 2nd ed ed. 1979, Cambridge etc.: Cambridge University Press. XIII, 435 p.
173. Ziman, J.M., *Electrons and phonons : theory of transport phenomena in solids*. 1979, Oxford: Clarendon Press. XIV, 554 p.